DYNAMICAL CASIMIR EFFECT IN A SUPERCONDUCTING CIRCUIT PERIODIC LATTICE

A Thesis

by

ANDRÉS CUÉLLAR VEGA

Submitted in Partial Fulfillment of the

Requirements for the Degree of

MASTER OF SCIENCE

Major Subject: Physics

The University of Texas Rio Grande Valley

December 2021

DYNAMICAL CASIMIR EFFECT IN A SUPERCONDUCTING CIRCUIT PERIODIC LATTICE

A Thesis
by
ANDRÉS CUÉLLAR VEGA

COMMITTEE MEMBERS

Dr. Andreas Hanke
Chair of Committee

Dr. Hamidreza Ramezani
Committee Member

Dr. Soumya D. Mohanty
Committee Member

December 2021

ABSTRACT

Cuéllar Vega, Andrés, Dynamical Casimir Effect in a Superconducting Circuit Periodic Lattice. Master of Science (MS), December, 2021, 108 pp., 31 figures, 27 references.

The dynamical Casimir effect (DCE) is the generation of real photons out of the quantum vacuum due to a rapid modulation of boundary conditions for the electromagnetic field, such as a mirror oscillating at speeds comparable to the speed of light. Previous work demonstrated experimentally that DCE radiation can be generated in electrical circuits based on superconducting microfabricated waveguides, where a rapid modulation of boundary conditions corresponding to semi-transparent mirrors is realized by tuning the applied magnetic flux through superconducting quantum-interference devices (SQUIDs) that are embedded in the waveguide circuits. We propose a novel SQUID periodic lattice architecture, in which SQUIDs embedded in a coplanar waveguide (CPW) form the sites of a one-dimensional periodic lattice, resulting in a band structure and band gaps for the DCE radiation akin to classical photonic crystals. The band structure in our "quantum photonic crystals" can be tuned by the spatial distance between SQUIDs in the lattice and their Josephson energy. Moreover, the harmonic drive of the SQUIDs generating the DCE radiation can be tuned in terms of the drive frequency, amplitude, and phase. The latter two parameters can be modulated for each SQUID in the periodic array individually, making our proposed lattice architecture quite versatile. We find a rich interplay between the band structure of the lattice, the harmonic drive of the SQUIDs, and the DCE photon-flux density, which thus allows us to control, guide, and manipulate DCE radiation. We develop a theoretical and computational model for our proposed system and calculate the DCE radiation for various experimental setups. In particular, we show that a harmonic drive that breaks the left-right symmetry results in quasi unidirectional DCE radiation. Possible applications of our results in quantum information technologies are discussed.

ACKNOWLEDGMENTS

I would like to extend my gratitude to my advisor Andreas Hanke who enthusiastically accepted me as his student. I am grateful for everything you've taught me, for the physics you introduced me to, but even more for teaching me how to be a researcher. You taught me how to engage in the work: slowly, carefully, and consistently. You taught me how to discriminate the intellectual endeavors that matter, and focus on them. For these and many more lessons, for believing in my potential even more than I did myself, and for all the time we've spent working together, I'm immensely grateful.

I would also like to thank the many mentors who profoundly influenced me, often by just being an example on how to do research, teach, and live. I would like to thank Richard Price, who early in my career infected me with his passion for physics. Matthew Benacquista, for introducing me to research for the first time. Holger Pletsch and Colin Clark for showing me what a healthy and productive work culture is. Soma Mukherjee, for always having her door and heart open for her students. Soumya Mohanty, for teaching me to work like Michelangelo, with a hammer and chisel. Mario Diaz, for going above and beyond to be a guide to his students, and for being a model for the well-rounded and compassionate academic that I aspire to be. I would particularly like to thank Joseph Romano for believing in me at a time when it was much needed. For taking my intellectual interests seriously, teaching me the "know how to solve every problem that has been solved" philosophy and for doing so much to guide me. To all these mentors, the lessons you taught me will forever be with me and I will continue to transmit them to my peers and my own students.

Thank you to my fellow graduate students who accompanied me in this journey. Thank you to Zuzanna, Wiktoria, and Kazia for being there not only as classmates, but as friends. To Richard for all of our stimulating conversations, all the coffees, for teaching me the value of discipline, and for throwing the best physics parties. To Alexandro, for inspiring me with your work ethic and always reassuring me that things would be alright. To Satzhan, for all those mornings with bicycle rides and quantum foundations discussions. To Francisco, for the unconditional support and camaraderie. To Luis, for helping create the office culture I always tried to built. To Wendy, for all those moments when we shared our struggles. Your openness to even admit them validates me and inspires me to be more open myself. To Alejandro for giving me a home and a friend when I needed them most, and for all of our travels and adventures together. May there be many more.

Thank you to all my friends who supported me along the way. I am grateful to have too many to name, but you know this is for you. Thank you for sitting next to me while I worked when I didn't have time to share otherwise. Thank for cooking, living, traveling, playing music, and laughing with me. You kept my life balanced and more importantly, full of joy.

Finally, thank you to my family. To my sister Genesis and mother Veronica for all of your love and support.

TABLE OF CONTENTS

Page

LIST OF FIGURES

Page

CHAPTER I

INTRODUCTION

1.1 Zero Point Energy and the Dynamical Casimir Effect

One of the most exciting predictions of quantum field theory is the existence of quantum vacuum fluctuations. Fluctuations in the fields permeating the vacuum have lead us to re-think the nature of "empty" space. Quantum theory predicts the existence of a vacuum state, where no particles are present, yet with a non-zero energy. The existence of this zero-point energy in the quantum electromagnetic field has observable implications in different physical phenomena. Some of phenomena in the field of quantum electrodynamics (QED) which are consequences of the zero-point energy include the Lamb shift [18], where the interaction of electrons with the underlying vacuum leads to a detectable energy difference between energy states in hydrogen atoms, as well as the (static) Casimir effect [3], where two conducting plates experience a force between them explained by the difference between the vacuum energy between the plates and on the space surrounding them.

Of particular interest to us is a phenomenon where the effects of the zero-point energy can be observed in the presence of the time-dependent modulation of a boundary. First proposed half a century ago by Moore [21], the dynamical Casimir effect (DCE) refers to the spontaneous creation of photons by the excitation of the zero-point quantum states due to a moving mirror (see Fig. 1.1). Moore showed that the effect was "immeasurably small" for non-relativistic mirror trajectories. Therefore, the detection of DCE would only be possible in scenarios with boundaries exhibiting relativistic motion.

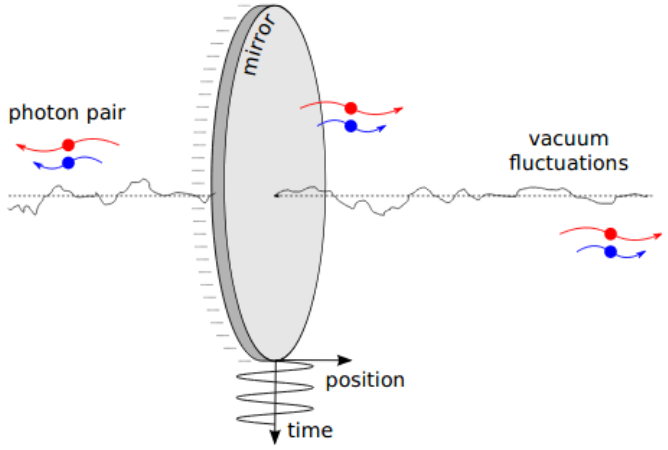

Figure 1.1: Illustration of the dynamical Casimir effect (DCE) due to an oscillating mirror. Photon pairs are created out of vacuum fluctuations by means of the non-adiabatic oscillation of a mirror. Credit: [22].

For a perfect mirror (no transmission), undergoing an oscillatory motion with frequency Ω, and oscillation amplitude a, the number of photon pairs produced per unit time is

$$\frac{N}{T} = \frac{\Omega}{3\pi}\left(\frac{v}{c}\right)^2 \tag{1.1}$$

where $v = \Omega a$ is the maximum speed of the mirror [19]. Thus, to produce a significant amount of photons requires a mirror which oscillates at speeds close to the speed of light.

Since the original proposal by Moore, the study of the DCE has evolved into a mature field with many publications analyzing theoretical implications as well as experimental realizations (see [5]). Different treatments of the DCE can be found in the literature, where states of the quantum electromagnetic field are characterized by its energy momentum tensor $T_{\alpha,\beta}(x,t)$ [8], or by means of a second-quantization expansion of the fields in the Fock state basis [6]. In this work, we employ the latter approach as it allows us to examine the field in terms of its photon statistics similar to the ones employed in [6, 19, 22].

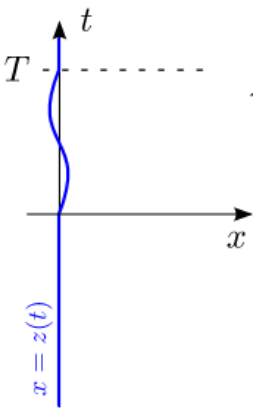

Figure 1.2: Oscillation of a mirror as a function of time. Using a Bogoliubov transformation we express the field modes at times $t > T$ as a superposition of field modes for $t < 0$. Credit: [22].

Consider a scattering-type problem of a field $\phi(x,t)$ in 1+1 dimensional space-time. The field has a boundary condition which undergoes some time-dependent change in positions between times $t = 0$ and $t = T$ (see Fig. 1.2). We can write our field as an expansion of modes at the stationary regions $t < 0$ and $t > T$ respectively:

$$\phi_{\text{in}}(x,t) = \sum_n \left[\psi_n^{(0)}(x,t)\, a_n + \text{h.c.} \right] , \tag{1.2}$$

$$\phi_{\text{out}}(x,t) = \sum_n \left[\psi_n(x,t)\, b_n + \text{h.c.} \right] . \tag{1.3}$$

Here we have assumed that the field has a discrete set of basis states. In general, the sums in Eqs. (1.2), (1.3) will be replaced by an integral over a continuous set of basis states. The modes of the field for $t > T$ are not the same as for $t < 0$, but they can be expressed as a linear superposition of these modes by means of a Bogoliubov transformation:

$$\begin{aligned} b_m &= \sum_n \left(\alpha_{nm}\, a_n + \beta_{nm}\, a_n^\dagger \right) , \\ b_m^\dagger &= \sum_k \left(\alpha_{nm}^*\, a_n^\dagger + \beta_{nm}^*\, a_n \right) , \end{aligned} \tag{1.4}$$

with the normalization $\sum_n \left(|\alpha_{nm}|^2 + |\beta_{nm}|^2 \right) = 1$ to preserve unitarity. Note that this transformation preserves the momentum of the field. If one interprets the operator b_m as annihilating a photon with

momentum k, then one can interpret the r.h.s. of the first line of Eq. (1.4) as a term that annihilates a photon with momentum k, (a_n), plus another term that creates a particle with momentum $-k$, $(a_n^\dagger)$. Thus the momentum of the field in conserved. A similar conclusion applies to the creation operator $b_m^\dagger$. Thus, photon statistics for both regions in Eqs. (1.2), (1.3) are well-defined.

We can thus find the final number of photons. For an initial field in the vacuum state ($|0\rangle$),

$$\begin{aligned} N_m^{\text{out}} &= \left\langle b_m^\dagger b_m \right\rangle_{\text{in}} \\ &= \sum_n \left\langle \left(|\alpha_{nm}|^2 a_n^\dagger a_n + |\beta_{nm}|^2 a_n a_n^\dagger \right) \right\rangle_{\text{in}} \\ &= \sum_n \left\langle \left(a_n^\dagger a_n + |\beta_{nm}|^2 \right) \right\rangle_{\text{in}} \\ &= \sum_n |\beta_{nm}|^2 \, . \end{aligned} \tag{1.5}$$

This shows a non-zero number of photons in the final state of the field, even though we started from the vacuum state, as long as there are coefficients $\beta_{nm} \neq 0$. The mixing of terms due to the scattering with a time-dependent boundary expressed through the Bogoliubov transformation in Eq. (1.4), combined with the commutation relations of the creation/annihilation operators $(a_n^\dagger, a_n)$, gives rise to the creation of DCE photons. The problem of calculating the number of DCE photons generated when there is a time-dependent modulation of the boundary condition is then equivalent to that of finding these Bogoliubov coefficients, given an initial set of basis states for the static fields.

1.2 Superconducting quantum circuits and SQUIDs

The quantum electromagnetic field is largely studied via the interactions between light and matter, by placing atoms in low loss optical cavities where they interact with a quantized electromagnetic field. This is the field of cavity QED, where experiments are done with light in the optical domain. An alternative regime is that of superconducting quantum circuits (SQC), which usually operate in the microwave regime. In this field, the role of atoms in cavity QED is taken by superconducting artificial atoms, which are quantum multi-level systems created using

Josephson junctions and superconducting circuit elements [11]. Josephson junctions are created by interrupting two superconductor segments by a insulating (non-superconducting) gap (see Fig. 1.3). The Josephson effect, which describes Cooper pairs tunneling across this insulating gap, gives SQC non-linearity without introducing dissipation. Advances in the theory and technology of superconducting circuits have developed rapidly due to their use in quantum computing and other quantum technologies [17]. Treatments for the quantum description of SQC, including the quantization method, and the input-output formalism we employ can be found in standard references for quantum network theory [26, 24].

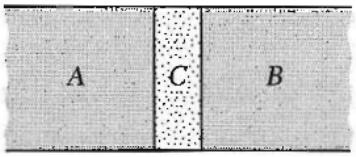

Figure 1.3: Schematic representation of a Josephson junction. Superconducting segments A and B are interrupted by a thin insulating barrier C. Credit: [16].

There are two elements of a such circuits relevant for our work. The first one is the superconducting transmission line, realized through coplanar waveguides (CPW) which consist of a central conductor surrounded by a ground plane. The second one is the superconducting quantum interference device (SQUID), which consists of a superconducting loop interrupted by two Josephson junctions. Treatments for the quantum description of SQC, including the quantization method, and the input-output formalism we employ in our quantum network theory treatment can be

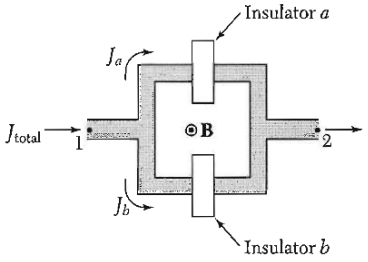

Figure 1.4: Schematic representation of a superconducting quantum interference device (SQUID). A superconducting loop is interrupted by two Josephson junctions with total current J_{total}. An external magnetic field B is applied to the loop. Credit: [16].

found in [26, 24]. The CPW can be modeled as a series of coupled inductor-capacitor (LC) circuits.

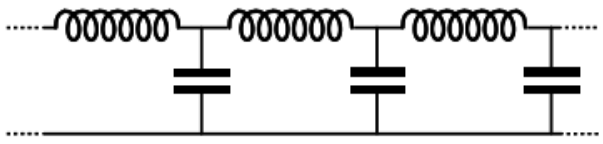

Figure 1.5: A superconducting coplanar waveguide (CPW) modeled as a series of inductors and capacitors. Credit: [24].

We describe the dynamics by introducing the magnetic flux Φ_i at site i. The Lagrangian density for the flux in the CPW is then

$$\mathscr{L} = \frac{1}{2}\sum_i \left(\Delta x C_0 \left(\dot{\Phi}_i\right)^2 - \frac{\left(\Phi_{i+1} - \Phi_i\right)^2}{\Delta x L_0} \right) \tag{1.6}$$

where Δx is the distance between nodes and C_0, L_0 are the capacitance and inductance per unit length, respectively. This Lagrangian has a similar form to the one for a mechanical oscillator. The node fluxes take the place of position coordinates, while node charges take the place of momentum. The capacitive term in the Lagrangian takes the role of kinetic energy, while the inductive term takes the role of potential energy. As for the SQUID, it also contains capacitive and inductive terms. The total inductive energy of the SQUID is

$$E_{\text{SQUID}}(t) = -E_{J_1}\cos\left(2\pi\frac{\Phi_{J_1}}{\Phi_0}\right) - E_{J_2}\cos\left(2\pi\frac{\Phi_{J_2}}{\Phi_0}\right), \tag{1.7}$$

where E_{J_α} and Φ_{J_α} are the Josephson energy and the flux through the αth Josephson junction, respectively, Φ_0 is the magnetic flux quantum, and the fluxes of Josephson junctions are related to the external flux by $\Phi_1 - \Phi_2 = \Phi_{\text{ext}}(t)$. If we consider a symmetric SQUID, such that $E_{J_1} = E_{J_2} = \varepsilon_J$ and $C_{J_1} = C_{J_2} = C_J/2$, we can write the Lagrangian density for the SQUID as

$$E_{\text{SQUID}}(t) = -2E_J\left|\cos\left(\pi\frac{\Phi_{\text{ext}}(t)}{\Phi_0}\right)\right|\cos\left(2\pi\frac{\Phi_J}{\Phi_0}\right). \tag{1.8}$$

One may think of the SQUID as a single Josephson junction with a tunable inductance which

depends on the applied magnetic flux. For a regular inductor, the energy is stored in the magnetic field passing through the coil of the inductor. For a Josephson junction, the inductance is related to the kinetic energy of Cooper pairs through the junction.

1.3 DCE in Superconducting Circuits

The superconducting microwave circuit regime has proved a promising platform to study vacuum energy amplification phenomena [22] such as the Unruh effect, parametric amplification, and an analogue Hawking radiation. More importantly for our work, this regime is where the first experimental evidence of DCE has been achieved [25].

In work by Johansson et al. [14, 15], an architecture consisting of a semi-infinite CPW terminated by a SQUID is proposed. By applying an external magnetic flux across the SQUID, the authors show that the boundary condition imposed by the SQUID mimics that of a perfectly reflecting mirror at an effective distance L^0_{eff} from the SQUID (see Fig. 1.6). This distance is given by

$$L^0_{\text{eff}} = \frac{L_J(\Phi_{\text{ext}})}{L_0}\,, \tag{1.9}$$

where $L_J(\Phi_{\text{ext}})$ is the Josephson inductance of the SQUID and L_0 is the inductance per unit length of the CPW. Applying a harmonic modulation of the external magnetic flux it is thus possible to reproduce the boundary condition of an oscillating mirror, resulting in DCE radiation. The influence of the external flux on the SQUID inductance is large enough so that a small modulation in the flux is equivalent to a significant effective amplitude of oscillation for a mirror (see Fig. 1.6). The bias lines adjacent to SQUIDs can implement frequencies of oscillation in the range of tens of GHz. The combination of "large" amplitudes and frequencies of oscillation make a SQUID a suitable candidate for detecting DCE radiation (see Section 1.1). Figure 1.7 shows results reproduced by our calculations using the analysis in [15]. The photon number density is shown as a function of frequency.

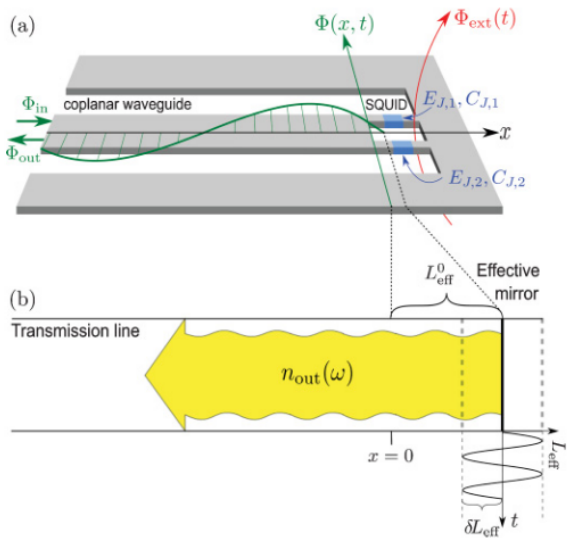

Figure 1.6: (a) Representation of a coplanar waveguide (CPW) terminated by a superconducting quantum interference device (SQUID). The external harmonic magnetic flux $\Phi_{\rm ext}(t)$ generates the boundary condition of an oscillating mirror (b) located at an effective distance $L^0_{\rm eff}$ from the SQUID at $x = 0$. The mirror oscillates with amplitude $\delta L_{\rm eff}$. The oscillation mirror produces DCE radiation. Credit: [15].

The DCE was observed experimentally in work by Wilson et. al. [25]. The radiation emitted showed two-mode squeezing, which is a signature of the pair-creation quantum process in the DCE. Shortly after, other realizations for DCE in superconducting circuits were proposed, an example being [20], where the dielectric properties of a SQUID metamaterial resonator are modulated, corresponding to a modulated cavity length and generating DCE. The entanglement nature of superconducting DCE photons has been also investigated [13], as well as its use as in quantum information and simulation. Some examples include [7, 23, 1, 27].

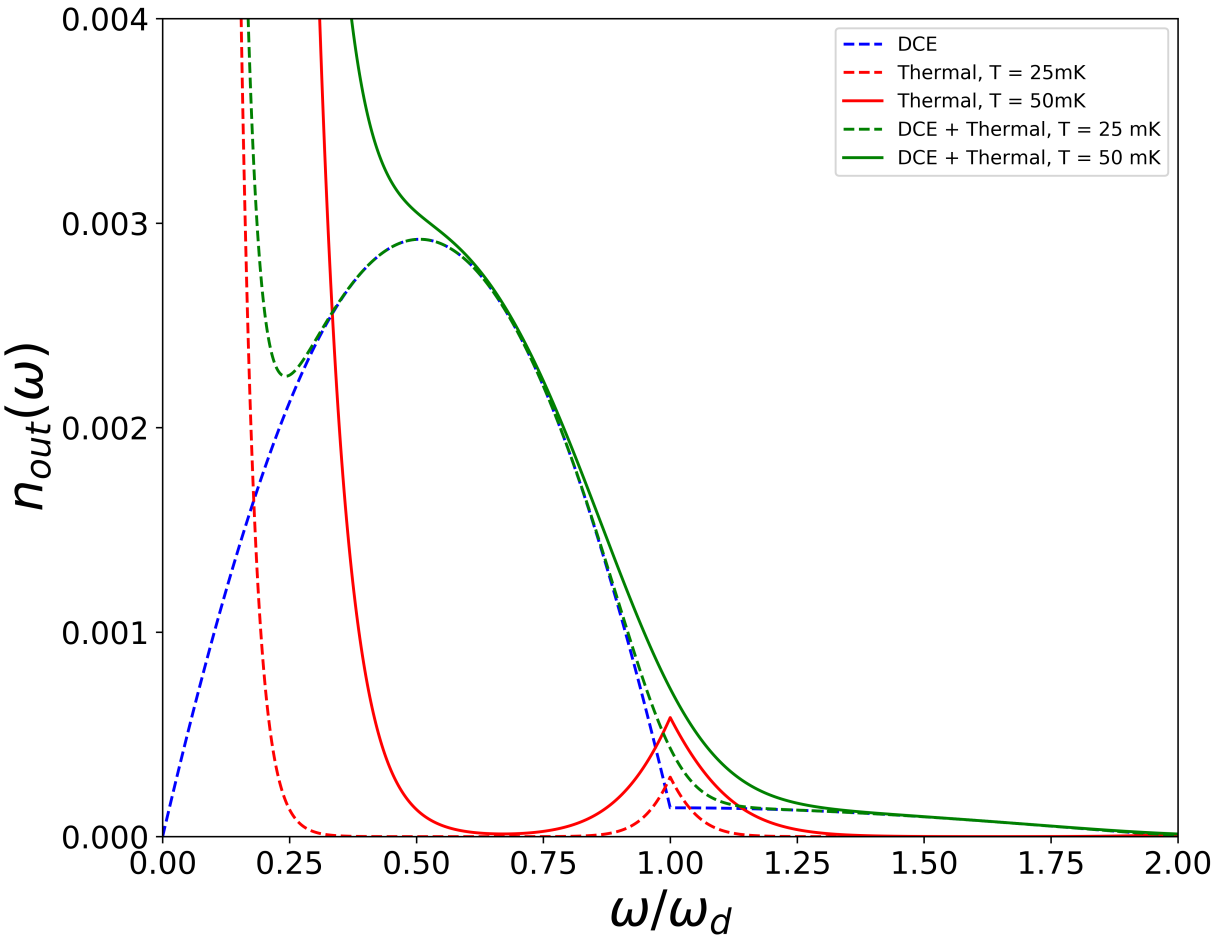

Figure 1.7: Reproduced results using the analysis from [15]. Shown is the photon number as a function of frequency in units of the SQUID driving frequency $\omega_d/2\pi$ = 18.6GHz. The output thermal radiation is shown for temperatures of 25mK and 50mK and compared with the DCE radiation emitted.

CHAPTER II

DCE IN A PERIODIC POTENTIAL

2.1 Circuit analysis for a 1D periodic potential quantum network

2.1.1 Lagrangian formulation

We now proceed to the study of the DCE in our proposed system, which consists of a periodic array of CPWs connected by SQUIDs (see Figure 2.1). To define the Lagrangian we discretize the system into segments i of length Δx with capacitance $\Delta x C_0$, inductance $\Delta x L_0$, and dynamical fluxes $\Phi_i(t)$ (see [24]). Assuming symmetric SQUIDs, the Lagrangian density for this system is

$$\begin{aligned}\mathscr{L} = &\frac{1}{2}\sum_i \left(\Delta x C_0 \left(\dot{\Phi}_i\right)^2 - \frac{\left(\Phi_{i+1} - \Phi_i\right)^2}{\Delta x L_0} \right) \\ &+ \sum_n \left[\frac{1}{2} C_{J,n} \left(\dot{\Phi}_{J,n}\right)^2 + E_{J,n}(t) \cos\left(2\pi \frac{\Phi_{J,n}}{\Phi_0}\right) \right]\end{aligned} \tag{2.1}$$

where a dot over a symbol indicates a time derivative, e.g., $\dot{\Phi}_i = \dfrac{\partial}{\partial t}\Phi_i$. The terms on the r.h.s. of the first line of Eq. (2.1) describe sections of the CPW between the SQUIDs.

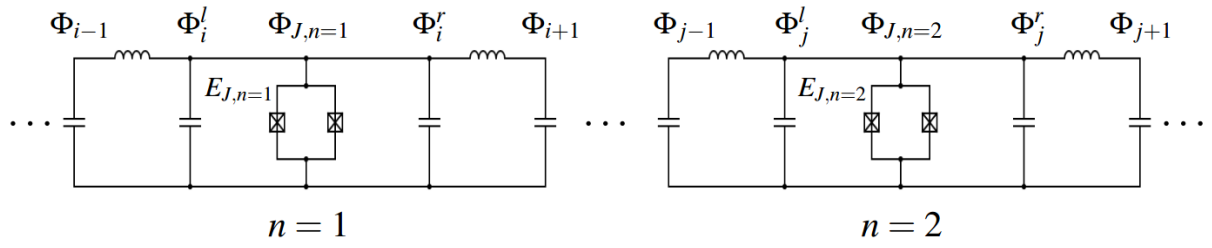

Figure 2.1: Circuit diagram for a periodic lattice consisting of CPWs connected by symmetric SQUIDs at lattice sites n. The dynamical fluxes Φ_i and $\Phi_{J,n}$ characterize the system.

The second line of Eq. (2.1) describes a periodic array of SQUIDs indexed by n with effective capacitance $C_{J,n}$ and flux $\Phi_{J,n}$ at node n, where the subscript J stands for the two Josephson junctions of a SQUID. $\Phi_0 = h/(2e)$ is the magnetic flux quantum. The SQUIDs are separated by distance ℓ corresponding to the lattice constant of the one-dimensional (1D) SQUID array. The Josephson energy $E_{J,n}(t)$ of SQUID n is tunable by the externally applied magnetic flux $\Phi_{\text{ext},n}(t)$ through the SQUID (cp. Johansson, Eq. (6)):

$$E_{J,n}(t) = 2\,\varepsilon_{J,n}\left|\cos\left(\pi\,\frac{\Phi_{\text{ext},n}(t)}{\Phi_0}\right)\right|\,, \tag{2.2}$$

where $\varepsilon_{J,n}$ is a constant energy parameter.

We now make use of considerations for the SQUID parameters similar to those found in the treatment by Johansson, et. al. [15]. We assume that the plasma frequency ω_p of the SQUIDs far exceeds other characteristic frequencies in the circuit so that oscillations in the phase across the SQUIDs have small amplitude, i.e., $\Phi_{J,n}/\Phi_0 \ll 1$, and the SQUIDs are operated in the phase regime where $E_{J,n} \gg (2e)^2/(2C_{J,n})$. Using $\Phi_{J,n}/\Phi_0 \ll 1$ one may expand the cosine in Eq. (2.1), resulting in a Lagrangian quadratic in $\Phi_{J,n}$ (dropping terms $E_{J,n}(t)$ independent of $\Phi_{J,n}$)

$$\begin{aligned}\mathscr{L} = &\frac{1}{2}\sum_i\left(\Delta x C_0\left(\dot{\Phi}_i\right)^2 - \frac{\left(\Phi_{i+1}-\Phi_i\right)^2}{\Delta x L_0}\right)\\ &+\frac{1}{2}\sum_n\left(C_{J,n}\left(\dot{\Phi}_{J,n}\right)^2 - \left(\frac{2\pi}{\Phi_0}\right)^2 E_{J,n}(t)\left(\Phi_{J,n}\right)^2\right)\,.\end{aligned} \tag{2.3}$$

Note that we make the identification $\Phi_i^l = \Phi_{J,n} = \Phi_i^r$ for the flux at SQUID n, where Φ_i^l and Φ_i^r are the fluxes at adjacent nodes to the left (l) and right (r) of node n, respectively (see Figure 2.1).

From now on, we assume that the intrinsic device parameters of all SQUIDs are equal, i.e., $C_{J,n} = C_J$, $\varepsilon_{J,n} = \varepsilon_J$ for all n in Eqs. (2.3), (2.2). Moreover, we assume that the SQUID energy $E_{J,n}(t)$ in Eq. (2.2) can be expanded in a static plus harmonic drive terms

$$E_{J,n}(t) = E_J^0 + \delta E_{J,n}\cos(\Omega t + \varphi_n) \tag{2.4}$$

where $\delta E_{J,n} < E_J^0$ and Ω is the frequency of the external drive $\Phi_{\text{ext}}(t)$ in Eq. (2.2). As indicated in Eq. (2.4), we assume that the *static* part E_J^0 of $E_{J,n}(t)$ is the same for all SQUIDs (i.e., indepedent of n). This assumption is crucial for our treatment of the *static* system (realized by a static applied magnetic flux Φ_{ext} for all SQUIDs) as a 1D periodic lattice with period ℓ. However, the time-dependent contribution in Eq. (2.4) may be modulated along the SQUID array, i.e., may differ for different SQUIDs n, in terms of amplitudes $\delta E_{J,n}$ and phases φ_n. This allows us to externally control the DCE radiation generated in the SQUID array by varying the parameters $\delta E_{J,n}$ and φ_n. However, we will assume for simplicity that the drive frequency is the same for all SQUIDs, i.e., $\Omega_n = \Omega$ for all n. That is, we consider an amplitude modulation but no frequency modulation of the time-dependent contribution in Eq. (2.4).

2.1.2 Quantization of the dynamic flux in the periodic SQUID array

To quantize the system, we first transform the Lagrangian $\mathscr{L}$ in Eq. (2.3) into a Hamiltonian $\mathscr{H}$ by a Legendre transformation. To this end, it is convenient to temporarily consider the fluxes Φ_i^l, Φ_i^r, and $\Phi_{J,n}$ at SQUIDs n as independent dynamic variables (cp. remark below Eq.(2.3)) and define

$$\mathscr{H} = \sum_i \frac{\partial \mathscr{L}}{\partial \dot{\Phi}_i} \dot{\Phi}_i + \sum_n \frac{\partial \mathscr{L}}{\partial \dot{\Phi}_{J,n}} \dot{\Phi}_{J,n} - \mathscr{L} \ , \tag{2.5}$$

resulting in

$$\begin{aligned} \mathscr{H} = & \frac{1}{2} \sum_i \left(\frac{P_i^2}{\Delta x C_0} + \frac{(\Phi_{i+1} - \Phi_i)^2}{\Delta x L_0} \right) \\ & + \frac{1}{2} \sum_n \left(\frac{(P_{J,n})^2}{C_J} + \left(\frac{2\pi}{\Phi_0} \right)^2 E_{J,n}(t) \, (\Phi_{J,n})^2 \right) \end{aligned} \tag{2.6}$$

with the canonical conjugate momenta

$$P_i = \frac{\partial \mathscr{L}}{\partial \dot{\Phi}_i} = \Delta x C_0 \dot{\Phi}_i \ , \tag{2.7a}$$

$$P_{J,n} = \frac{\partial \mathscr{L}}{\partial \dot{\Phi}_{J,n}} = C_J \dot{\Phi}_{J,n} \ . \tag{2.7b}$$

At this point, we identify again $\Phi_i^l = \Phi_{J,n} = \Phi_i^r$ and $P_i^l = P_{J,n} = P_i^r$ for the fluxes and conjugate momenta at SQUIDs n. The system is quantized by turning the fluxes $\Phi_i(t)$ and conjugate momenta $P_i(t)$ to operators $\hat{\Phi}_i(t)$, $\hat{P}_i(t)$ with equal-time commutation relations

$$\left[\hat{\Phi}_i(t), \hat{P}_j(t)\right] = i\hbar\delta_{ij} \,, \quad \left[\hat{\Phi}_i(t), \hat{\Phi}_j(t)\right] = 0 \,, \quad \left[\hat{P}_i(t), \hat{P}_j(t)\right] = 0 \,, \tag{2.8}$$

with the identifications mentioned above; for example, $\left[\hat{\Phi}_i^l, \hat{P}_{J,n}\right] = \left[\hat{\Phi}_i^r, \hat{P}_{J,n}\right] = i\hbar$ (see Figure 2.1).

2.1.3 Wave equation and boundary conditions

In the CPW between the SQUIDs, the Heisenberg equation of motion $\frac{d}{dt}\hat{P}_i = \frac{i}{\hbar}\left[\hat{\mathscr{H}}, \hat{P}_i\right]$ results in, using Eqs. (2.6) - (2.8),

$$C_0 L_0 \frac{d^2}{dt^2}\hat{\Phi}_i = \frac{1}{(\Delta x)^2}\left(\hat{\Phi}_{i+1} - 2\hat{\Phi}_i + \hat{\Phi}_{i-1}\right) \,. \tag{2.9}$$

In the continuum limit $\Delta x \to 0$ writing $\hat{\Phi}_i(t) \to \hat{\Phi}(x,t)$ with a continuous position variable x the r.h.s. of Eq. (2.9) becomes $\frac{\partial^2\hat{\Phi}(x,t)}{\partial x^2}$. We thus obtain the wave equation for the dynamic flux operator $\hat{\Phi}(x,t)$ in the CPW between the SQUIDs,

$$\frac{\partial^2\hat{\Phi}(x,t)}{\partial t^2} - v^2\frac{\partial^2\hat{\Phi}(x,t)}{\partial x^2} = 0 \,, \tag{2.10}$$

where $v = 1/\sqrt{C_0 L_0}$ is the wave propagation speed in the CPW. We note that, in the continuum limit $\Delta x \to 0$, the momentum operator conjugate to $\hat{\Phi}(x,t)$ is given by, instead of Eq. (2.7a),

$$\hat{\bar{P}}(x,t) := \frac{\hat{P}_i(t)}{\Delta x} = C_0\frac{\partial}{\partial t}\hat{\Phi}(x,t) \tag{2.11}$$

with equal-time commutation relations

$$\left[\hat{\Phi}(x,t), \hat{\bar{P}}(x',t)\right] = i\hbar\delta(x-x') \,, \quad \left[\hat{\Phi}(x,t), \hat{\Phi}(x',t)\right] = 0 \,, \quad \left[\hat{\bar{P}}(x,t), \hat{\bar{P}}(x',t)\right] = 0 \,, \tag{2.12}$$

where $\delta(x)$ is the 1D delta function (with units of $1/x$).

Similarly, at the nth SQUID site, the Heisenberg equations of motion $\frac{d}{dt}\hat{P}_{J,n} = \frac{i}{\hbar}\left[\hat{\mathscr{H}}, \hat{P}_{J,n}\right]$ results in, using Eqs. (2.6) - (2.8) with the identifications noted below Eq. (2.7b),

$$C_J \frac{d^2}{dt^2}\hat{\Phi}_{J,n} + \left(\frac{2\pi}{\Phi_0}\right)^2 E_{J,n}(t)\,\hat{\Phi}_{J,n} + \frac{1}{L_0}\left(\frac{\hat{\Phi}_{J,n} - \hat{\Phi}_{i-1}}{\Delta x} - \frac{\hat{\Phi}_{i+1} - \hat{\Phi}_{J,n}}{\Delta x}\right) = 0\,, \tag{2.13}$$

where $\hat{\Phi}_{i-1}$ and $\hat{\Phi}_{i+1}$ are adjacent nodes to the left and right of $\hat{\Phi}_i^l = \hat{\Phi}_{J,n} = \hat{\Phi}_i^r$, respectively (see Figure 2.1). In the continuum limit $\Delta x \to 0$ we obtain the boundary condition for $\hat{\Phi}(x,t)$ at the SQUID sites x_n

$$C_J \frac{\partial^2\hat{\Phi}(x_n,t)}{\partial t^2} + \left(\frac{2\pi}{\Phi_0}\right)^2 E_{J,n}(t)\,\hat{\Phi}(x_n,t) + \frac{1}{L_0}\left(\left.\frac{\partial\hat{\Phi}(x,t)}{\partial x}\right|_{x_n^-} - \left.\frac{\partial\hat{\Phi}(x,t)}{\partial x}\right|_{x_n^+}\right) = 0\,, \tag{2.14}$$

where $\left.\frac{\partial\hat{\Phi}}{\partial x}\right|_{x_n^-}$ denotes a derivative from the left $(-)$ of x_n evaluated at x_n and $\left.\frac{\partial\hat{\Phi}}{\partial x}\right|_{x_n^+}$ denotes a derivative from the right $(+)$ of x_n evaluated at x_n.

The SQUID energy $E_{J,n}(t)$ is given by Eq. (2.4). In the absence of the SQUIDs, i.e., $C_J = E_{J,n}(t) = 0$, Eq. (2.14) shows that $\partial\hat{\Phi}/\partial x$ is continuous everywhere, and the solution of the wave equation (2.10) are simple harmonic waves $\hat{\Phi}(x,t) \sim \exp[i(qx - \omega t)]$ with angular frequency ω, 1D wave vector q, and dispersion relation $\omega(q) = v|q|$ [1]. However, in the presence of the SQUIDs the boundary condition (2.14) introduces discontinuities (jumps) of $\partial\hat{\Phi}/\partial x$ at the SQUID sites $x_n = \ell n$ and $\hat{\Phi}(x,t)$ are no longer simple harmonic waves (cp. Section 2.2 below).

2.2 Static case: Relation to the Kronig-Penney model

In this section we consider the static case, in which $\delta E_{J,n} = 0$ in Eq. (2.4) and the SQUID energy $E_{J,n} = E_J^0$ is constant. In this case, the boundary condition (2.14) is given by

$$C_J \frac{\partial^2\hat{\Phi}(x_n,t)}{\partial t^2} + \left(\frac{2\pi}{\Phi_0}\right)^2 E_J^0\,\hat{\Phi}(x_n,t) + \frac{1}{L_0}\left(\left.\frac{\partial\hat{\Phi}(x,t)}{\partial x}\right|_{x_n^-} - \left.\frac{\partial\hat{\Phi}(x,t)}{\partial x}\right|_{x_n^+}\right) = 0 \tag{2.15}$$

[1] We denote the 1D wave vector for the free CPW by the symbol q to distinguish it from the wave vector k of the Bloch waves obtained for the periodic SQUID array in the static case obtained in Section 2.2.3.

2.2.1 Boundary condition in the frequency domain

We will generally work in the frequency domain instead of the time domain by expanding $\hat{\Phi}(x,t)$ in harmonic modes $\hat{\Phi}_\omega(x,t) = \hat{\varphi}(x,\omega)\exp(-i\omega t)$ of frequency ω (see Eqs. (2.51) and (2.53) below). In the frequency domain the boundary condition for the static case in Eq. (2.15) translates to a boundary condition for $\hat{\varphi}(x,\omega)$:

$$-C_J\,\omega^2\hat{\varphi}(x_n,\omega) + \left(\frac{2\pi}{\Phi_0}\right)^2 E_J^0\,\hat{\varphi}(x_n,\omega) + \frac{1}{L_0}\left(\left.\frac{\partial\hat{\varphi}(x,\omega)}{\partial x}\right|_{x_n^-} - \left.\frac{\partial\hat{\varphi}(x,\omega)}{\partial x}\right|_{x_n^+}\right) = 0 \qquad (2.16)$$

Note that Eq. (2.16) only holds in the static case because for time-dependent SQUID energy $E_{J,n}(t)$ the term $E_{J,n}(t)\,\hat{\Phi}(x_n,t)$ in Eq. (2.14) generates a coupling of modes with different frequencies ω. In large parts of this thesis we will use unitless variables by expressing lengths in units of ℓ and times in units of ℓ/v where ℓ is the distance between SQUIDs in the periodic array (see Figure 2.1) and $v = 1/\sqrt{C_0L_0}$ is the speed of light in the CPW in Eq. (2.10). The boundary condition (2.16) can be expressed in terms of unitless parameters by multiplying both sides of Eq. (2.16) by ℓL_0 resulting in [2]

$$\varepsilon(\omega)\hat{\varphi}(n,\omega) = \left.\frac{\partial\hat{\varphi}(x,\omega)}{\partial x}\right|_{n^+} - \left.\frac{\partial\hat{\varphi}(x,\omega)}{\partial x}\right|_{n^-} \qquad (2.17)$$

where n is the position of the nth SQUID in units of ℓ and

$$\varepsilon(\omega) = \ell L_0\left[-C_J\,\omega^2 + \left(\frac{2\pi}{\Phi_0}\right)^2 E_J^0\right] \qquad (2.18)$$

is a unitless parameter.

From now on we assume for simplicity that the SQUID plasma frequency ω_p is sufficiently large so that we can neglect the term $C_J\,\omega^2$ in Eq. (2.18) compared to the other term [15] (cp. text below Eq. (2.2)), i.e., we will use the ω-independent parameter

[2] We use the same symbol x for the original position variable and its unitless version (position in units of ℓ) to keep the notation simple.

$$\varepsilon = \ell \left(\frac{2\pi}{\Phi_0}\right)^2 E_J^0 L_0 \,. \tag{2.19}$$

A physical interpretation of the unitless parameter ε can be obtained by writing

$$\varepsilon = \frac{\ell}{L_{\text{eff}}^0} \text{ with } L_{\text{eff}}^0 = \left(\frac{\Phi_0}{2\pi}\right)^2 \frac{1}{E_J^0 L_0} \,. \tag{2.20}$$

For a single SQUID terminating a CPW, the parameter L_{eff}^0 can be interpreted as an effective length that gives the distance from the SQUID to a perfectly reflecting mirror [15]. Thus, ε corresponds to the ratio of the lattice constant ℓ of the SQUID array to this effective length L_{eff}^0.

2.2.2 Kronig-Penney model

The Kronig-Penney model is a simplified model for an electron in a 1D periodic potential (see [16]). Modeling the periodic potential as a Dirac comb (see Figure 2.2) with amplitude $u > 0$ and lattice constant ℓ, the time-independent Schrödinger equation reads

$$-\frac{\hbar^2}{2m}\frac{d^2}{dx^2}\psi(x) + u\,\ell \sum_n \delta(x - n\ell)\psi(x) = E\,\psi(x) \,, \tag{2.21}$$

where $\psi(x)$ is the wave function, m the mass, and E the energy of the electron. This equation can be made unitless by multiplying both sides with $\frac{2m\ell^2}{\hbar^2}$ which yields

$$-\psi''(x) + \varepsilon \sum_n \delta(x - n)\psi(x) = \mathscr{E}\psi(x) \,, \quad \text{(Kronig-Penney, unitless)} \tag{2.22}$$

where the position x is expressed in units of ℓ, the prime symbol denotes a derivative with respect to x, and

$$\varepsilon = \frac{2mu\,\ell^2}{\hbar^2} \,, \quad \mathscr{E} = \frac{2mE\ell^2}{\hbar^2} \tag{2.23}$$

are unitless (re-scaled) versions of u and E.

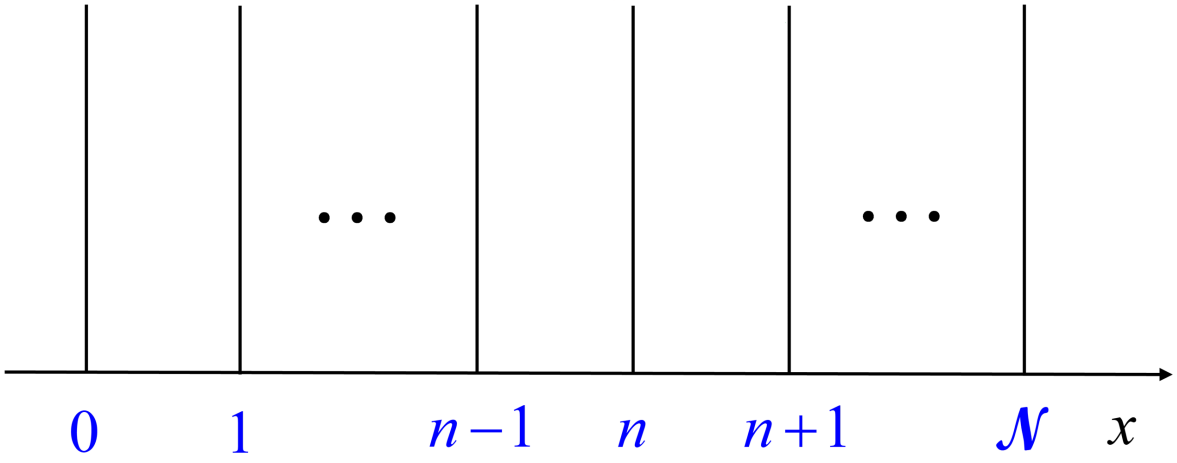

Figure 2.2: Diagrammatic representation of Dirac comb potential as an infinite series of Dirac delta distributions placed at intervals ℓ.

Integrating Eq. (2.22) over a small region about n according to $\int_{n-\delta x}^{n+\delta x} dx$ followed by the limit $\delta x \to 0$ yields a boundary condition at n in terms of a jump of the first derivative $\psi'(x)$ (see [16]).

$$\varepsilon\psi(n,\mathscr{E}) = \psi'(n,\mathscr{E})\big|_{n^+} - \psi'(n,\mathscr{E})\big|_{n^-} . \quad \text{(Kronig-Penney, unitless)} \tag{2.24}$$

Comparison with Eq. (2.17) shows that the form of the boundary conditions for the field operator $\hat{\varphi}(x,\omega)$ in the 1D periodic SQUID array (static case) and the electron wave function $\psi(x,\mathscr{E})$ in the Kronig-Penney model are identical. However, in the absence of the periodic potential in the Kronig-Penney model, i.e., $u = \varepsilon = 0$, the solution of Eq. (2.22) are harmonic waves $\psi(x,\mathscr{E}) \sim \exp(iqx)$ with 1D wave vector q and dispersion relation $\mathscr{E}(q) = q^2$ (corresponding to $E(q) = \hbar^2 q^2/(2m)$ in original variables). In contrast, for the free CPW we found the dispersion relation $\omega(q) = |q|$ in unitless variables (corresponding to $\omega(q) = v|q|$ in original variables, see text below Eq. (2.14) and footnote 1 on page 14). That is, $\omega(q)$ in the free CPW is a linear function of q instead of quadratic, which is a consequence of the fact that the particles in the CPW are massless photons whereas the electrons in the Schrödinger equation (2.21) have a finite mass m. However, except

for this difference of the dispersion relation, the solution for the field operator $\hat{\varphi}(x,\omega)$ in the 1D periodic SQUID array with boundary condition (2.17) at the SQUID sites n for the static case is analogous to that of the Kronig-Penney model.

2.2.3 Solution of the Kronig-Penney-type model for the 1D SQUID array

This subsection uses unitless variables by expressing lengths in units of ℓ and times in units of ℓ/v as discussed above [3]. In the frequency domain, the wave equation for the CPW between the SQUIDs is given by Eq. (2.10) with $\Phi_\omega(x,t) = \varphi(x,\omega)\exp(-i\omega t)$ (see Section 2.2.1), which results in [4]

$$\varphi''(x,\omega) + \omega^2\varphi(x,\omega) = 0\,. \tag{2.25}$$

The boundary conditions at the SQUID sites n, in the static case, are given by Eq. (2.17):

$$\varepsilon\varphi(n,\omega) = \left.\frac{\partial\varphi(x,\omega)}{\partial x}\right|_{n^+} - \left.\frac{\partial\varphi(x,\omega)}{\partial x}\right|_{n^-} \quad \text{for all integer } n\ . \tag{2.26}$$

Note that, by using unitless variables, the only system-specific parameter in Eqs. (2.25), (2.26) is the unitless energy parameter ε in Eq. (2.19).

The strategy for solving Eqs. (2.25) and (2.26) is to use an ansatz for $\varphi_n(x)$ for each section n of the CPW between SQUIDs as a linear combination of right-moving and left-moving plane waves with 1D wave vector $q > 0$ as in a free CPW:

$$\varphi_n(x) = A_n \exp\left[iq(x-n)\right] + B_n \exp\left[-iq(x-n)\right]\ , \quad n-1 < x < n\ , \tag{2.27}$$

and to determine the n-dependent coefficients A_n, B_n by the boundary conditions (2.26) using a transfer matrix approach. The extra terms $\exp(-iqn)$, $\exp(iqn)$ in Eq. (2.27) were introduced for computational convenience (see Mathematica notebook in the Appendix). We find solutions for the

[3] We use the same symbols x, q, k, ω, etc. for the original variables and their unitless versions to keep the notation simple. It will be clear from the context and/or by explicit marking which version of variables are used.

[4] In this subsection we skip the hat symbol for operators since the operator property of $\varphi(x,\omega)$ is not used.

Kronig-Penney-type model defined by Eqs. (2.25), (2.26) in terms of Bloch functions

$$\psi_{\nu,k}(x) = e^{ikx} u_{\nu,k}(x) \,, \tag{2.28}$$

where k is a 1D Bloch wave vector, which depends in a nontrivial way on the wave vector q used in the ansatz (2.27), and ν is the band index [2]. Since $\omega = q$ in unitless variables (corresponding to $\omega(q) = vq$ in original variables, and using $q > 0$ in Eq. (2.27)), the dependence $k(q)$ directly translates to a dependence $k(\omega)$, corresponding to the inverse of the dispersion relation $\omega_\nu(k)$ in frequency band ν for the Kronig-Penney-type model (see Figure 2.6).

The function $u_{\nu,k}(x)$ in Eq. (2.28) has period ℓ, i.e., period 1 in unitless variables, which means that $u_{\nu,k}(x+n) = u_{\nu,k}(x)$ for all integers n. Thus, $u_{\nu,k}(x)$ is completely specified by the domain $x \in [0,1]$ and periodic extension beyond this domain. The Bloch functions $\psi_{\nu,k}(x)$ in Eq. (2.28) are unitless, orthogonal with respect to the 1D wave vector k, and normalized such that

$$\int_{-\infty}^{\infty} dx\, \psi^*_{\nu,k}(x)\, \psi_{\nu',k'}(x) = 2\pi\, \delta_{\nu\nu'}\, \delta(k-k') \,. \tag{2.29}$$

Examples of the functions $u_{\nu,k}(x)$ and $\psi_{\nu,k}(x)$ are shown in Figs. 2.3 and 2.4, respectively.

The introduction of a periodic potential leads to a Bloch band structure with frequency bands ν similar to electrons in crystals [2] or photons in photonic crystals [12]. The frequency bands are determined by the relation

$$\cos k = \cos\omega + \frac{\varepsilon}{2\omega} \sin\omega \tag{2.30}$$

with ε defined in Eq. (2.19) and included in the boundary condition (2.26). Since the left-hand side of Eq. (2.30) has range $[-1,1]$ allowed frequencies ω are determined by the condition (see Figure 2.5)

$$\left| \cos\omega + \frac{\varepsilon}{2\omega} \sin\omega \right| \leq 1 \,. \tag{2.31}$$

For allowed frequencies ω, the function $k(\omega)$ is given by (using the principal value range of the

arccos function) (see Figure 2.6)

$$k(\omega) = \arccos\left[\cos\omega + \frac{\varepsilon}{2\omega}\sin\omega\right] \in [0,\pi]\,. \tag{2.32}$$

Conversely, the dispersion relation of the Kronig-Penney-type model is given by solutions $\omega_\nu(k)$ of Eq. (2.32), where the band index ν labels different solutions ω_ν for given $k \in [-\pi,\pi]$ in the first Brillouin zone of the reciprocal lattice (in unitless variables where the lattice constant is 1). Since $\omega_\nu(k) = \omega_\nu(-k)$ by symmetry of the lattice, it is sufficient to consider positive wave vectors $k > 0$. A solution of Eq. (2.32) for $\omega_\nu(k)$ obtained by graphically inverting the function $k(\omega)$ using the Mathematica function ParametricPlot (see Appendix) is shown in Figure 2.7 [5].

2.3 Harmonic drive

The goal of this section is to find solutions for the dynamic flux field $\hat{\Phi}(x,t)$ introduced in Section 2.1.3 in the presence of a time-dependent, harmonic applied magnetic flux with frequency Ω resulting in the time-dependent SQUID energy $E_{J,n}(t)$ in Eq. (2.4). In terms of unitless variables, $E_{J,n}(t)$ is given by

$$\begin{aligned} \varepsilon_n(t) &= \varepsilon + \delta\varepsilon_n^0\cos(\Omega t + \varphi_n) \\ &=: \varepsilon + \delta\varepsilon_n(t) \end{aligned} \tag{2.33}$$

with $\varepsilon = \ell\left(\frac{2\pi}{\Phi_0}\right)^2 E_J^0 L_0$ from Eq. (2.19) and the unitless amplitude

$$\delta\varepsilon_n^0 := \ell\left(\frac{2\pi}{\Phi_0}\right)^2 \delta E_{J,n} L_0\,. \tag{2.34}$$

To proceed, it will be convenient to represent the flux field $\hat{\Phi}(x,t)$ in second-quantized form.

[5] The dispersion relation $\omega_\nu(k)$ resulting from Eq. (2.32) cannot be calculated in closed form. Our calculations will therefore use the inverse function $k(\omega)$, which is directly given in analytical form by Eq. (2.32). See Section 2.3.1.

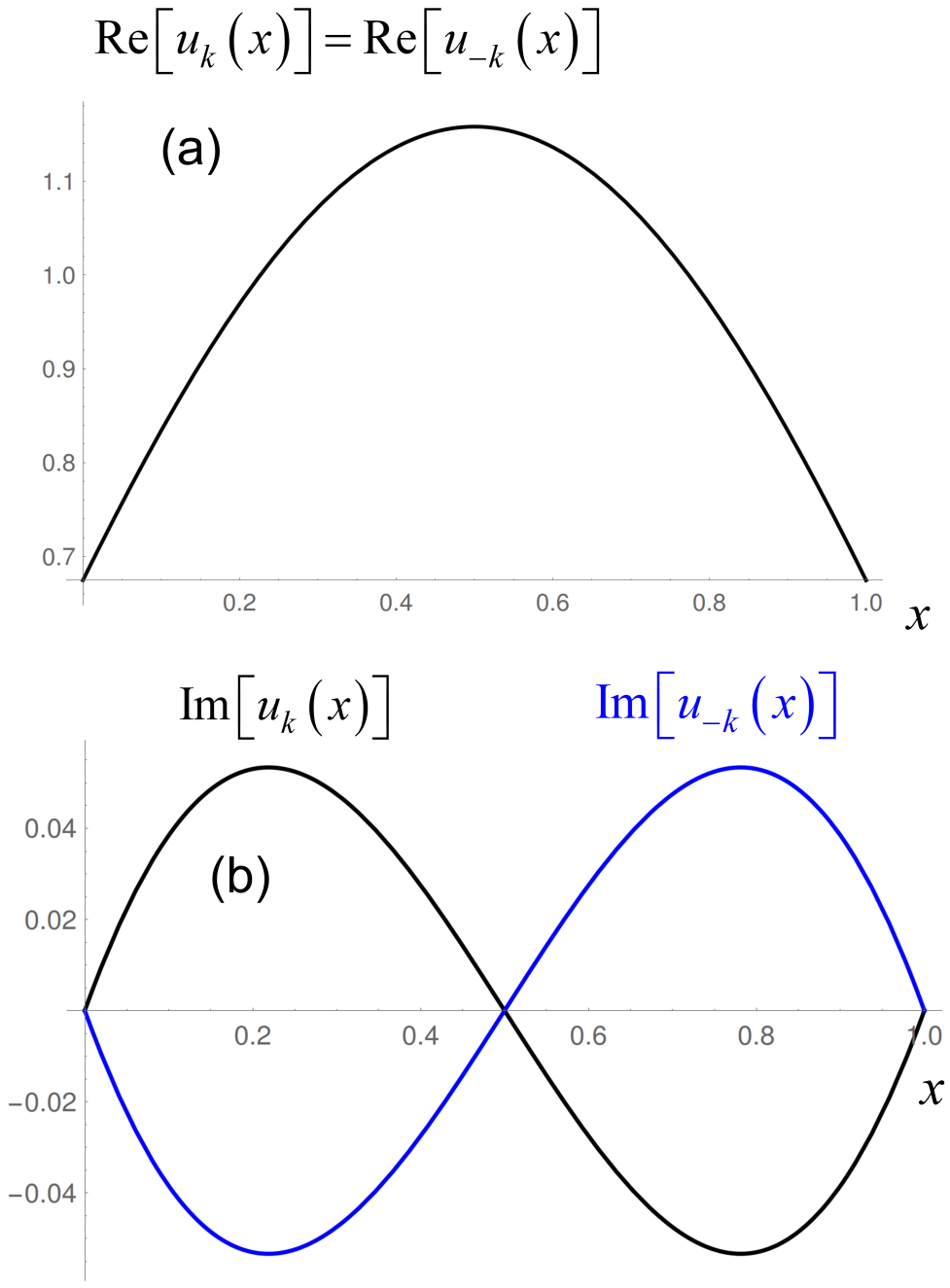

Figure 2.3: (a) Real part and (b) imaginary part of the function $u_{\nu,k}(x)$ for $0 \leq x \leq 1$ for the Bloch function $\psi_{\nu,k}(x) = e^{ikx}u_{\nu,k}(x)$ in Eq. (2.28) for $\varepsilon = 5$. Here $\omega = 2$, i.e., $k = k(2)$ and $\nu = 1$ (see Figure 2.7 below).

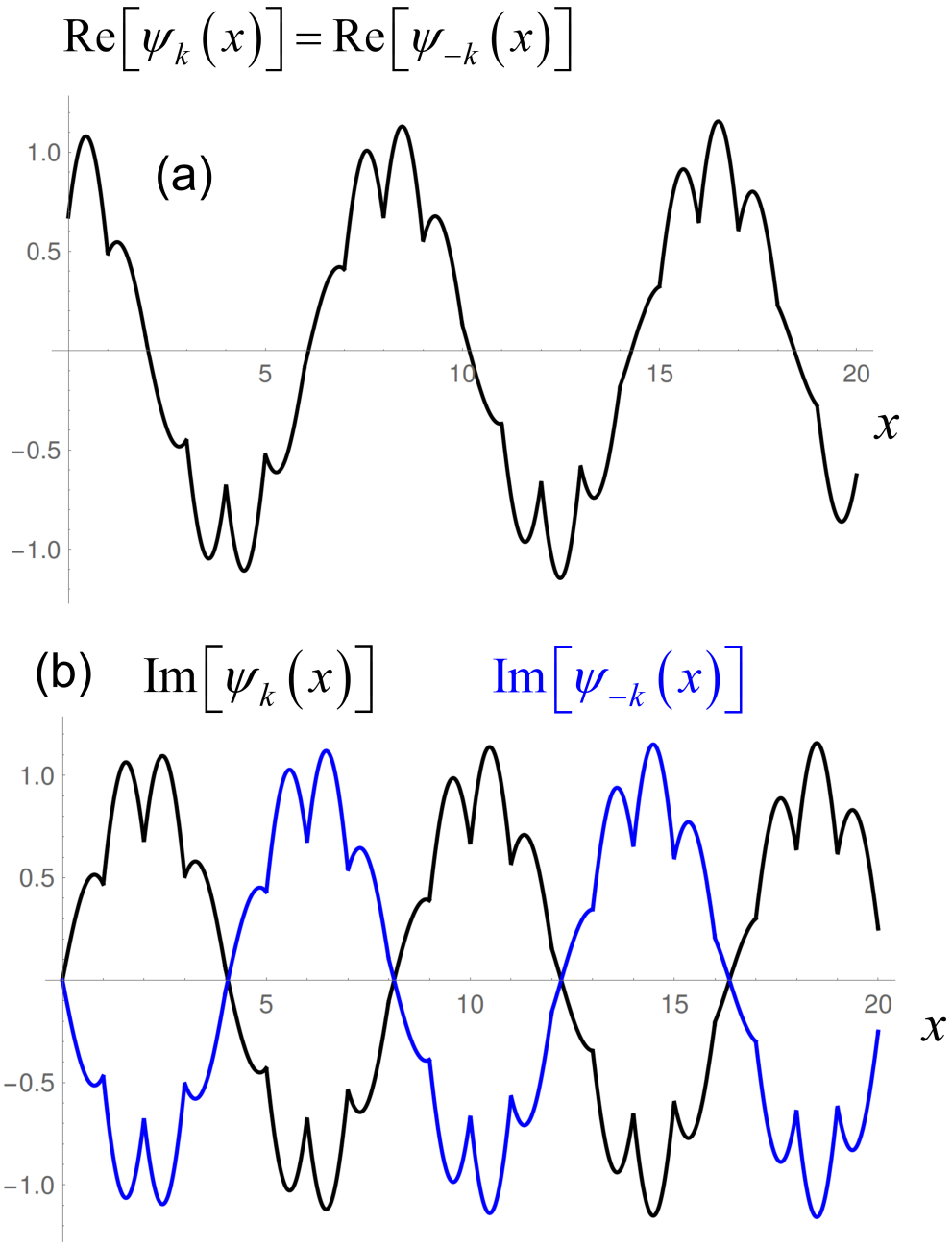

Figure 2.4: (a) Real part and (b) imaginary part of the Bloch function $\psi_{\nu,k}(x) = e^{ikx}u_{\nu,k}(x)$ in Eq. (2.28). Parameter values as in Figure 2.3.

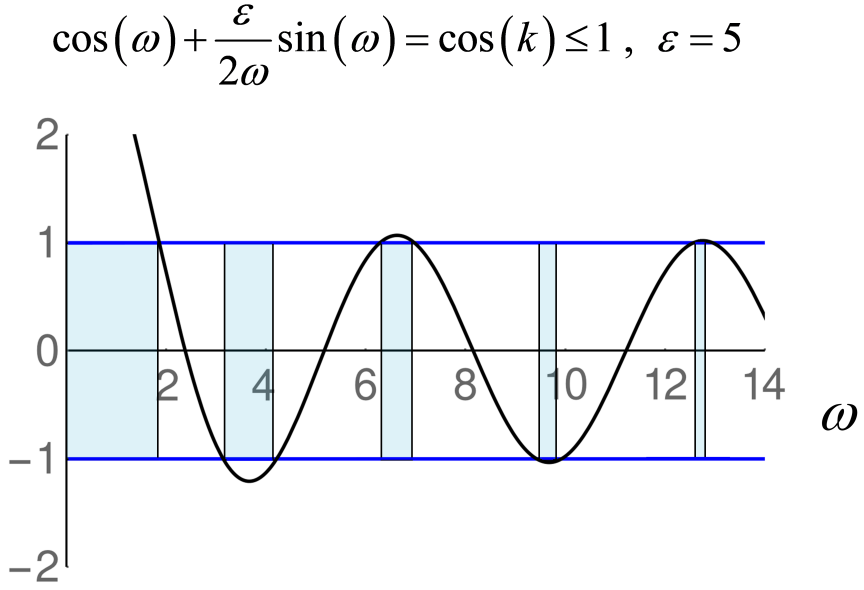

Figure 2.5: Frequency bands and gaps for the Kronig-Penney-type model defined by Eqs. (2.25) and (2.26). Shown is the function $f(\omega) = \cos\omega + \frac{\varepsilon}{2\omega}\sin\omega$ for $\varepsilon = 5$. The relation $f(\omega) = \cos(k)$ can be satisfied for real k if and only if $|f(\omega)| \le 1$ (see Eq. (2.31)). Modes with $|f(\omega)| \le 1$ are allowed and can freely propagate through the one-dimensional periodic structure (see Figure 2.2). Modes with $|f(\omega)| > 1$ decay exponentially and are therefore forbidden, resulting in frequency gaps (shown shaded in the figure).

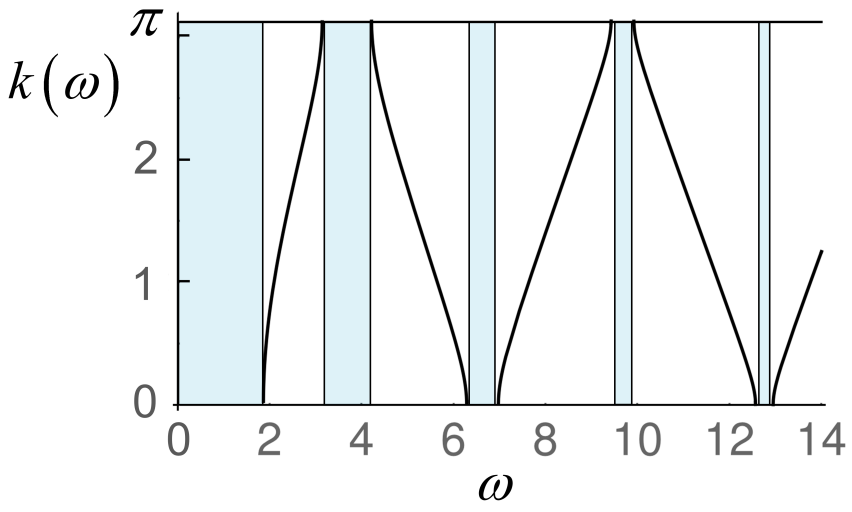

Figure 2.6: Inverse dispersion relation $k(\omega) \in [0, \pi]$ for allowed frequencies ω given by Eq. (2.32) for $\varepsilon = 5$. The band gaps are shown shaded.

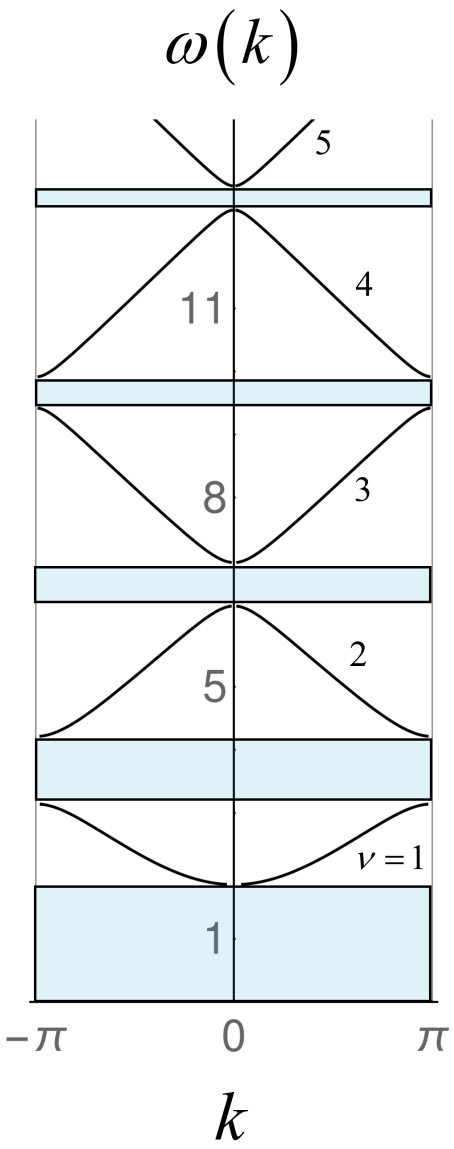

Figure 2.7: Dispersion relation $\omega(k)$ with frequency bands ν resulting from $\cos k = \cos\omega + \frac{\varepsilon}{2\omega}\sin\omega$ for $\varepsilon = 5$ in the reduced zone scheme (see Eq. (2.32)). The frequency gaps are shown shaded. The k-interval $[-\pi, \pi]$ is the first Brillouin zone of the reciprocal lattice in unitless variables where the lattice constant is equal to 1. Modes with $k > 0$ are moving to the right and modes with $k < 0$ are moving to the left.

2.3.1 Dynamic flux field in second-quantized form

We start this Section using original variables for clarity, and later turn to unitless variables to simplify the notation and facilitate the numerical implementation. For each section n of the CPW between SQUIDs $n-1$ and n we expand the field operator $\hat{\Phi}(x,t)$ introduced below Eq. (2.9), with time-dependent boundary conditions (2.14) at the SQUID sites $x_n = n\ell$, in second quantized form using annihilation and creation operators $\hat{a}_n(\nu,k)$ and $\hat{a}_n^\dagger(\nu,k)$ for wave vector k and frequency band ν (see Figure 2.10 on page 44 for a depiction of sites n and sections n of the SQUID array):

$$\hat{\Phi}_n(x,t) = \sqrt{\frac{\hbar}{2C_0}} \sum_{\nu=1}^{\infty} \int_{-\pi/\ell}^{\pi/\ell} \frac{dk}{2\pi} \frac{1}{\sqrt{\omega_\nu(k)}} \left[\hat{a}_n(\nu,k)\psi_{\nu,k}(x)\, e^{-i\omega_\nu(k)t} + \hat{a}_n^\dagger(\nu,k)\psi_{\nu,k}^*(x)\, e^{i\omega_\nu(k)t} \right] , \quad x_{n-1} < x < x_n , \tag{2.35}$$

where $\psi_{\nu,k}(x)$ are Bloch functions with dispersion relation $\omega_\nu(k)$ defined for the *static* system, and the k-integration is over the first Brillouin zone $\left[-\frac{\pi}{\ell}, \frac{\pi}{\ell}\right]$ of the reciprocal lattice (see Section 2.2.3). The Bloch functions have the form (see Eq. (2.28))

$$\psi_{\nu,k}(x) = e^{ikx} u_{\nu,k}(x) , \tag{2.36}$$

where $u_{\nu,k}(x)$ has period ℓ so that $u_{\nu,k}(x+n\ell) = u_{\nu,k}(x)$ for all integers n. The Bloch functions $\psi_{\nu,k}(x)$ are unitless, orthogonal with respect to the 1D wave vector k, normalized such that

$$\int_{-\infty}^{\infty} dx\, \psi_{\nu,k}^*(x)\psi_{\nu',k'}(x) = 2\pi\, \delta_{\nu\nu'}\, \delta(k-k') , \tag{2.37}$$

and fulfill the completeness relation

$$\sum_{\nu=1}^{\infty} \int_{-\pi/\ell}^{\pi/\ell} \frac{dk}{2\pi}\, \psi_{\nu,k}(x)\psi_{\nu,k}^*(x') = \delta(x-x') . \tag{2.38}$$

The index n in Eq. (2.35) indicates that $\hat{\Phi}_n(x,t)$ is defined in the domain $x_{n-1} < x < x_n$ corresponding to section n of the CPW. Field operators $\hat{\Phi}_n(x,t)$, $\hat{\Phi}_{n+1}(x,t)$ in subsequent sections n, $n+1$ are coupled to each other by the time-dependent boundary condition (2.14) at SQUID site x_n. The operators $\hat{a}_n(\nu,k)$, $\hat{a}_n^\dagger(\nu,k)$ in Eq. (2.35) can be interpreted as expansion coefficients of $\hat{\Phi}_n(x,t)$ in Bloch modes $\psi_{\nu,k}(x)\exp[-i\omega_\nu(k)t]$ in section n. Conversely, the Bloch functions $\psi_{\nu,k}(x)$ are defined for the global system by construction and do not depend on n.

For each section n of the CPW the annihilation and creation operators in Eq. (2.35) obey the commutation relations

$$\begin{aligned} \left[\hat{a}_n(\nu,k),\hat{a}_n^\dagger(\nu',k')\right] &= 2\pi\delta_{\nu\nu'}\,\delta(k-k')\,, \\ \left[\hat{a}_n(\nu,k),\hat{a}_n(\nu',k')\right] &= \left[\hat{a}_n^\dagger(\nu,k),\hat{a}_n^\dagger(\nu',k')\right] = 0\,, \end{aligned} \tag{2.39}$$

and have units of length$^{1/2}$. The prefactor $\sqrt{\dfrac{\hbar}{2C_0}}$ in Eq. (2.35) is determined by the equal-time commutation relation for section n of the CPW, $\left[\hat{\Phi}_n(x,t),\hat{\tilde{P}}_n(x',t)\right] = i\hbar\delta(x-x')$ in Eq. (2.12), using Eqs. (2.39) and (2.38).

The dispersion relation $\omega_\nu(k)$ used in Eq. (2.35) cannot be calculated in closed form. Conversely, the inverse function $k(\omega)\in[0,\pi]$ is uniquely defined for given $\omega=\omega_\nu$ and is directly available in analytical form by Eq. (2.32) (see Figure 2.6) [6]. It is therefore convenient to perform a substitution of integration variables $k\to\omega$ in Eq. (2.35), which gives

$$\begin{aligned} \hat{\Phi}_n(x,t) = \sqrt{\frac{\hbar}{2C_0}} \int_{0,\,\text{w/o gaps}}^{\infty} \frac{d\omega}{2\pi} \left|\frac{dk}{d\omega}\right| \frac{1}{\sqrt{\omega}} \\ \times \Big[\hat{a}_n[\nu,k(\omega)]\,\psi_{\nu,k(\omega)}(x)\,e^{-i\omega t} + \hat{a}_n^\dagger[\nu,k(\omega)]\,\psi^*_{\nu,k(\omega)}(x)\,e^{i\omega t} \\ + \hat{a}_n[\nu,-k(\omega)]\,\psi_{\nu,-k(\omega)}(x)\,e^{-i\omega t} + \hat{a}_n^\dagger[\nu,-k(\omega)]\,\psi^*_{\nu,-k(\omega)}(x)\,e^{i\omega t}\Big]\,, \end{aligned} \tag{2.40}$$

[6] In what follows, $k(\omega)\in[0,\pi]$ denotes the *positive* solution for k of Eq. (2.30) in the reduced zone scheme given by Eq. (2.32) and Figure 2.6.

where $\left|\frac{dk}{d\omega}\right|$ is the Jacobian for the transformation $k \to \omega$ and the integration is over all positive frequencies $\omega > 0$ excluding the frequency gaps of the band structure (see Figure 2.6). We may rewrite Eq. (2.40) as

$$\begin{aligned}\hat{\Phi}_n(x,t) = \sqrt{\frac{\hbar}{2C_0}} \int_{0,\,\text{w/o gaps}}^{\infty} \frac{d\omega}{2\pi} \left|\frac{dk}{d\omega}\right|^{1/2} \frac{1}{\sqrt{\omega}} \\ \times \Big[\hat{a}_n^R(\omega)\psi_\omega^R(x)\,e^{-i\omega t} + \hat{a}_n^{R\dagger}(\omega)\psi_\omega^{R*}(x)\,e^{i\omega t} \\ + \hat{a}_n^L(\omega)\psi_\omega^L(x)\,e^{-i\omega t} + \hat{a}_n^{L\dagger}(\omega)\psi_\omega^{L*}(x)\,e^{i\omega t} \Big] ,\end{aligned} \tag{2.41}$$

where we defined (note that $k(\omega) > 0$ by convention, see footnote 6 on page 26)

$$\hat{a}_n^R(\omega) := \left|\frac{dk}{d\omega}\right|^{1/2} \hat{a}_n[\nu, k(\omega)] \ , \ \psi_\omega^R(x) := \psi_{\nu,k(\omega)}(x) \ , \ \text{moving to the right (R)} \ , \tag{2.42a}$$

$$\hat{a}_n^L(\omega) := \left|\frac{dk}{d\omega}\right|^{1/2} \hat{a}_n[\nu, -k(\omega)] \ , \ \psi_\omega^L(x) := \psi_{\nu,-k(\omega)}(x) \ , \ \text{moving to the left (L)} \ . \tag{2.42b}$$

Note that by using ω as the independent variable, the band index ν is specified by the value of $\omega = \omega_\nu$ (see Figure 2.7). The prefactors of $\left|\frac{dk}{d\omega}\right|^{1/2}$ in Eq. (2.42) are introduced so that the commutation relations (2.39) for $\hat{a}_n(k)$ result in the corresponding commutation relations in ω-space,

$$\left[\hat{a}_n^R(\omega), \hat{a}_n^{R\dagger}(\omega')\right] = 2\pi\delta(\omega - \omega') \ , \tag{2.43a}$$

$$\left[\hat{a}_n^L(\omega), \hat{a}_n^{L\dagger}(\omega')\right] = 2\pi\delta(\omega - \omega') \ , \tag{2.43b}$$

$$\left[\hat{a}_n^L(\omega), \hat{a}_n^{R\dagger}(\omega')\right] = 0 \ , \text{ etc.} \ , \tag{2.43c}$$

and $\hat{a}_n(\omega)$ has units of time$^{1/2}$.

We now rewrite Eq. (2.41) in terms of unitless variables by expressing lengths in units of ℓ and times in units of ℓ/v as discussed in Section 2.2.1:

$$\begin{aligned}\hat{\phi}_n(x,t) = &\int_{0,\,\text{w/o gaps}}^{\infty} \frac{d\omega}{2\pi} \left|\frac{dk}{d\omega}\right|^{1/2} \frac{1}{\sqrt{\omega}} \\ &\times \Big[\hat{a}_n^R(\omega)\psi_\omega^R(x)\,e^{-i\omega t} + \hat{a}_n^{R\dagger}(\omega)\psi_\omega^{R*}(x)\,e^{i\omega t} \\ &+ \hat{a}_n^L(\omega)\psi_\omega^L(x)\,e^{-i\omega t} + \hat{a}_n^{L\dagger}(\omega)\psi_\omega^{L*}(x)\,e^{i\omega t}\Big]\,, \quad n-1<x<n\,,\end{aligned} \tag{2.44}$$

with the unitless field operator in section n of the periodic array (see Figure 2.10 on page 44)

$$\hat{\phi}_n(x,t) := \sqrt{\frac{2C_0 v}{\hbar}}\,\hat{\Phi}_n(x,t)\,, \quad n-1<x<n\,. \tag{2.45}$$

Unitless annihilation and creation operators in ω-space are defined by $\sqrt{\frac{v}{\ell}}\,\hat{a}_n(\omega)$ and $\sqrt{\frac{v}{\ell}}\,\hat{a}_n^\dagger(\omega)$, respectively, and again denoted by $\hat{a}_n(\omega)$ and $\hat{a}_n^\dagger(\omega)$ to keep the notation simple. They obey the same commutation relations as in Eq. (2.43) (where ω is now unitless). Note that all variables in Eq. (2.44) are made unitless by expressing lengths in units of ℓ and times in units of ℓ/v. The following results are then valid for any general system exhibiting time-dependent harmonic modulations in a periodic lattice. The variables that are unique to our superconducting circuit setup are the speed of propagation in the CPW v, the length of the CPW sections (lattice constant) ℓ, and the unitless variable ε in Eq. (2.19), which determines the strength of the potential encountered at our SQUID sites. It follows that the subsequent analysis applies to any other physical realization with corresponding physical values of ℓ, v, and ε.

Equation (2.44) incorporates our strategy to find the radiation created by the dynamical Casimir effect (DCE) in the SQUID array with time-dependent drive, Eq. (2.4). In each section n of the array, the flux field $\hat{\phi}_n(x,t)$ for $n-1<x<n$ is expanded in right-moving (R) and left-moving (L) Bloch waves $\psi_\omega^R(x)$ and $\psi_\omega^L(x)$ obtained for the static case (see Section 2.2.3). The expansion coefficients $\hat{a}_n^R(\omega)$ and $\hat{a}_n^L(\omega)$ in subsequent sections n, $n+1$ are coupled in a nontrivial way by the time-dependent part $\delta E_{J,n}\cos(\Omega t+\varphi_n)$ of the boundary condition at site n in Eq. (2.4). The

expansion coefficients in section $n+1$ are found from the coefficients in section n from the boundary condition at site n by using a transfer matrix approach, which allows us to find the coefficients and therefore the flux field for the whole array by iteration (see Figure 2.10 on page 44).

2.3.2 Frequency modes

The next step will be to relate the operators $\hat{a}_n^R(\omega)$, $\hat{a}_n^{R\dagger}(\omega)$, $\hat{a}_n^L(\omega)$, $\hat{a}_n^{L\dagger}(\omega)$ in Eq. (2.44) in subsequent sections n, $n+1$ by using the time-dependent boundary condition (2.14) at SQUID site n. For a general function $f(t)$ of time t we define its Fourier transform as

$$\widetilde{f}(\omega) := \int_{-\infty}^{\infty} dt\, f(t)\, \exp(i\omega t) \tag{2.46}$$

and the inverse transformation

$$f(t) := \int_{-\infty}^{\infty} \frac{d\omega}{2\pi}\, \widetilde{f}(\omega)\, \exp(-i\omega t)\,. \tag{2.47}$$

Note that the integral in Eq. (2.47) includes both positive and negative frequencies ω whereas the integral in Eq. (2.44) is restricted to positive frequencies $\omega > 0$. However, one may rewrite the integral in Eq. (2.44) to include both positive and negative frequencies ω by associating the terms containing the adjoint operators $\hat{a}_n^{R\dagger}(\omega)$ and $\hat{a}_n^{L\dagger}(\omega)$ with negative frequencies [15]:

$$\hat{a}_n^R(-\omega)\,\psi_{-\omega}^R(x)\,e^{-i(-\omega)t} := \hat{a}_n^{R\dagger}(\omega)\,\psi_\omega^{R*}(x)\,e^{i\omega t} \quad \text{for } \omega > 0\,, \tag{2.48}$$

which implies for $\omega < 0$

$$\hat{a}_n^R(\omega) = \hat{a}_n^{R\dagger}(|\omega|)\,, \quad \psi_\omega^R(x) = \psi_{|\omega|}^{R*}(x) \quad \text{for } \omega < 0\,. \tag{2.49}$$

Thus, positive frequencies $\omega > 0$ are associated with operators $\hat{a}(\omega)$ and Bloch functions ψ_ω whereas negative frequencies $\omega < 0$ are associated with operators $\hat{a}^\dagger(|\omega|)$ and Bloch functions $\psi_{|\omega|}^*$ (compare Figure 2.8 on page 38). Similar definitions apply for modes traveling to the left (L). Using

Eq. (2.48) we can write

$$\begin{aligned}
&\int_{0,\,\text{w/o gaps}}^{\infty} \frac{d\omega}{2\pi} \left|\frac{dk}{d\omega}\right|^{1/2} \frac{1}{\sqrt{\omega}}\, \hat{a}_n^{R\dagger}(\omega)\psi_\omega^{R*}(x)\, e^{i\omega t} \\
&= \int_{-\infty,\,\text{w/o gaps}}^{0} \frac{d\omega}{2\pi} \left|\frac{dk}{d\omega}\right|^{1/2} \frac{1}{\sqrt{|\omega|}}\, \hat{a}_n^{R}(\omega)\psi_\omega^{R}(x)\, e^{-i\omega t}
\end{aligned} \tag{2.50}$$

where the integral on the r.h.s. is over the domain of negative frequencies $\{-\omega : \omega > 0, \text{w/o gaps}\}$, corresponding to a point reflection of the domain of the integral on the l.h.s. at $\omega = 0$ to negative values. Using a similar definition for modes moving to the left (L), and using definition (2.47) for the Fourier transform, we may rewrite Eq. (2.44) in compact form as

$$\begin{aligned}
\hat{\phi}_n(x,t) &= \int_{-\infty,\,\text{w/o gaps}}^{\infty} \frac{d\omega}{2\pi} \left|\frac{dk}{d\omega}\right|^{1/2} \frac{1}{\sqrt{|\omega|}} \\
&\qquad \times \left[\hat{a}_n^{R}(\omega)\psi_\omega^{R}(x) + \hat{a}_n^{L}(\omega)\psi_\omega^{L}(x)\right] e^{-i\omega t} \\
&= \int_{-\infty,\,\text{w/o gaps}}^{\infty} \frac{d\omega}{2\pi}\, \hat{\phi}_n(x,\omega)\, e^{-i\omega t}\,,
\end{aligned} \tag{2.51}$$

where [7]

$$\hat{\phi}_n(x,\omega) = \hat{\phi}_n^{R}(x,\omega) + \hat{\phi}_n^{L}(x,\omega) \tag{2.52}$$

with the frequency modes moving to the right (R) and left (T) in section $n-1 < x < n$:

$$\hat{\phi}_n^{R}(x,\omega) = \left|\frac{dk}{d\omega}\right|^{1/2} \frac{1}{\sqrt{|\omega|}}\, \hat{a}_n^{R}(\omega)\psi_\omega^{R}(x) \tag{2.53a}$$

$$\hat{\phi}_n^{L}(x,\omega) = \left|\frac{dk}{d\omega}\right|^{1/2} \frac{1}{\sqrt{|\omega|}}\, \hat{a}_n^{L}(\omega)\psi_\omega^{L}(x)\,. \tag{2.53b}$$

We recall that the modes in Eq. (2.53) are defined for both positive and negative frequencies ω, where negative frequencies $\omega < 0$ produce the adjoint operator $\hat{a}^\dagger$ and complex conjugate ψ^* as shown in Eq. (2.49). The frequency gaps in Eq. (2.51) can be reconciled with the definition (2.47)

[7] We omit the tilde symbol for the Fourier transform to the keep the notation simple.

of the Fourier transform by setting the integrand in Eq. (2.51) to zero at values of ω that fall in frequency gaps.

2.3.3 Incorporation of the boundary condition at the SQUID sites: Static case

In the static case, where $\delta E_{J,n} = 0$ in Eq. (2.4) and the SQUID energy $E_{J,n} = E_J^0$ is constant, there are two boundary conditions for the frequency modes $\hat{\phi}_n(x,\omega)$ in Eq. (2.52) at SQUID site n (see Section 2.2 and Figure 2.10 on page 44):

1. The (unitless) field operator $\hat{\phi}(x,\omega)$ is continuous at the SQUID sites n:

$$\hat{\phi}_n(x,\omega)\big|_{x=n} = \hat{\phi}_{n+1}(x,\omega)\big|_{x=n} \quad \text{for all integer } n\,. \tag{2.54}$$

2. The first derivative $\hat{\phi}'(x,\omega) := \partial\hat{\phi}(x,\omega)/\partial x$ jumps at the SQUID sites n according to Eq. (2.26) with ε from Eq. (2.19):

$$\varepsilon\hat{\phi}_n(n,\omega) = \hat{\phi}'_{n+1}(n,\omega) - \hat{\phi}'_n(n,\omega) \quad \text{for all integer } n\,. \tag{2.55}$$

   This boundary condition couples $\hat{\phi}_n$ and $\hat{\phi}_{n+1}$ because the derivative in the first term on the r.h.s. of Eq. (2.55) is taken in section $n+1$ (where $n < x < n+1$) whereas the derivative in the second term is taken in section n (where $n-1 < x < n$) (see Figure 2.10 on page 44).

Since by construction the Bloch functions $\psi^R_\omega(x)$, $\psi^L_\omega(x)$ solve the wave equation (2.25) for the flux field with the boundary conditions (2.54), (2.55) in the entire system (see Section 2.2.3), in the static case the solution for the flux field $\hat{\phi}(x,\omega)$ in the entire system is simply a superposition of non-interacting Bloch modes:

$$\hat{\phi}(x,t) = \int_{-\infty,\,\text{w/o gaps}}^{\infty} \frac{d\omega}{2\pi} \left|\frac{dk}{d\omega}\right|^{1/2} \frac{1}{\sqrt{|\omega|}} \left[\hat{a}^R(\omega)\psi^R_\omega(x) + \hat{a}^L(\omega)\psi^L_\omega(x)\right] e^{-i\omega t}\,, \tag{2.56}$$

where $\hat{a}^R(\omega)$, $\hat{a}^L(\omega)$ are now *global* coefficients (equal for all sections n of the CPW) and given by external conditions (e.g., radiation entering the system from outside, thermal radiation, etc.). For classical light, systems of this type are realized in photonic crystals [12], which consist of periodic dielectric nanostructures that affect the motion of photons in a similar way that periodic crystal lattices affect the motion of electrons in solids (see Section 2.2)

Similar descriptions of quantum fields as an expansion of Bloch modes has been employed in the study of quantum electrodynamics in photonic crystals. Some recent examples are [10], where a QED treatment is used to study the Lamb shift of atoms placed in a photonic crystal medium, and [9] where ionization energy of atoms in a photonic crystal is explored.

2.3.4 Incorporation of the boundary condition at the SQUID sites: Harmonic drive

We now consider a time-dependent applied magnetic flux through the SQUIDs in the form of a harmonic drive, which results in the SQUID energy $E_{J,n}(t) = E_J^0 + \delta E_{J,n}\cos(\Omega t + \varphi_n)$ in Eq. (2.4). From Eq. (2.14) and using unitless variables, we obtain the boundary condition for the (unitless) field operator $\hat{\phi}(x,t)$ introduced in Eq. (2.45):

$$\varepsilon\hat{\phi}(n,t) + \delta\varepsilon_n(t)\,\hat{\phi}(n,t) + \hat{\phi}'(n^-,t) - \hat{\phi}'(n^+,t) = 0 \quad \text{for all integer } n \tag{2.57}$$

with $\varepsilon = \ell\left(\frac{2\pi}{\Phi_0}\right)^2 E_J^0 L_0$ from Eq. (2.19),

$$\delta\varepsilon_n(t) = \delta\varepsilon_n^0\cos(\Omega t + \varphi_n) \tag{2.58}$$

with the unitless amplitude from Eq. (2.34)

$$\delta\varepsilon_n^0 = \ell\left(\frac{2\pi}{\Phi_0}\right)^2 \delta E_{J,n} L_0\,, \tag{2.59}$$

and we omitted a term proportional to C_J as discussed below Eq. (2.18).

We now show how the time-dependent boundary condition (2.57) results in a coupling between $\hat{a}$ operators in subsequent sections n, $n+1$ of the array. Fourier transforming the first, third and fourth terms in Eq. (2.57) to frequency space according to Eq. (2.46) (for fixed positive $\omega > 0$) results in frequency modes $\hat{\phi}_n(n,\omega)$, $\hat{\phi}'_n(n,\omega)$, $\hat{\phi}'_{n+1}(n,\omega)$ as in the static case, with $\hat{\phi}_n(x,\omega)$ from Eq. (2.52). However, Fourier transforming the second term in Eq. (2.57) (for fixed positive $\omega > 0$) results in a convolution integral in frequency space:

$$\int_{-\infty}^{\infty} dt\, \delta\varepsilon_n(t)\, \hat{\phi}_n(n,t)\, \exp(i\omega t) = \int_{-\infty,\,\text{w/o gaps}}^{\infty} d\mu \sqrt{\frac{|\mu|}{|\omega|}}\, \delta g_n(\omega,\mu)\, \hat{\phi}_n(n,\mu) \tag{2.60}$$

where

$$\delta g_n(\omega,\mu) := \frac{1}{2\pi}\sqrt{\frac{|\omega|}{|\mu|}} \int_{-\infty}^{\infty} dt\, \delta\varepsilon_n(t)\, \exp\left[i(\omega-\mu)t\right] . \tag{2.61}$$

The factor of $\frac{1}{2\pi}\sqrt{\frac{|\omega|}{|\mu|}}$ in Eq. (2.61) has been introduced for convenience. Using Eq. (2.60) the time-dependent boundary condition in Eq. (2.57) reads in ω-space

$$\varepsilon\hat{\phi}_n(n,\omega) + \hat{\phi}'_n(n,\omega) - \hat{\phi}'_{n+1}(n,\omega) + \int_{-\infty,\,\text{w/o gaps}}^{\infty} d\mu \sqrt{\frac{|\mu|}{|\omega|}}\, \delta g_n(\omega,\mu)\, \hat{\phi}_n(n,\mu) = 0 \tag{2.62}$$

with $\hat{\phi}_n(x,\omega)$ from Eq. (2.52) and the prime denotes a derivative $\frac{\partial}{\partial x}$ evaluated at n. We now use the fact that the Bloch functions $\psi^R_\omega(x)$ and $\psi^L_\omega(x)$ in the definition of $\hat{\phi}_n(x,\omega)$ in Eqs. (2.52) and (2.53) fulfill the boundary condition in Eq. (2.26) for the static case, i.e., $\varepsilon\psi_\omega(n) + \psi'_\omega(n^-) = \psi'_\omega(n^+)$. Using this in Eq. (2.62) we find (for fixed positive $\omega > 0$)

$$\begin{aligned} &\left|\frac{dk}{d\omega}\right|^{1/2} \left[\hat{a}^R_n(\omega) - \hat{a}^R_{n+1}(\omega)\right] \psi^{R'}_\omega(n^+) + \left|\frac{dk}{d\omega}\right|^{1/2} \left[\hat{a}^L_n(\omega) - \hat{a}^L_{n+1}(\omega)\right] \psi^{L'}_\omega(n^+) \\ &+ \int_{-\infty,\,\text{w/o gaps}}^{\infty} d\mu \left|\frac{dk}{d\mu}\right|^{1/2} \delta g_n(\omega,\mu) \left[\hat{a}^R_n(\mu)\psi^R_\mu(n) + \hat{a}^L_n(\mu)\psi^L_\mu(n)\right] = 0 . \end{aligned} \tag{2.63}$$

Note that Eq. (2.63) couples operators $\hat{a}_n(\omega)$, $\hat{a}_{n+1}(\omega)$ in subsequent sections n, $n+1$ of the array in a nontrivial way due to the integral term. The derivative $\psi'_\omega(n^+)$ of the Bloch functions is calculated at site n from the right. In the following sections we devise a scheme to solve Eq. (2.63) numerically as a matrix equation for an harmonic drive $\delta\varepsilon_n(t) = \delta\varepsilon_n^0 \cos(\Omega t + \varphi_n)$ in Eq. (2.61).

Bloch functions at the SQUID sites We recall that the Bloch functions in Eq. (2.63) are given in terms of the wave vector $k(\omega)$ by Eq. (2.42), where we defined $k(\omega) > 0$ by convention (see Eq. (2.32) and footnote 6 on page 26). To avoid confusion regarding the sign of k in future calculations, let us define explicitly

$$K := |k| > 0 \ , \quad K(\omega) := |k(\omega)| > 0 \ , \tag{2.64}$$

so that $k = K$ if $k > 0$ and $k = -K$ if $k < 0$. We thus obtain for $\omega > 0$ [8]

$$\psi^R_\omega(x) = \psi_{K(\omega)}(x) = \exp\left[iK(\omega)x\right] u_{K(\omega)}(x) \ , \quad \text{moving to the right (R)} \ , \tag{2.65a}$$

$$\psi^L_\omega(x) = \psi_{-K(\omega)}(x) = \exp\left[-iK(\omega)x\right] u^*_{K(\omega)}(x) \ , \quad \text{moving to the left (L)} \ , \tag{2.65b}$$

where in the second line we used $u_{-K}(x) = u^*_K(x)$. For $\omega < 0$ we obtain, using Eq. (2.49),

$$\psi^R_\omega(x) = \psi^{R*}_{|\omega|}(x) = \exp\left[-iK(\omega)x\right] u^*_{K(\omega)}(x) \ , \quad \text{moving to the right (R)} \ , \tag{2.66a}$$

$$\psi^L_\omega(x) = \psi^{L*}_{|\omega|}(x) = \exp\left[iK(\omega)x\right] u_{K(\omega)}(x) \ , \quad \text{moving to the left (L)} \ . \tag{2.66b}$$

In Eq. (2.63) we need the values of the Bloch functions $\psi(x)$ and their derivatives at the SQUID sites n. Since $\psi(x) = \exp(iKx)u_K(x)$ and $\psi'(x) = \exp(iKx)\left[iKu_K(x) + u'_K(x)\right]$ we define

[8] To keep the notation simple, in this section we omit the band index ν. It is understood that a frequency band is uniquely specified by k and ν, or by $\omega = \omega_\nu$. See Eq. (2.42) in Section 2.3.1.

$$\mathscr{C}_K := u_K(0) = u_K(1) = u_{-K}(0) = u_{-K}(1) \quad \text{real-valued} \tag{2.67a}$$

$$\mathscr{D}_K := \frac{d}{dx}\, u_K(x)|_{x=0^+} \ , \quad \mathscr{D}_{-K} = \mathscr{D}_K^* \, , \tag{2.67b}$$

$$\mathscr{A}_K := iK\mathscr{C}_K + \mathscr{D}_K \ , \quad \mathscr{A}_{-K} = \mathscr{A}_K^* \, . \tag{2.67c}$$

We define for $\omega > 0$

$$\mathscr{C}_\omega := \mathscr{C}_{K(\omega)} \ , \quad \mathscr{D}_\omega := \mathscr{D}_{K(\omega)} \ , \quad \mathscr{A}_\omega := \mathscr{A}_{K(\omega)} \ , \tag{2.68}$$

whereas for $\omega < 0$

$$\mathscr{C}_\omega = \mathscr{C}_{|\omega|} \ , \quad \mathscr{D}_\omega = \mathscr{D}_{|\omega|}^* \ , \quad \mathscr{A}_\omega = \mathscr{A}_{|\omega|}^* \, . \tag{2.69}$$

Note that $u_K(x)$ is defined in the domain $x \in [0,1]$ so that the derivative in Eq. (2.67b) is taken for $x > 0$ and evaluated at $x = 0$. The algebraic properties shown in Eq. (2.67) are verified in the Mathematica notebook in the Appendix. With these definitions, the Bloch functions and their derivatives at site n in Eq. (2.63) are given by, for $\omega > 0$,

$$\begin{aligned} &\psi_\omega^R(n) = \exp\left[iK(\omega)n\right] \mathscr{C}_\omega \ , \quad \psi_\omega^L(n) = \exp\left[-iK(\omega)n\right] \mathscr{C}_\omega \ , \\ &\psi_\omega^{R'}(n^+) = \exp\left[iK(\omega)n\right] \mathscr{A}_\omega \ , \quad \psi_\omega^{L'}(n^+) = \exp\left[-iK(\omega)n\right] \mathscr{A}_\omega^* \, , \end{aligned} \tag{2.70}$$

whereas for $\omega < 0$

$$\begin{aligned} &\psi_\omega^R(n) = \exp\left[-iK(\omega)n\right] \mathscr{C}_{|\omega|} \ , \quad \psi_\omega^L(n) = \exp\left[iK(\omega)n\right] \mathscr{C}_{|\omega|} \ , \\ &\psi_\omega^{R'}(n^+) = \exp\left[-iK(\omega)n\right] \mathscr{A}_{|\omega|}^* \ , \quad \psi_\omega^{L'}(n^+) = \exp\left[iK(\omega)n\right] \mathscr{A}_{|\omega|} \, . \end{aligned} \tag{2.71}$$

Position-dependent annihilation and creation operators From Eqs. (2.63) and (2.70) one can see that the operators $\hat{a}_n^R$ are associated with a phase factor $\exp(iKn)$ and operators $\hat{a}_n^L$ are associated with a phase factor $\exp(-iKn)$, where the phase factors come from the Bloch functions.

In future calculations it will be convenient to include this phase factor in the operators by defining position-dependent operators (for positive $\omega > 0$)

$$\hat{a}_n^R(\omega,x) := \hat{a}_n^R(\omega)\exp\left[iK(\omega)x\right] , \quad n-1 < x < n , \tag{2.72a}$$

$$\hat{a}_n^L(\omega,x) := \hat{a}_n^L(\omega)\exp\left[-iK(\omega)x\right] , \quad n-1 < x < n , \tag{2.72b}$$

with $\hat{a}_n^R(\omega)$, $\hat{a}_n^L(\omega)$ as defined in Eq. (2.42) [9]. Using the above definitions, Eq. (2.63) takes the form

$$\begin{aligned} &\left|\frac{dk}{d\omega}\right|^{1/2}\left[\hat{a}_n^R(\omega,n)-\hat{a}_{n+1}^R(\omega,n)\right]\mathscr{A}_\omega + \left|\frac{dk}{d\omega}\right|^{1/2}\left[\hat{a}_n^L(\omega,n)-\hat{a}_{n+1}^L(\omega,n)\right]\mathscr{A}_\omega^* \\ &+\int_{-\infty,\,\text{w/o gaps}}^{\infty} d\mu \left|\frac{dk}{d\mu}\right|^{1/2}\delta g_n(\omega,\mu)\,\mathscr{C}_\mu\left[\hat{a}_n^R(\mu,n)+\hat{a}_n^L(\mu,n)\right] = 0 . \end{aligned} \tag{2.73}$$

Implementation of the harmonic drive We now specify the kernel $\delta g_n(\omega,\mu)$ in Eq. (2.73) for the harmonic drive $\delta\varepsilon_n(t) = \delta\varepsilon_n^0\cos(\Omega t+\varphi_n)$ in Eq. (2.58). Using this form in Eq. (2.61) we find

$$\delta g_n(\omega,\mu) = \sqrt{\frac{|\omega|}{|\mu|}}\,\frac{\delta\varepsilon_n^0}{2}\left\{e^{i\varphi_n}\,\delta\left[\mu-(\omega+\Omega)\right]+e^{-i\varphi_n}\,\delta\left[\mu-(\omega-\Omega)\right]\right\} , \tag{2.74}$$

which implies that the frequency ω is scattered to $\omega\pm\Omega$ provided that the target frequencies $\omega\pm\Omega$ are allowed, i.e., do not fall in a frequency gap of the band structure (see Figure 2.8 on page 38). Thus, for given ω, the range of frequencies resulting from multiple scattering processes is confined to the discrete set $\{\omega+\alpha\,\Omega$ for integer $\alpha\}$. For our numerical implementation we need to limit this set to a finite number of elements. Taking into account that the range of frequencies can only include allowed frequencies, for given (allowed) frequency ω we define the range of frequencies due to multiple scattering processes as

$$\omega_\alpha = \omega + (N_u+1-\alpha)\,\Omega , \quad \alpha = 1,\ldots,M(\omega) \tag{2.75}$$

[9] The phase factor in Eq. (2.72) does not change the commutation relations (2.43).

where

$$M(\omega) = N_u(\omega) + N_l(\omega) + 1 \; . \tag{2.76}$$

Explicitly, the range of frequencies in Eq. (2.75) is given by

$$\begin{aligned}
&\omega_1 = \omega + N_u \, \Omega \\
&\omega_2 = \omega + (N_u - 1) \, \Omega \\
&\vdots \\
&\omega_\alpha = \omega \;\; \text{with} \;\; \alpha = N_u + 1 \\
&\vdots \\
&\omega_{M-1} = \omega - (N_l - 1) \, \Omega \\
&\omega_M = \omega - N_l \, \Omega \; .
\end{aligned} \tag{2.77}$$

The upper and lower boundaries N_u, N_l are defined as follows. For given frequency ω, $N_u(\omega)$ and $N_l(\omega)$ are the *maximum* integers $\in \{0, \ldots, N_{cut}\}$ so that *all* frequencies $\omega_1, \ldots, \omega_M$ in Eq. (2.77) are allowed. Thus, ω_1 is allowed but $\omega_1 + \Omega$ is not allowed, i.e., falls in a frequency gap. Similarly, ω_M is allowed but $\omega_M - \Omega$ is not allowed [10]. N_{cut} is an overall cutoff that limits N_u, N_l if the scattered frequencies do not fall in gaps within the range specified by N_{cut}. Note that $N_u(\omega)$, $N_l(\omega)$, $M(\omega)$ in Eq. (2.76) depend on the given frequency ω, whereas N_{cut} is a global cutoff and independent of ω.

Multiple scattering processes may lead from a positive initial frequency $\omega = \omega_\alpha$ (with $\alpha = N_u + 1$, see Eq. (2.77)) to negative frequencies $\omega_\beta < 0$. Negative frequencies turn creation and annihilation operators into their conjugate versions as shown in Eq. (2.48). It is this crossover from positive to negative frequencies and the associated conjugation of creation and annihilation operators that causes the DCE radiation, as will be shown in Section 2.4 below. For a graphical representation of the frequency jumps generated by these scattering processes, see Figure 2.8.

If for given ω a transition from positive to negative frequencies occurs within the range specified by Eq. (2.77), we use the special index κ for the *first* negative frequency $\omega_\kappa < 0$ found by

[10] We may call the set of frequencies in Eq. (2.77) the *largest simply connected frequency domain* that includes ω.

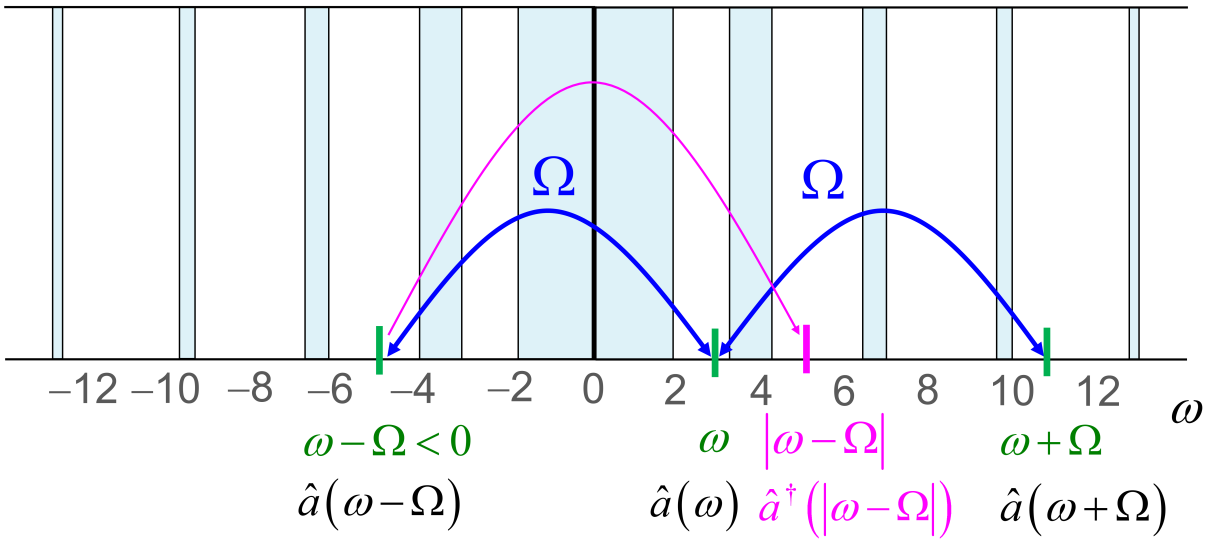

Figure 2.8: Band structure with frequency gaps (shown shaded) and possible transitions induced by an harmonic drive with frequency Ω (see Eq. (2.75)). The harmonic drive induces jumps from an allowed frequency ω in units of the drive frequency Ω (blue, here $\Omega = 8$) if the target frequencies $\omega \pm \Omega$ are allowed, i.e., do not fall in a band gap (green). In this figure the domain of positive frequencies $\omega > 0$ is extended to negative frequencies $\omega < 0$ by a point reflection at $\omega = 0$ (see text below Eq. (2.50) and compare Figure 2.7 on page 24). Physical radiation corresponds to positive frequencies $\omega > 0$. An operator $\hat{a}$ for a negative frequency $\omega - \Omega < 0$ thus transforms to the adjoint operator $\hat{a}^\dagger$ for positive frequency $|\omega - \Omega| > 0$ (magenta) (see Eqs. (2.48) and 2.49)). This process generates DCE radiation by virtue of the commutation relation $\left[\hat{a}, \hat{a}^\dagger\right] = 1$ (see Eq. (2.112)). In general, this type of process is described by a Bogoliubov transformation (see Section 1.1).

reading the table (2.77) from top to bottom. Thus

$$\begin{aligned} &\omega_1 > 0 \\ &\vdots \\ &\omega_{\kappa-1} > 0 \\ &\omega_\kappa < 0 \\ &\vdots \\ &\omega_M < 0 \ . \end{aligned} \tag{2.78}$$

Using the definitions above, denoting $\hat{a}_n^R(\alpha,n) \equiv \hat{a}_n^R(\omega_\alpha,n)$, etc., and using the abbreviation

$$d\omega(\alpha) := \left|\frac{dk}{d\omega_\alpha}\right|^{1/2} , \tag{2.79}$$

the boundary condition (2.73) at SQUID site n for given frequency $\omega = \omega_\alpha$ reads

$$\begin{aligned} &d\omega(\alpha)\left[\hat{a}_n^R(\alpha,n) - \hat{a}_{n+1}^R(\alpha,n)\right]\mathscr{A}_\alpha + d\omega(\alpha)\left[\hat{a}_n^L(\alpha,n) - \hat{a}_{n+1}^L(\alpha,n)\right]\mathscr{A}_\alpha^* \\ &+ \frac{\delta\varepsilon_n^0}{2}\sum_{\beta,\,\text{w/o gaps}} d\omega(\beta)\sqrt{\frac{|\omega_\alpha|}{|\omega_\beta|}}\mathscr{C}_\beta\left[e^{i\varphi_n}\delta_{\beta,\,\alpha+1} + e^{-i\varphi_n}\delta_{\beta,\,\alpha-1}\right]\left[\hat{a}_n^R(\beta,n) + \hat{a}_n^L(\beta,n)\right] = 0 \ . \end{aligned} \tag{2.80}$$

Vector notation and transfer matrix To write Eq. (2.80) in matrix form, for given ω with largest simply connected domain given by Eq. (2.77) we divide Eq. (2.80) by ε from Eq. (2.19) and define matrices $\delta G^{(n)}$ and A by [11]

$$\delta G_{\alpha\beta}^{(n)} := \frac{1}{2}\frac{\delta\varepsilon_n^0}{\varepsilon} d\omega(\beta)\sqrt{\frac{|\omega_\alpha|}{|\omega_\beta|}}\mathscr{C}_\beta\left[e^{i\varphi_n}\delta_{\beta,\,\alpha+1} + e^{-i\varphi_n}\delta_{\beta,\,\alpha-1}\right] , \tag{2.81}$$

[11] Note that Greek indices α, β, etc. label the set of frequencies ω_α in Eq. (2.77) whereas Latin indices n label the SQUID sites.

$$A_{\alpha\beta} := \frac{1}{\varepsilon} d\omega(\alpha)\, \delta_{\alpha\beta} \times \begin{cases} \mathscr{A}_\alpha \ , \ \omega_\alpha > 0 \\ \mathscr{A}_\alpha^* \ , \ \omega_\alpha < 0 \ . \end{cases} \tag{2.82}$$

Note that the matrix $\delta G^{(n)}$ in general depends on the SQUID site n in terms of the amplitude ε_n^0 and phase φ_n in $\delta\varepsilon_n(t) = \delta\varepsilon_n^0 \cos(\Omega t + \varphi_n)$ in Eq. (2.58). Furthermore, we combine annihilation operators for the frequencies in Eq. (2.77) to a vector

$$\vec{X}_R = \begin{pmatrix} \hat{a}_n^R(\omega_1, n) \\ \vdots \\ \hat{a}_n^R(\omega_{\kappa-1}, n) \\ \hat{a}_n^R(\omega_\kappa, n) \\ \vdots \\ \hat{a}_n^R(\omega_M, n) \end{pmatrix} = \begin{pmatrix} \hat{a}_n^R(\omega_1, n) \\ \vdots \\ \hat{a}_n^R(\omega_{\kappa-1}, n) \\ \hat{a}_n^{R\dagger}(|\omega_\kappa|, n) \\ \vdots \\ \hat{a}_n^{R\dagger}(|\omega_M|, n) \end{pmatrix} \tag{2.83}$$

where the index κ is defined in Eq. (2.78) and for the second equation we used Eq. (2.49). Note that the vector $\vec{X}_R$ is defined for section n of the SQUID array at position $x = n$, i.e., right at and to the left of SQUID n (see Figure 2.9). To simplify notation in the following discussion, we omit the index n for $\vec{X}_R$ and it is understood that $\vec{X}_R$ is an operator. In a completely analogous way as in Eq. (2.83) we define a vector $\vec{X}_L$ for left-moving modes (L).

In a similar way we define vectors $\vec{Y}_R$, $\vec{Y}_L$ for section $n+1$ of the SQUID array at position $x = n$, i.e., right at and to the right of SQUID n (see Figure 2.9):

$$\vec{Y}_R = \begin{pmatrix} \hat{a}_{n+1}^R(\omega_1, n) \\ \vdots \\ \hat{a}_{n+1}^R(\omega_{\kappa-1}, n) \\ \hat{a}_{n+1}^R(\omega_\kappa, n) \\ \vdots \\ \hat{a}_{n+1}^R(\omega_M, n) \end{pmatrix} = \begin{pmatrix} \hat{a}_{n+1}^R(\omega_1, n) \\ \vdots \\ \hat{a}_{n+1}^R(\omega_{\kappa-1}, n) \\ \hat{a}_{n+1}^{R\dagger}(|\omega_\kappa|, n) \\ \vdots \\ \hat{a}_{n+1}^{R\dagger}(|\omega_M|, n) \end{pmatrix} \tag{2.84}$$

and similarly for $\vec{Y}_L$. With these definitions, Eq. (2.80) becomes a matrix equation (omitting the index n for the matrix δG)

$$A\left(\vec{X}_R-\vec{Y}_R\right)+A^*\left(\vec{X}_L-\vec{Y}_L\right)+\delta G\left(\vec{X}_R+\vec{X}_L\right)=0\,, \tag{2.85}$$

which can be solved for the $\vec{Y}$ vectors as

$$A\vec{Y}_R+A^*\vec{Y}_L=A\vec{X}_R+A^*\vec{X}_L+\delta G\left(\vec{X}_R+\vec{X}_L\right)\,. \tag{2.86}$$

The condition that the flux field $\hat{\phi}(x,\omega)$ in Eq. (2.56) is continuous at the SQUID sites n gives a second boundary condition in matrix form, using Eqs. (2.70) and (2.72) (where a factor $\mathscr{C}_\omega$ cancels)

$$\vec{Y}_R+\vec{Y}_L=\vec{X}_R+\vec{X}_L\,. \tag{2.87}$$

The two equations (2.86), (2.87) can be solved $\vec{Y}_R$, $\vec{Y}_L$ in a straightforward way. The solution can be given in a compact form as follows. We combine the vectors for right-moving (R) and left-moving (L) modes to $2M$-vectors as

$$\underline{X}=\begin{pmatrix}\vec{X}_R\\ \vec{X}_L\end{pmatrix}\,,\quad \underline{Y}=\begin{pmatrix}\vec{Y}_R\\ \vec{Y}_L\end{pmatrix}\,, \tag{2.88}$$

and define a $2M\times 2M$ matrix S as

$$S=\begin{pmatrix}I+\mathscr{G} & \mathscr{G}\\ -\mathscr{G} & I-\mathscr{G}\end{pmatrix}\,, \tag{2.89}$$

where I is the identity matrix and the $M\times M$ matrix $\mathscr{G}$ is defined as

$$\mathscr{G}=\left(A-A^*\right)^{-1}\delta G\,. \tag{2.90}$$

The matrix $(A-A^*)^{-1}$ is diagonal with purely imaginary diagonal elements $\dfrac{\varepsilon\delta_{\alpha\beta}}{d\omega_\alpha\left(\mathscr{A}_\alpha-\mathscr{A}_\alpha^*\right)}$ where

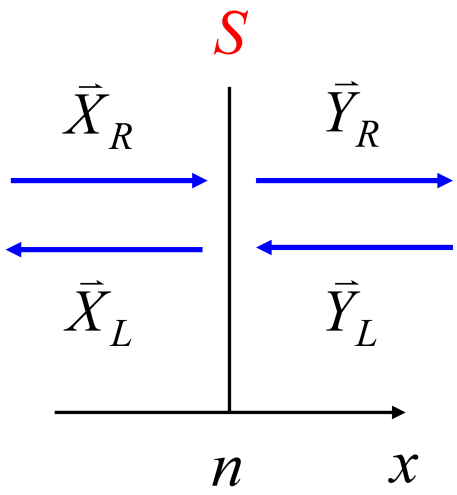

Figure 2.9: Matrix S transforming vectors $\vec{X}_R$, $\vec{X}_L$ on the left of SQUID site n to vectors $\vec{Y}_R$, $\vec{Y}_L$ on the right of SQUID site n according to Eq. (2.91). The directions of propagation of the associated operators are indicated by the blue arrows.

$\mathscr{A}_\alpha - \mathscr{A}_\alpha^* = \pm 2i\,[K(\omega_\alpha)\mathscr{C}_\alpha + \mathrm{Im}(\mathscr{D}_\alpha)]$ for $\omega_\alpha > 0$ $(+)$ or < 0 $(-)$ (see Eq. (2.82)). The solution for the $\vec{Y}$ vectors takes the compact form (see Figure 2.9)

$$\underline{Y} = S\underline{X}\,, \tag{2.91}$$

where both vectors are calculated at $x = n$ (but on opposite sides). Note that in the static case, where $\mathscr{G} = \delta G = \delta\varepsilon_n^0 = 0$, the matrix S in Eq. (2.89) reduces to the $2M \times 2M$ identity matrix, so that $\underline{Y}(x = n) = \underline{X}(x = n)$ for all SQUID sites n. This implies that the operators $\vec{a}_n$, $\vec{a}_{n+1}$ in the $\vec{X}$, $\vec{Y}$ vectors in Eqs. (2.83), (2.84) are equal for all n, and we recover the result in Eq. (2.56) found in the static case.

According to the definitions (2.83), (2.84), the matrix S in Eq. (2.91) maps operators $\hat{a}_n(\alpha, n)$ in section n of the SQUID array at position $x = n$ to operators $\hat{a}_{n+1}(\alpha, n)$ in section $n+1$ at position $x = n$, i.e., "transfers" the operators across the SQUID site n. In the next step we transfer the latter operators within section $n+1$ from position $x = n$ to $x = n+1$, i.e, from SQUIDs n to $n+1$.

According to Eq. (2.72) this transition is accompanied by phase factors

$$\vec{Y}_R(x=n+1) = \begin{pmatrix} \hat{a}^R_{n+1}(\omega_1,n+1) \\ \vdots \\ \hat{a}^R_{n+1}(\omega_{\kappa-1},n+1) \\ \hat{a}^{R\dagger}_{n+1}(|\omega_\kappa|,n+1) \\ \vdots \\ \hat{a}^{R\dagger}_{n+1}(|\omega_M|,n+1) \end{pmatrix} = \begin{pmatrix} \hat{a}^R_{n+1}(\omega_1,n)\exp[iK(\omega_1)] \\ \vdots \\ \hat{a}^R_{n+1}(\omega_{\kappa-1},n)\exp[iK(\omega_{\kappa-1})] \\ \hat{a}^{R\dagger}_{n+1}(|\omega_\kappa|,n)\exp[-iK(\omega_\kappa)] \\ \vdots \\ \hat{a}^{R\dagger}_{n+1}(|\omega_M|,n)\exp[-iK(\omega_M)] \end{pmatrix} = \mathscr{P}(1)\,\vec{Y}_R(x=n) \tag{2.92}$$

with the $M \times M$ diagonal matrix

$$\mathscr{P}(x) = \mathrm{diag}\left(\exp[iK(\omega_1)x],\ldots,\exp[iK(\omega_{\kappa-1})x],\exp[-iK(\omega_\kappa)x],\ldots,\exp[-iK(\omega_M)x]\right) . \tag{2.93}$$

Similarly we obtain $\vec{Y}_L(x=n+1) = \mathscr{P}^*(1)\,\vec{Y}_L(x=n)$. Defining the $2M \times 2M$ matrix P by

$$P(x) = \begin{pmatrix} \mathscr{P}(x) & 0 \\ 0 & \mathscr{P}^*(x) \end{pmatrix} \tag{2.94}$$

we thus obtain

$$\underline{Y}(x=n+1) = P(1)\,\underline{Y}(x=n) . \tag{2.95}$$

Thus, the matrix $P(1)$ transfers operators $\hat{a}_{n+1}(\alpha,n)$ in section $n+1$ at position $x=n$ to position $n+1$ corresponding to a displacement of 1 lattice constant ℓ. Combining Eqs. (2.91) and (2.94) we finally obtain

$$\underline{Y}_{n+1}(x=n+1) = P(1)\,S_n\underline{X}_n(x=n) =: T_n\underline{X}_n(x=n) , \tag{2.96}$$

with the transfer matrix

$$T_n = P(1)\,S_n . \tag{2.97}$$

In Eq. (2.96) we reintroduce indices to indicate that $\underline{Y}_{n+1}(x=n+1)$ contains operators in section

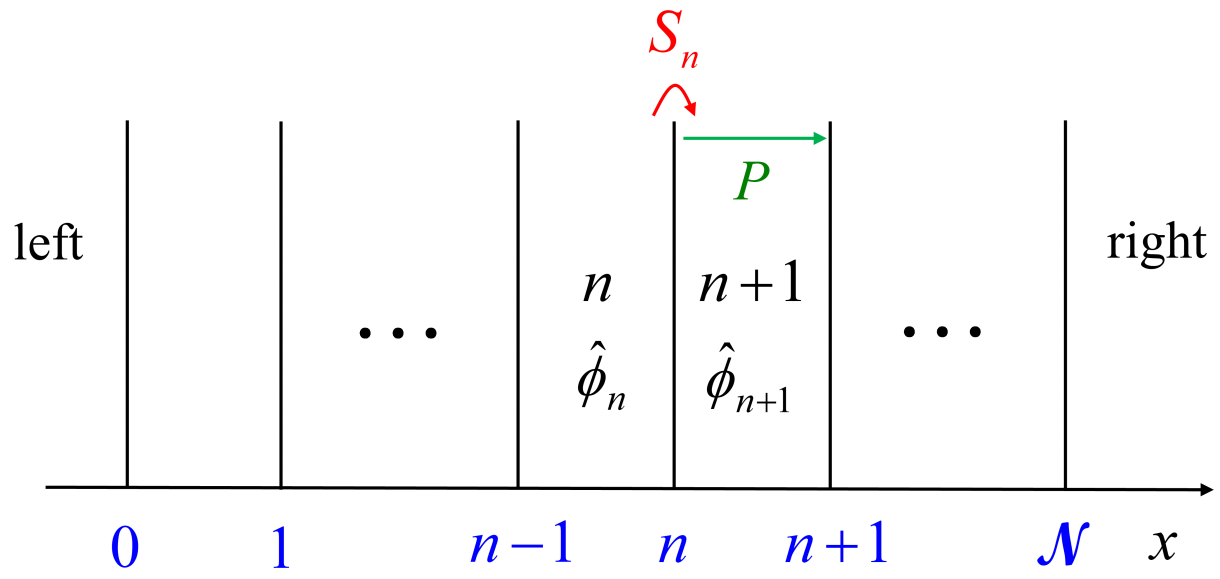

Figure 2.10: SQUID sites n (blue) and CPW sections n with flux field $\hat{\phi}_n(x,t)$ for $n-1<x<n$ (black). The matrix S_n in Eq. (2.89) (red) transfers the flux field across the boundary at site n. The matrix $P=P(1)$ in Eq. (2.94) (green) propagates the flux field through section $n+1$ from the right side of site n to the left side of site $n+1$. Repeated application of the transfer matrix $T_n=P(1)\,S_n$ in Eq. (2.97) thus propagates the flux field from the left side to the right side of the SQUID array.

$n+1$ evaluated at $x=n+1$ and $\underline{X}_n(x=n)$ contains operators in section n evaluated at $x=n$. The transfer matrix T_n in Eq. (2.97) thus transfers the latter to the right by one repeated unit of the periodic SQUID array (see Figure 2.10). Furthermore, we use the index n for T_n to indicate that the transfer matrix depends on the SQUID site n by the contribution $S=S_n$ in Eq. (2.89) (see text below Eq. (2.82)). Finally, for given frequency ω, both S_n and $P(1)$ in Eq. (2.97) depend on the set of frequencies ω_α in Eq. (2.77) by the inverse dispersion relation $K(\omega)$.

2.4 Dynamical Casimir radiation in the periodic SQUID array

We consider a linear, periodic array of $\mathcal{N}+1$ SQUIDs $n=0,\ldots,\mathcal{N}$ along the x-axis separated by a distance (lattice constant) ℓ and connected to coplanar waveguide (CPW) lines. In this section we use again unitless variables where the lattice constant is 1 and $x_n=n$. The first SQUID (on the far left) is located at $x=0$ and the last one (on the far right) at $x=\mathcal{N}$ (see Figure 2.10).

If the transfer matrix in Eq. (2.97) is independent of the SQUID site n, i.e., $T_n=T$, by repeated application of Eq. (2.96) we can express the operators on the far right in terms of the

operators on the far left:

$$\underline{X}_{\text{right}}(x=\mathscr{N}) = U\underline{X}_{\text{left}}(x=0) \tag{2.98}$$

with the $2M \times 2M$ matrix

$$U = ST^{\mathscr{N}} = S(PS)^{\mathscr{N}} \tag{2.99}$$

and $\underline{X}_{\text{left}}$ and $\underline{X}_{\text{right}}$ are defined as in Eq. (2.88) with vectors $\vec{X}_R$ and $\vec{X}_L$ as in Eq. (2.83). In Section 3.4 we will also consider an n-dependent harmonic drive $\delta\varepsilon_n(t) = \delta\varepsilon^0\cos(\Omega t + \varphi_n)$ with $\delta\varepsilon^0$ equal for all SQUIDs and $\varphi_n = n(2\pi)/3$ (see Eq. (2.58)). This case is also described by Eqs. (2.98), (2.99) using a modified U-matrix for a periodically repeated unit cell containing 3 SQUIDs in an array containing a total number of $3\mathscr{N}+1$ SQUIDs:

$$U' = S(\varphi=0)\left[T\left(\varphi=\frac{4\pi}{3}\right)T\left(\varphi=\frac{2\pi}{3}\right)T(\varphi=0)\right]^{\mathscr{N}}. \tag{2.100}$$

Using Eq. (2.88) and the notation

$$U = \begin{pmatrix} a & b \\ c & d \end{pmatrix} \tag{2.101}$$

with $M \times M$ matrices a, b, c, d, Eq. (2.98) can be written as

$$\begin{pmatrix} \vec{X}_R \\ \vec{X}_L \end{pmatrix}_{\text{right}} = \begin{pmatrix} a & b \\ c & d \end{pmatrix} \begin{pmatrix} \vec{X}_R \\ \vec{X}_L \end{pmatrix}_{\text{left}}. \tag{2.102}$$

This equation relates a signal on the right of the SQUID array (incoming and outgoing) to a signal on the left (compare Figure 2.9). However, we would like to study a different situation: For given *incoming* signals $\vec{X}_{R,\text{left}}$ and $\vec{X}_{L,\text{right}}$ (e.g., thermal noise) we would like to obtain the *outgoing* signals $\vec{X}_{R,\text{right}}$ and $\vec{X}_{L,\text{left}}$ generated or influenced by the dynamical DCE effect in the SQUID array.

This result can be obtained from Eq. (2.102) by simple algebra, and we find

$$\begin{pmatrix} \vec{X}_{R,\text{right}} \\ \vec{X}_{L,\text{left}} \end{pmatrix} = \begin{pmatrix} A & B \\ C & D \end{pmatrix} \begin{pmatrix} \vec{X}_{R,\text{left}} \\ \vec{X}_{L,\text{right}} \end{pmatrix} , \tag{2.103}$$

with $M \times M$ matrices

$$A = a - b\,d^{-1}c\,, \quad B = b\,d^{-1}\,, \quad C = -d^{-1}c\,, \quad D = d^{-1}\,, \tag{2.104}$$

where d^{-1} is the matrix inverse of d. The transformation from Eq. (2.102) to (2.103) is well-defined since the matrix in Eq. (2.102) is regular due to the fact that all frequencies ω_α contained in the $\vec{X}$-vectors are allowed by definition (see Eq. (2.75) and the related discussion).

Explicitly, Eq. (2.103) reads for given frequency $\omega_\alpha > 0$, using the definition (2.83),

$$\hat{a}^R_{\text{right}}(\omega_\alpha) = \sum_{\beta=1}^{M} A_{\alpha\beta}\, \vec{X}_{R,\text{left}}\Big|_\beta + \sum_{\beta=1}^{M} B_{\alpha\beta}\, \vec{X}_{L,\text{right}}\Big|_\beta \tag{2.105}$$

where $\vec{X}_{R,\text{left}}\Big|_\beta$ is the component β of the vector $\vec{X}_{R,\text{left}}$. Equation 2.105, gives the Bogoliubov transformations for our particular system (see Section 1.1). Multiplying this equation from the left by $\hat{a}^{R\dagger}_{\text{right}}(\omega_\alpha)$ we obtain the number operator for outgoing photons with frequency ω_α moving to the right (R) on the right side (right) of the SQUID array:

$$\begin{aligned} &\hat{n}^R_{\text{right}}(\omega_\alpha) \equiv \hat{a}^{R\dagger}_{\text{right}}(\omega_\alpha)\,\hat{a}^R_{\text{right}}(\omega_\alpha) \\ &= \sum_{\gamma,\beta} A^*_{\alpha\gamma} A_{\alpha\beta} \left(\vec{X}_{R,\text{left}}\Big|_\gamma\right)^\dagger \vec{X}_{R,\text{left}}\Big|_\beta + \sum_{\gamma,\beta} B^*_{\alpha\gamma} B_{\alpha\beta} \left(\vec{X}_{L,\text{right}}\Big|_\gamma\right)^\dagger \vec{X}_{L,\text{right}}\Big|_\beta \\ &\quad + \text{terms containing products } \hat{a}^\dagger_{\text{left}}\hat{a}_{\text{right}}\,,\ \hat{a}^\dagger_{\text{right}}\hat{a}_{\text{left}}\,. \end{aligned} \tag{2.106}$$

To find the DCE radiation associated with the photon number operator $\hat{n}^R_{\text{right}}(\omega_\alpha)$ we define the density operator for a thermal equilibrium ensemble at temperature T (statistical operator):

$$\hat{\rho}(T) = \frac{\exp\left[-\hat{H}/(k_B T)\right]}{\text{tr}\left\{\exp\left[-\hat{H}/(k_B T)\right]\right\}} \tag{2.107}$$

where k_B is the Boltzmann constant, tr denotes a trace, and the Hamilton operator in the basis of the incoming, non-interacting photon states on both sides of the array is given by

$$\hat{H} = \int_0^\infty \frac{d\omega}{2\pi}\, \hbar\omega \left[\hat{a}^{L\dagger}_{\text{right}}(\omega)\,\hat{a}^{L}_{\text{right}}(\omega) + \hat{a}^{R\dagger}_{\text{left}}(\omega)\,\hat{a}^{R}_{\text{left}}(\omega)\right] . \tag{2.108}$$

Using Eq. (2.106) and $\hat{\rho}(T)$ from Eq. (2.107) we find the expectation value of the photon number of the outgoing mode with frequency ω_α moving to the right (R) on the right side (right) of the SQUID array:

$$\begin{aligned} n^R_{\text{right}}(\omega_\alpha, T) &= \text{tr}\left\{\hat{\rho}(T)\,\hat{n}^R_{\text{right}}(\omega_\alpha)\right\} \\ &= \sum_{\gamma,\beta} A^*_{\alpha\gamma} A_{\alpha\beta}\, \text{tr}\left\{\hat{\rho}(T)\left(\vec{X}_{R,\text{left}}\Big|_\gamma\right)^\dagger \vec{X}_{R,\text{left}}\Big|_\beta\right\} \\ &+ \sum_{\gamma,\beta} B^*_{\alpha\gamma} B_{\alpha\beta}\, \text{tr}\left\{\hat{\rho}(T)\left(\vec{X}_{L,\text{right}}\Big|_\gamma\right)^\dagger \vec{X}_{L,\text{right}}\Big|_\beta\right\} . \end{aligned} \tag{2.109}$$

The traces on the r.h.s. of the above equation only contribute for $\gamma = \beta$ since the Hamilton operator $\hat{H}$ in Eq. (2.108) is diagonal in ω. Moreover, the terms containing products $\hat{a}^\dagger_{\text{left}}\hat{a}_{\text{right}}$ and $\hat{a}^\dagger_{\text{right}}\hat{a}_{\text{left}}$ in Eq. (2.106) vanish when taking the trace since the thermal noise on the left and right side of the array is uncorrelated. We thus find, using the form of the vector $\vec{X}$ in Eq. (2.83),

$$
\begin{aligned}
& n^{R}_{\text{right}}(\omega_\alpha, T) \\
& = \sum_{\beta=1}^{\kappa-1} \left|A_{\alpha\beta}\right|^2 \, \text{tr}\left\{\hat{\rho}(T)\, \hat{a}^{R\dagger}_{\text{left}}(\omega_\beta)\, \hat{a}^{R}_{\text{left}}(\omega_\beta)\right\} + \sum_{\beta=\kappa}^{M} \left|A_{\alpha\beta}\right|^2 \, \text{tr}\left\{\hat{\rho}(T)\, \hat{a}^{R}_{\text{left}}(|\omega_\beta|)\, \hat{a}^{R\dagger}_{\text{left}}(|\omega_\beta|)\right\} \\
& + \sum_{\beta=1}^{\kappa-1} \left|B_{\alpha\beta}\right|^2 \, \text{tr}\left\{\hat{\rho}(T)\, \hat{a}^{L\dagger}_{\text{right}}(\omega_\beta)\, \hat{a}^{L}_{\text{right}}(\omega_\beta)\right\} + \sum_{\beta=\kappa}^{M} \left|B_{\alpha\beta}\right|^2 \, \text{tr}\left\{\hat{\rho}(T)\, \hat{a}^{L}_{\text{right}}(|\omega_\beta|)\, \hat{a}^{L\dagger}_{\text{right}}(|\omega_\beta|)\right\} \, .
\end{aligned}
\tag{2.110}
$$

The traces in the first and third terms on the r.h.s. of the above equation are the occupation numbers of the incoming photons with frequencies $\omega_\beta > 0$ on both sides of the array at thermal equilibrium (thermal noise):

$$
\begin{aligned}
n(\omega_\beta, T)\big|_{\text{eq}} &= \text{tr}\left\{\hat{\rho}(T)\, \hat{a}^{R\dagger}_{\text{left}}(\omega_\beta)\, \hat{a}^{R}_{\text{left}}(\omega_\beta)\right\} \\
&= \text{tr}\left\{\hat{\rho}(T)\, \hat{a}^{L\dagger}_{\text{right}}(\omega_\beta)\, \hat{a}^{L}_{\text{right}}(\omega_\beta)\right\} \\
&= \frac{1}{\exp\left[\hbar\omega_\beta/(k_B T)\right] - 1} \, .
\end{aligned}
\tag{2.111}
$$

The traces in the second and fourth terms on the r.h.s. in Eq. (2.110) can also be expressed in terms of $n(\omega_\beta, T)\big|_{\text{eq}}$ after using the commutation relation for a given frequency $\omega > 0$:

$$
\left[\hat{a}(\omega), \hat{a}^\dagger(\omega)\right] = 1 \;\Rightarrow\; \hat{a}(\omega)\, \hat{a}^\dagger(\omega) = \hat{a}^\dagger(\omega)\, \hat{a}(\omega) + 1 \, . \tag{2.112}
$$

For example, for the second term on the r.h.s. in Eq. (2.110) this gives

$$
\begin{aligned}
& \text{tr}\left\{\hat{\rho}(T)\, \hat{a}^{R}_{\text{left}}(|\omega_\beta|)\, \hat{a}^{R\dagger}_{\text{left}}(|\omega_\beta|)\right\} \\
&= \text{tr}\left\{\hat{\rho}(T)\, \hat{a}^{R\dagger}_{\text{left}}(|\omega_\beta|)\, \hat{a}^{R}_{\text{left}}(|\omega_\beta|)\right\} + \text{tr}\left\{\hat{\rho}(T)\right\} \\
&= n(|\omega_\beta|, T)\big|_{\text{eq}} + 1 \, .
\end{aligned}
\tag{2.113}
$$

It is this operation, the application of the commutation relation for negative frequencies $\omega_\beta < 0$ for $\beta \geq \kappa$ as in Eq. (2.113), that results in the DCE radiation by the extra 1 on the r.h.s. of Eq. (2.113) (see Eq. (2.78) and related discussion, and Figure 2.8 on page 38). Using Eq. (2.113) in Eq. (2.110) we obtain the final result for the expectation value of the photon number of the outgoing mode with frequency ω_α moving to the right (R) on the right side (right) of the SQUID array:

$$\begin{aligned} n^R_{\text{right}}(\omega_\alpha, T) = & \underbrace{\sum_{\beta=1}^{M} \left|A_{\alpha\beta}\right|^2 \, n(|\omega_\beta|, T)\big|_{\text{eq}}}_{\text{thermal noise from left side}} + \underbrace{\sum_{\beta=\kappa}^{M} \left|A_{\alpha\beta}\right|^2}_{\text{DCE radiation}} \\ & + \underbrace{\sum_{\beta=1}^{M} \left|B_{\alpha\beta}\right|^2 \, n(|\omega_\beta|, T)\big|_{\text{eq}}}_{\text{thermal noise from right side}} + \underbrace{\sum_{\beta=\kappa}^{M} \left|B_{\alpha\beta}\right|^2}_{\text{DCE radiation}}, \end{aligned} \tag{2.114}$$

with the matrices A, B given by Eq. (2.104) and $n(|\omega_\beta|, T)\big|_{\text{eq}}$ by Eq. (2.111). In the same way we obtain the expectation value of the photon number of the outgoing mode with frequency ω_α moving to the left (L) on the left side (left) of the SQUID array:

$$\begin{aligned} n^L_{\text{left}}(\omega_\alpha, T) = & \underbrace{\sum_{\beta=1}^{M} \left|C_{\alpha\beta}\right|^2 \, n(|\omega_\beta|, T)\big|_{\text{eq}}}_{\text{thermal noise from left side}} + \underbrace{\sum_{\beta=\kappa}^{M} \left|C_{\alpha\beta}\right|^2}_{\text{DCE radiation}} \\ & + \underbrace{\sum_{\beta=1}^{M} \left|D_{\alpha\beta}\right|^2 \, n(|\omega_\beta|, T)\big|_{\text{eq}}}_{\text{thermal noise from right side}} + \underbrace{\sum_{\beta=\kappa}^{M} \left|D_{\alpha\beta}\right|^2}_{\text{DCE radiation}} \end{aligned} \tag{2.115}$$

with the matrices C, D given by Eq. (2.104).

2.5 Summary of computational procedure

In this section we summarize the procedure of calculating the photon number $n^R_{\text{right}}(\omega_\alpha, T)$ and $n^R_{\text{left}}(\omega_\alpha, T)$ in Eqs. (2.114), (2.115) for given system parameters. We use again unitless variables by expressing lengths in units of ℓ and times in units of ℓ/v where ℓ is the distance between SQUIDs in the periodic array and v is the speed of light in the CPW (see text after Eq. (2.16)). The calculation

of the band structure $\omega_\nu(k)$ and Bloch functions $\psi_{\nu,k}(x) = e^{ikx}u_{\nu,k}(x)$ for the Kronig-Penney type model discussed in Section 2.2.3 is illustrated in the Mathematica notebook in the Appendix. Results in Chapter III were generated using the full-length calculation with a Python program available in the author's public GitHub Repository [4]. Using unitless variables, the only system-specific input parameters are:

- A given (unitless) frequency $\omega = \omega_\alpha > 0$ for which we want to calculate $n^R_{\text{right}}(\omega_\alpha, T)$ and $n^R_{\text{left}}(\omega_\alpha, T)$;
- The energy parameter ε in Eqs. (2.19) and (2.33);
- The drive frequency Ω, amplitudes $\delta\varepsilon_n^0$ and phases φ_n in the harmonic drive term $\delta\varepsilon_n(t) = \delta\varepsilon_n^0 \cos(\Omega t + \varphi_n)$ in Eq. (2.33);
- The number of repeated units $\mathscr{N}$ of the SQUID array;
- The temperature T in the thermal occupation numbers $n(\omega_\beta, T)\big|_{\text{eq}}$ in Eq. (2.111).

The calculation of $n^R_{\text{right}}(\omega_\alpha, T)$ and $n^R_{\text{left}}(\omega_\alpha, T)$ proceeds as follows.

1. Using unitless variables, the band structure for the static case only depends on the parameter ε (see Section 2.2.3). Program the inverse dispersion relation $k(\omega, \varepsilon) \in [0, \pi]$ in Eq. (2.32). If ω is allowed, the function should return the value $k(\omega)$. If ω is not allowed (i.e., falls in a frequency gap) the function should return a flag. Extend this function to negative frequencies by defining $k(\omega) := k(|\omega|)$ for $\omega < 0$. The function $k(\omega, \varepsilon) > 0$ corresponds to $K(\omega)$ defined in Eq. (2.64).

2. Program a function $u(x, \omega, \varepsilon)$ corresponding to $u_\omega(x) = u_{\nu,k(\omega)}(x)$ in Eq. (2.28). A closed-form expression of $u(x, \omega, \varepsilon)$ is given in the Mathematica notebook in the Appendix. where the function is called "u1" for $k > 0$ (right-moving mode) and "u2" for $k < 0$ (left-moving mode). In the notebook, ω is denoted q (see footnote 1 on page 14) and the function $u_\omega(x)$ depends explicitly on $q = \omega$ and the function $k(\omega, \varepsilon)$ of step 1.

3. For the given frequency ω and drive frequency Ω identity the largest simply connected frequency domain that includes ω according to Eq. (2.77) using the function $k(\omega,\varepsilon)$ of step 1. This results in numbers N_u, N_l, M and a vector ω_α with $\alpha = 1,\ldots,M$ as in Eq. (2.75), where $\omega = \omega_\alpha$ with $\alpha = N_u + 1$. (Some of these frequencies ω_α may be negative.)

4. Identify the index κ according to Eq. (2.78). If all $\omega_\alpha > 0$ and no such κ exists, then there is no DCE radiation with frequency ω.

5. For the positive frequencies $\omega_\alpha > 0$ with $\alpha = 1,\ldots,\kappa-1$ found in step 3 calculate the numbers $\mathscr{C}_\alpha = \mathscr{C}[\omega(\alpha)]$ and $\mathscr{A}_\alpha = \mathscr{A}[\omega(\alpha)]$ using Eqs. (2.68) and (2.67). For the negative frequencies $\omega_\alpha < 0$ with $\alpha = \kappa,\ldots,M$, calculate $\mathscr{C}_\alpha = \mathscr{C}(|\omega(\alpha)|)$ and $\mathscr{A}_\alpha = \mathscr{A}(|\omega(\alpha)|)^*$ using Eq. (2.69). This results in vectors $\mathscr{C}_\alpha$ and $\mathscr{A}_\alpha$ with $\alpha = 1,\ldots,M$.

6. For the frequencies ω_α found in step 3 calculate the numbers $d\omega(\alpha) = \left|\dfrac{dk}{d\omega_\alpha}\right|^{1/2}$ defined in Eq. (2.79), using the function $k(\omega,\varepsilon)$ of step 1. This results in a vector $d\omega(\alpha)$ with $\alpha = 1,\ldots,M$.

7. For given SQUID site n, calculate the matrices $G^{(n)}_{\alpha\beta}$ and $A_{\alpha\beta}$ in Eqs. (2.81) and (2.82) using the vectors found above.

8. For given SQUID site n calculate the matrix S using Eqs. (2.89) and (2.90).

9. Calculate the matrix $P(1)$ in Eqs. (2.93) and (2.94) using the function $k(\omega,\varepsilon)$ of step 1 and κ found in step 4. (Note that $K(\omega)$ in Eq. (2.93) is positive by definition.)

10. If the matrix S (and thus T) is independent of the SQUID site n, calculate the matrix U using Eq. (2.99) with the matrices S and P found above and the number $\mathscr{N}$ of repeated units of the array. Otherwise, modify the calculation of U according to the given setup (See Chapter III).

11. Identify the submatrices a, b, c, d of U according to Eq. (2.101), and use them to calculate the matrices A, B, C, D in Eq. (2.104).

12. Use the matrices A, B, C, D to calculate $n^R_{\text{right}}(\omega_\alpha, T)$ and $n^R_{\text{left}}(\omega_\alpha, T)$ in Eqs. (2.114), (2.115).

2.6 Special case: Single SQUID

As a test case, we also consider a single SQUID in a CPW, corresponding to $\mathscr{N} = 1$. In this section we summarize the required modifications to calculate the photon number $n^R_{\text{right}}(\omega_\alpha, T)$ and $n^R_{\text{left}}(\omega_\alpha, T)$ in Eqs. (2.114), (2.115) on both sides of the SQUID.

- The Bloch modes $\psi_k(x)$ in Eq. (2.35) should be replaced by plane waves e^{ikx}, which amounts to setting $u_k(x) = 1$ in Eq. (2.36). The dispersion relation is simply $\omega(k) = v|k|$ corresponding to $\omega(k) = |k|$ in unitless variables. Assuming that the SQUID is at $x = 0$ Eq. (2.35) reduces to

$$\begin{aligned}\hat{\Phi}_\pm(x,t) = &\sqrt{\frac{\hbar}{2C_0}} \int_{-\infty}^{\infty} \frac{dk}{2\pi} \frac{1}{\sqrt{\omega(k)}} \\ &\times \left(\hat{a}_\pm(k) \exp\left[ikx - i\omega(k)t\right] + \hat{a}^\dagger_\pm(k) \exp\left[-ikx + i\omega(k)t\right] \right) ,\end{aligned} \tag{2.116}$$

  for $x > 0$ $(+)$ and $x < 0$ $(-)$.

- Instead of Eq. (2.42), annihilation operators in frequency space are defined by

$$\hat{a}^R_\pm(\omega) := \hat{a}_\pm\left[k(\omega)\right] , \quad \text{moving to the right (R)} , \tag{2.117a}$$

$$\hat{a}^L_\pm(\omega) := \hat{a}_\pm\left[-k(\omega)\right] , \quad \text{moving to the left (L)} , \tag{2.117b}$$

  where $k(\omega) > 0$ as before, i.e., $k(\omega) = |\omega|$ (compare footnote 6 on page 26).

- Equation (2.51) is replaced by

$$\hat{\phi}_\pm(x,t) = \int_{-\infty}^{\infty} \frac{d\omega}{2\pi} \frac{1}{\sqrt{|\omega|}} \times \left[\hat{a}^R_\pm(\omega) e^{i\omega x} + \hat{a}^L_\pm(\omega) e^{-i\omega x} \right] e^{-i\omega t} , \tag{2.118}$$

  where for $\omega < 0$ we define $\hat{a}^R_\pm(\omega) = \hat{a}^{R\dagger}_\pm(|\omega|)$ and $\hat{a}^L_\pm(\omega) = \hat{a}^{L\dagger}_\pm(|\omega|)$. Note that for $\omega < 0$

Eq. (2.118) incorporates the correct signs in the plane-wave terms since $e^{-ik(\omega)x} = e^{i\omega x}$ for $\omega < 0$ with $k(\omega) = |\omega|$ (compare Eqs. (2.48) and (2.49)).

- Since for a single SQUID there are no frequency gaps, the numbers N_u and N_l in Eq. (2.77) are equal to the global cutoff, i.e., $N_u = N_l = N_{cut}$ and $M = 2N_{cut} + 1$. Identify the index κ according to Eq. (2.78) as before.

- Since $u(x) = 1$ in Eqs. (2.67) - (2.69) we obtain $\mathscr{C}_\omega = 1$ and $\mathscr{A}_\omega = i\omega$ for all ω (incorporating the correct sign in $\mathscr{A}_\omega$ for $\omega < 0$ since $(i|\omega|)^* = i\omega$ for $\omega < 0$).

- Since $\omega(k) = |k|$ we obtain $d\omega(\alpha) = \left|\dfrac{dk}{d\omega_\alpha}\right|^{1/2} = 1$ for all $\omega_\alpha > 0$.

- According to the above, the matrices $\delta G^{(n)}_{\alpha\beta}$ and $A_{\alpha\beta}$ in Eqs. (2.81) and (2.82) are replaced by

$$G_{\alpha\beta} = \delta_{\alpha\beta} + \frac{1}{2}\frac{\delta\varepsilon_n^0}{\varepsilon}\sqrt{\frac{|\omega_\alpha|}{|\omega_\beta|}}\left(\delta_{\beta,\alpha+1} + \delta_{\beta,\alpha-1}\right) , \tag{2.119}$$

$$A_{\alpha\beta} = \frac{i\omega_\alpha}{\varepsilon}\,\delta_{\alpha\beta} . \tag{2.120}$$

Thus, the matrix $\mathscr{G}$ in Eq. (2.90) is replaced by

$$\mathscr{G}_{\alpha\beta} = -i\frac{\varepsilon}{2\omega_\alpha}G_{\alpha\beta} . \tag{2.121}$$

The term $\delta_{\alpha\beta}$ in Eq. (2.119) (first term on the r.h.s.) incorporates the contribution from the term proportional to ε in the boundary condition (2.57) when applied to plane waves e^{ikx} at a single SQUID in the absence of a periodic lattice [12].

- Calculate the matrix S using Eqs. (2.89) and (2.90) as before, now using Eqs. (2.119) and (2.120). The matrix $P(1)$ in Eqs. (2.93) and (2.94) is not needed. Identify $U \equiv S$ and proceed as in steps 11 and 12 in Section 2.5.

[12] Note that for a periodic lattice, the contributions proportional to ε in the boundary condition at the SQUID sites n are incorporated in the Bloch functions in Eq. (2.28), which can travel freely through the lattice in the static case; see Section 2.2.3.

CHAPTER III

RESULTS AND DISCUSSION

Below, we present the results of our analysis. We concentrate on output radiation (photon-flux density), as a function of frequency. Unless specified, the input parameters for the calculations are (unitless) drive frequency $\Omega = 12$, lattice parameter $\varepsilon = 5$, modulation amplitude $\delta\varepsilon = \varepsilon/4$. All of the plots in our results were produced using the Python program found in the author's public GitHub repository [4].

3.1 One driven SQUID embedded in coplanar waveguide (CPW)

Below, in Fig. 3.2, we show the output radiation emitted by a single SQUID embedded in a CPW. This is in contrast to previous work [14], from which we borrow input parameters. We obtain a similar result, producing the distinctive one-mirror parabolic DCE shape described in [19]. One important distinction from the work cited is that the SQUID is embedded in a CPW, as opposed to terminating the CPW with a SQUID (effectively making the mirror semi-transparent as opposed to perfectly reflecting), radiation travels away from the mirror on both sides. A slightly higher overall photon-flux density is produced.

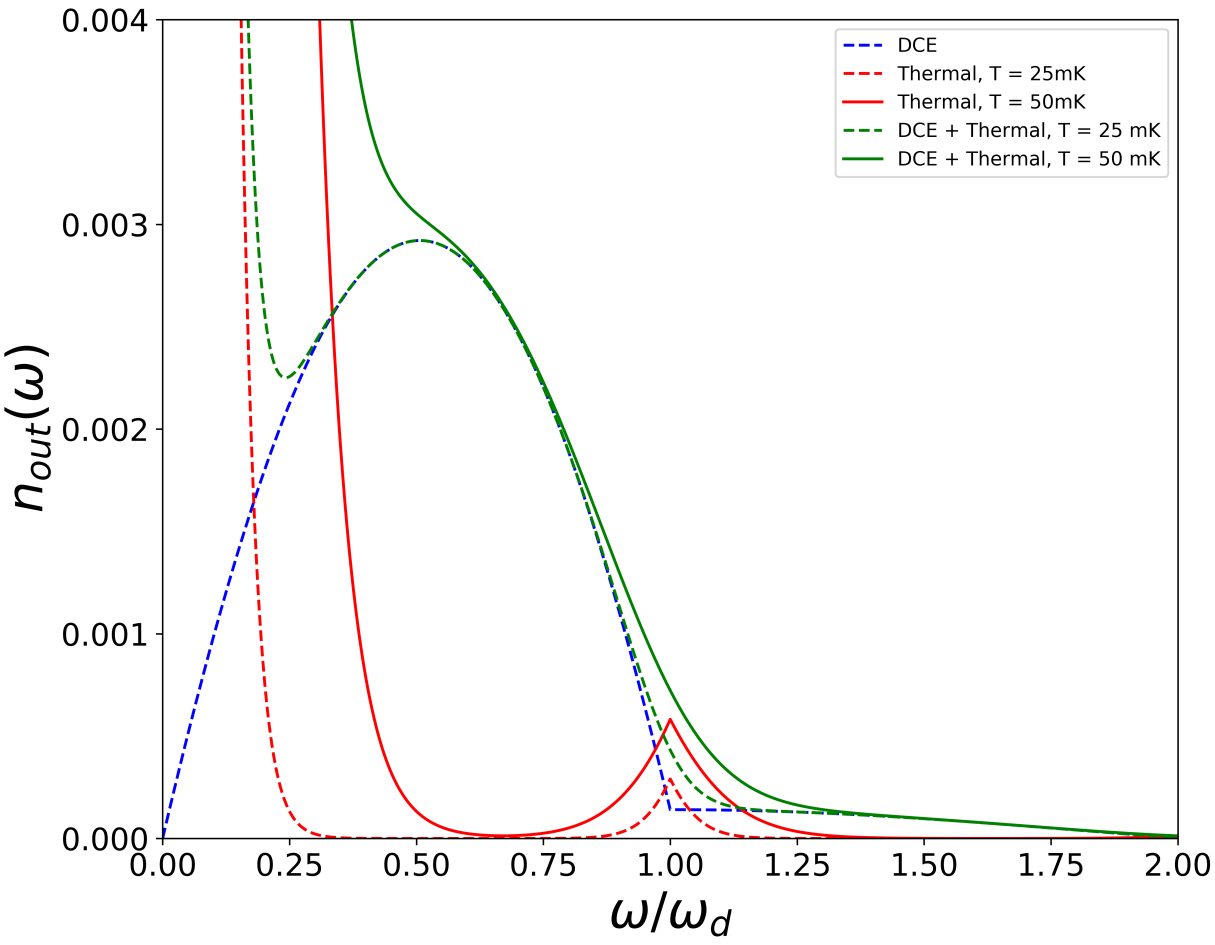

Figure 3.1: Reproduced results from [15], for radiation generated by a single SQUID. Here, the field only propagates on one side of the SQUID. Horizontal axis is normalized with drive frequency ω_d. Drive frequency $\omega_d/2\pi$=18.6 GHz.

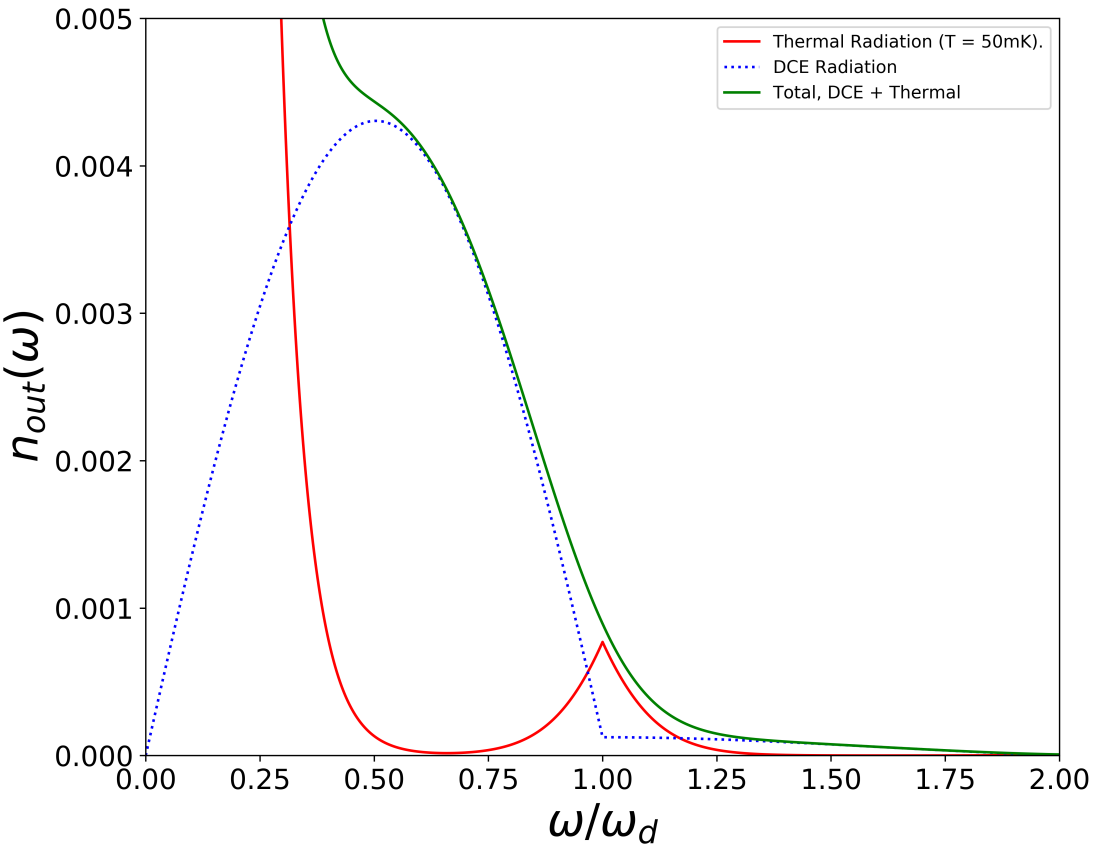

Figure 3.2: Output radiation for one single semi-transparent SQUID. We allow both sides of the SQUID to have incoming/outgoing radiation. Horizontal axis is normalized with drive frequency ω_d. Drive frequency $\omega_d/2\pi$=18.6 GHz. Left/right output radiation is symmetric.

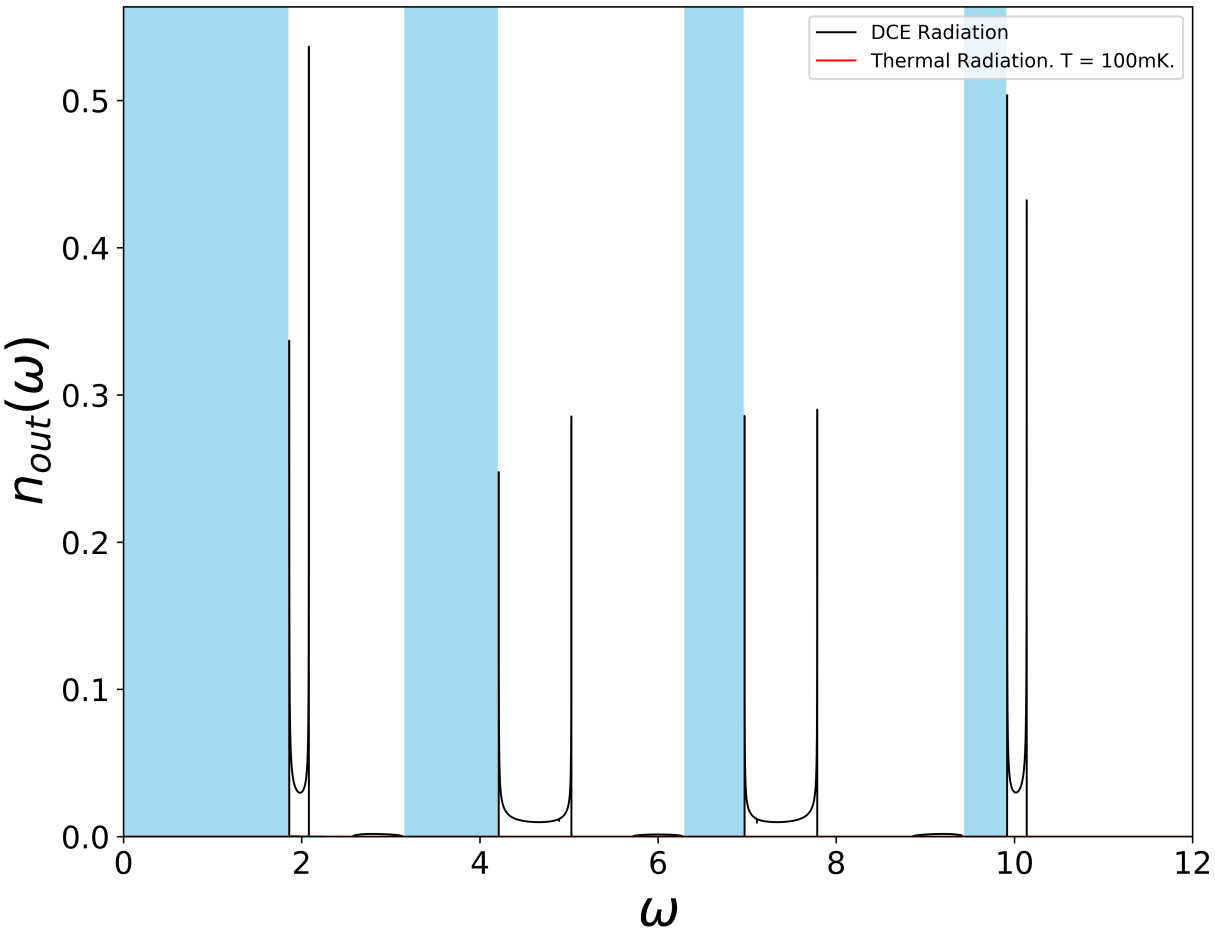

Figure 3.3: Output radiation for one single driven SQUID embedded in lattice with 50 static SQUIDs to either side. Input parameters used: $\Omega = 12$, $\varepsilon = 5$.

3.2 One SQUID embedded in lattice

We now discuss results of our own model for a periodic SQUID lattice. Forbidden regions (see Section 2.2.3) are shown in light blue. For these regions, no radiation (DCE or thermal) travels outside of the lattice. Detectable radiation is produced only within allowed regions.

For the following figures (3.3-3.5), only one SQUID is drive at a frequency $\Omega = 12$, in a periodic lattice with different lattice parameters ε. Different radiation patters emerge by changing the drive frequency and lattice parameter. Figure 3.3, shows the radiation produced by one single driven SQUID in a lattice $\varepsilon = 5$ which corresponds to physical lattice separation of about 2.21mm.

The radiation pattern changes dramatically compared to the one for a single SQUID between CPWs, when no lattice is present (see Fig. 3.2). The dramatic difference can be attributed to the presence of allowed and forbidden regions, as well as the change in the boundary condition due to the properties of Bloch functions, and the shape of the ground states of the field excited by the perturbation of such boundary conditions. A single SQUID surrounded by CPW would excite plane wave modes of the field, while when place in a lattice, the Bloch modes are excited instead.

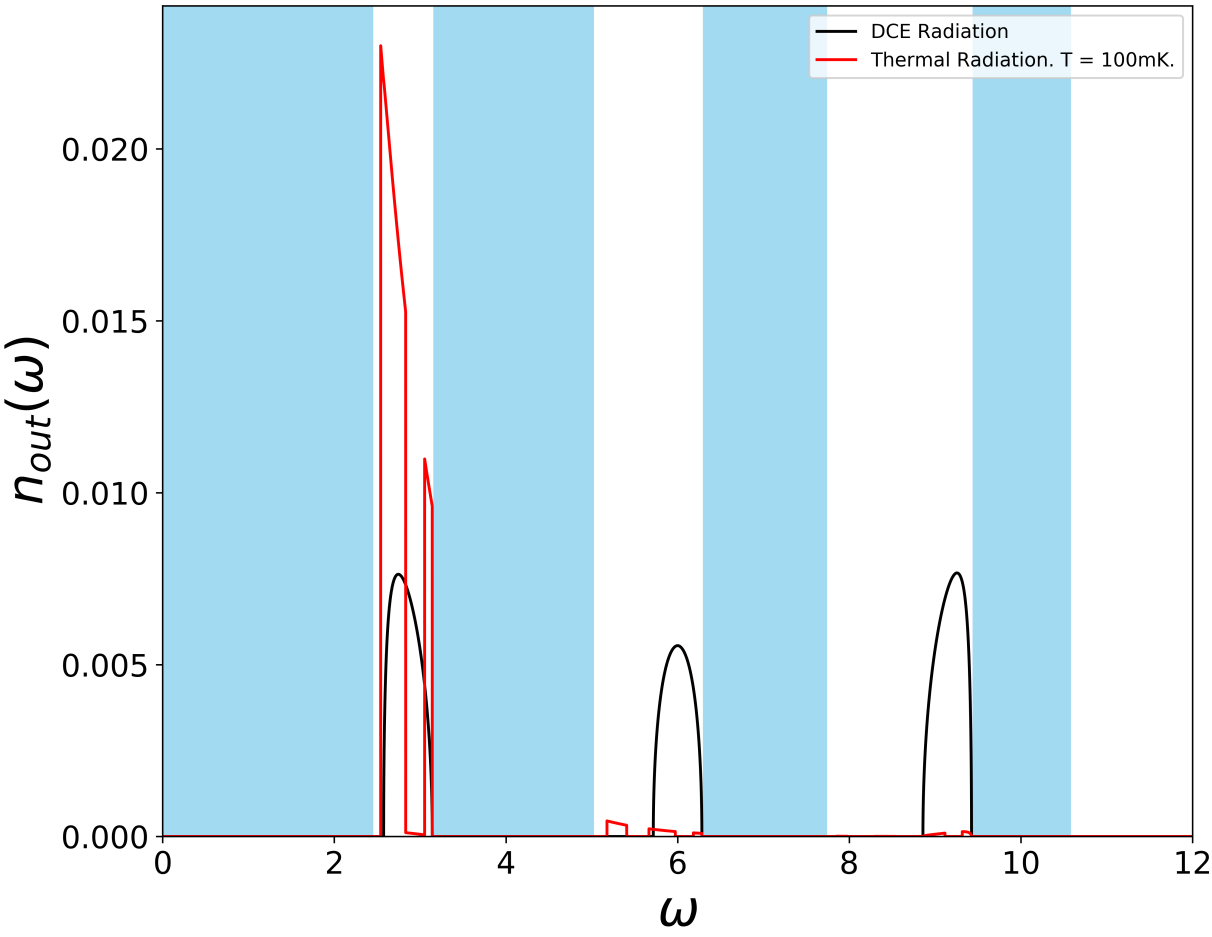

Figure 3.4: Output radiation for one single driven SQUID embedded in lattice. Input parameters used: $\Omega = 12$, $\varepsilon = 14$. A different band structure shows thermal contributions to the radiation. Temperature = 100mK.

Note that the presence of forbidden regions, particularly the region before the first allowed band, make it so the thermal radiation is filtered out. Since the input thermal radiation follows an inverse exponential relation for low frequencies (see Fig. 3.2), the first forbidden region absorbs most of the thermal radiation. By changing the structure of the lattice to $\varepsilon = 14$, the presence of thermal radiation can be observed, as well as well as different features in the DCE radiation (see Figure 3.4).

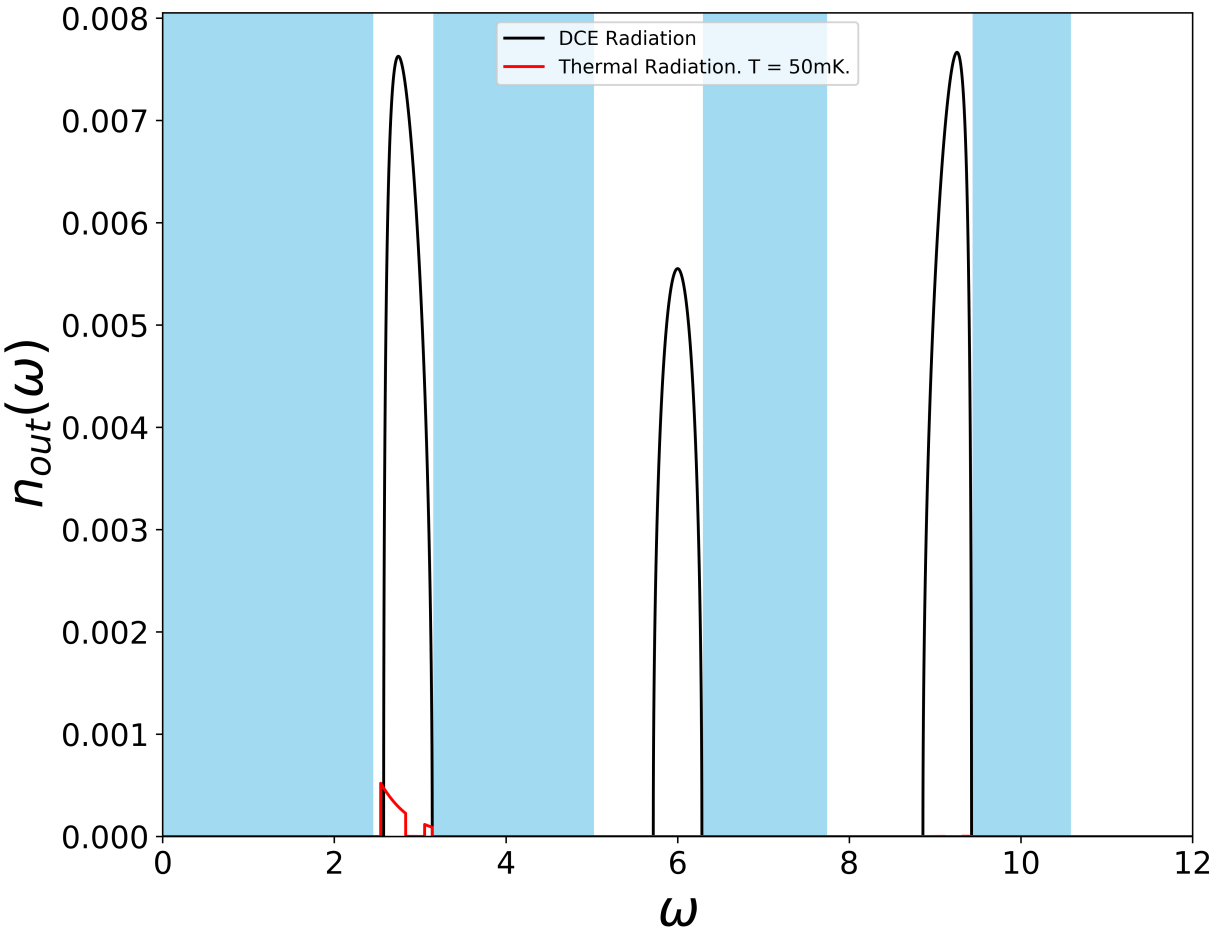

Figure 3.5: Output radiation for one single driven SQUID embedded in lattice. Input parameters used: $\Omega = 12$, $\varepsilon = 14$. A different band structure shows thermal contributions to the radiation. Temperature = 50mK.

Figure 3.5, shows how the distinct features of DCE radiation change when a different band structure is used (which is equivalent to changing the lattice parameter ε) (see Fig. 3.3). Here, the radiation is closer to the familiar single-SQUID parabolic shape. Note how the features of DCE radiation are not localized in one allowed region but instead cover multiple regions.

3.3 All SQUIDs embedded in lattice

The plots in this section correspond to the results of the case where all of the SQUIDs in a lattice with parameter ε are driven simultaneously (site-dependent phase $\varphi_n = 0$) with frequency Ω. We show the radiation spectrum for lattices of different sizes, with the size given by the number of SQUIDs in the lattice.

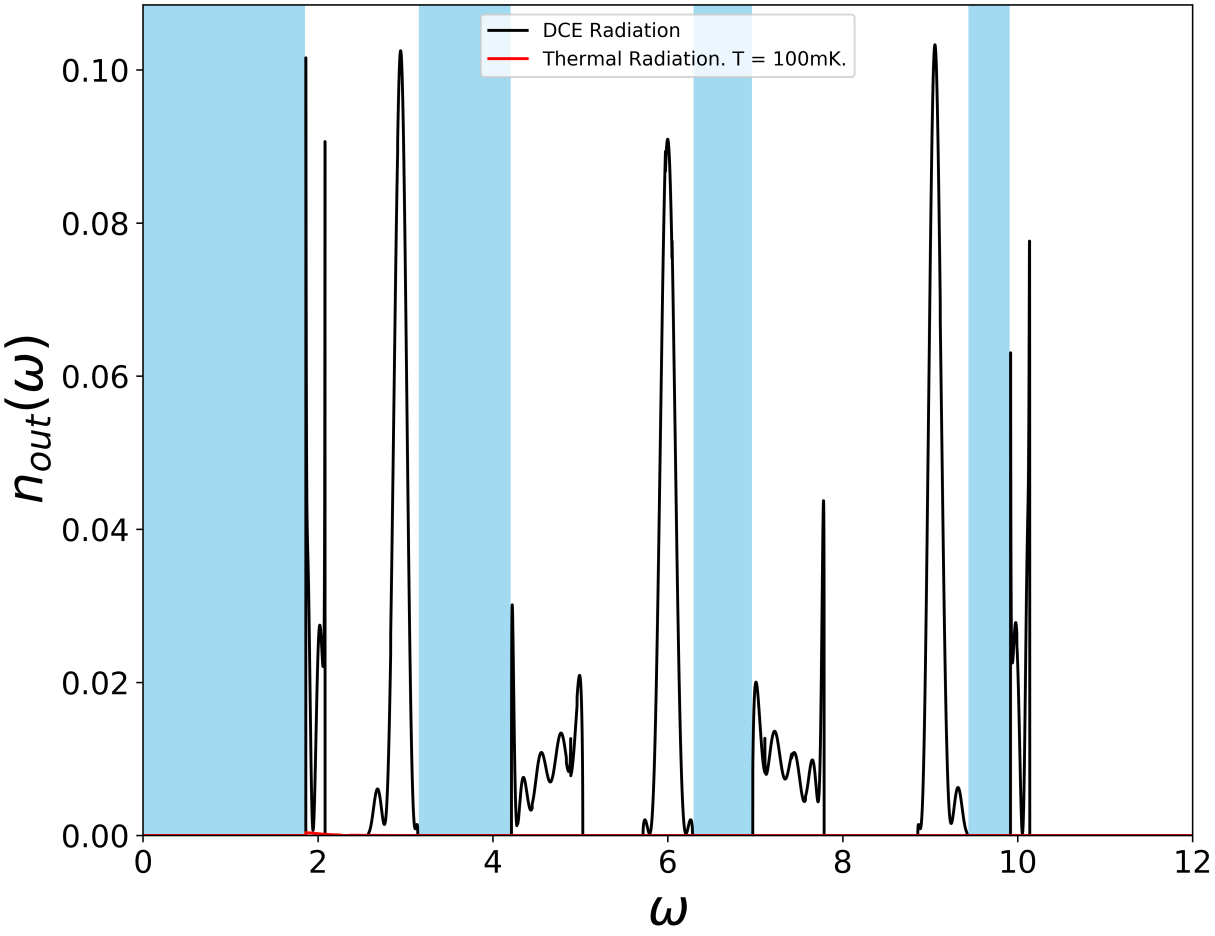

Figure 3.6: Output radiation for lattice of 10 driven SQUIDs. Input parameters used: $\Omega = 12$, $\varepsilon = 5$. Complex radiation patterns arise when all SQUIDs are active.

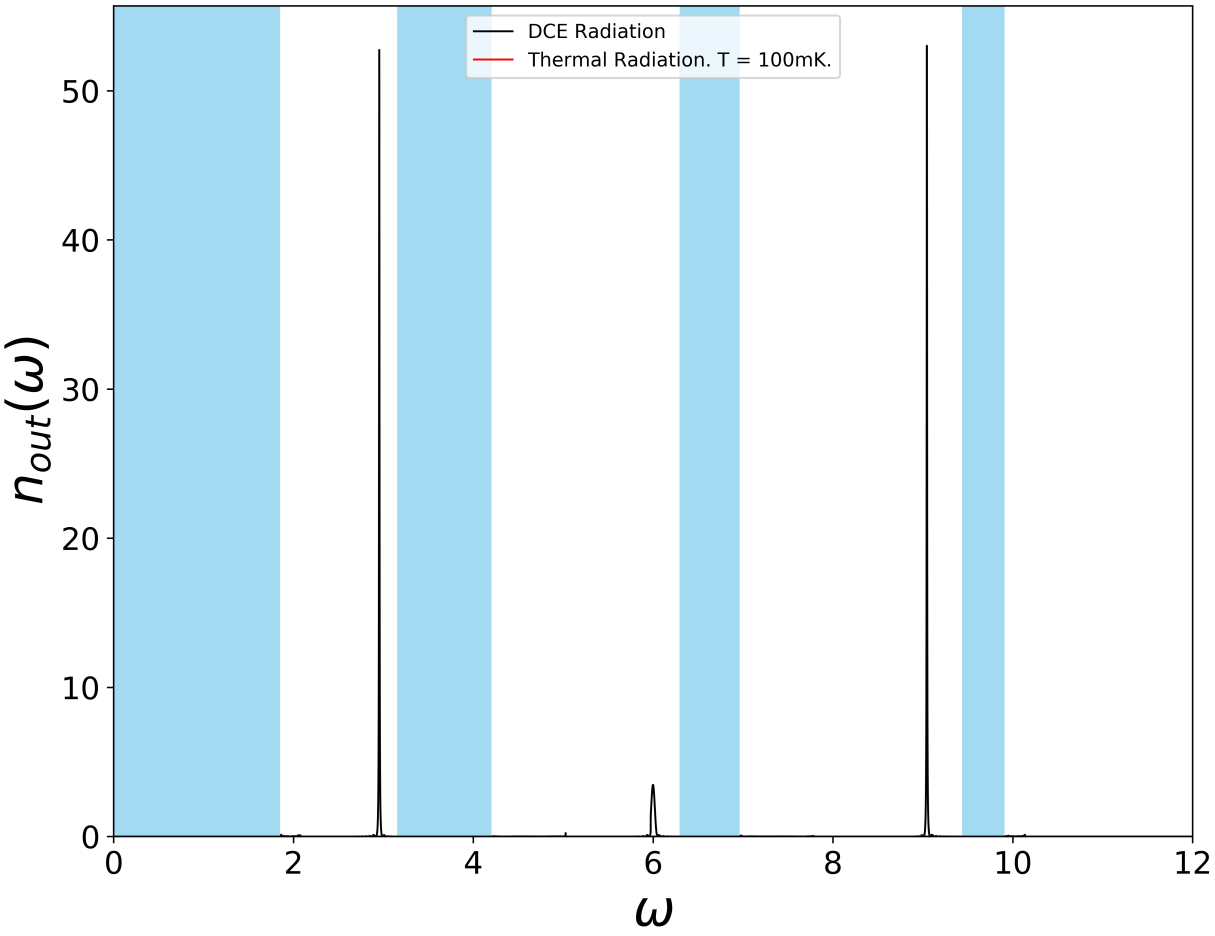

Figure 3.7: Output radiation for lattice of 50 driven SQUIDs. As we increase the number of SQUIDs, photon-flux density increases at narrow frequency ranges.

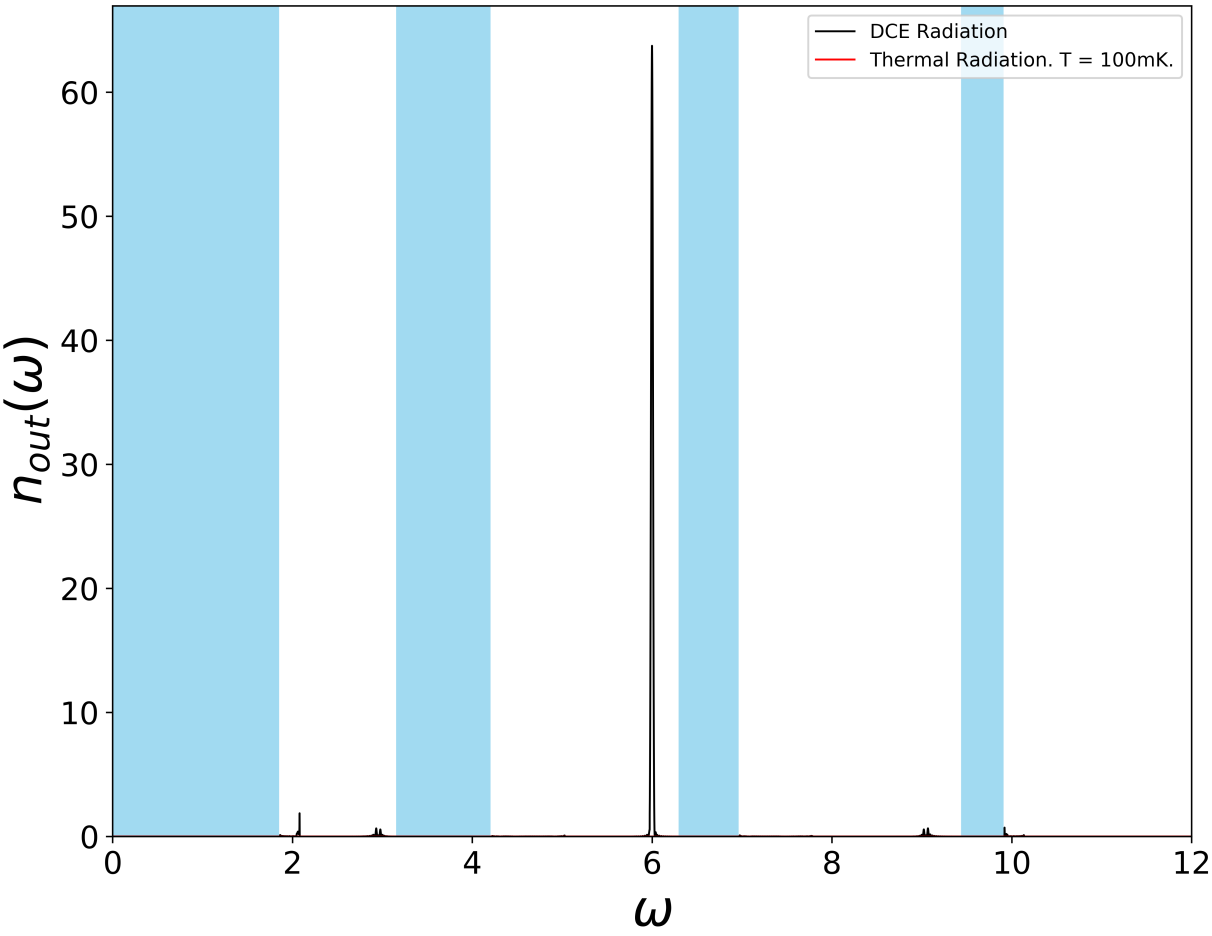

Figure 3.8: Output radiation for lattice of 100 driven SQUIDs. The frequency where most radiation is produced changes as we change number of SQUIDs.

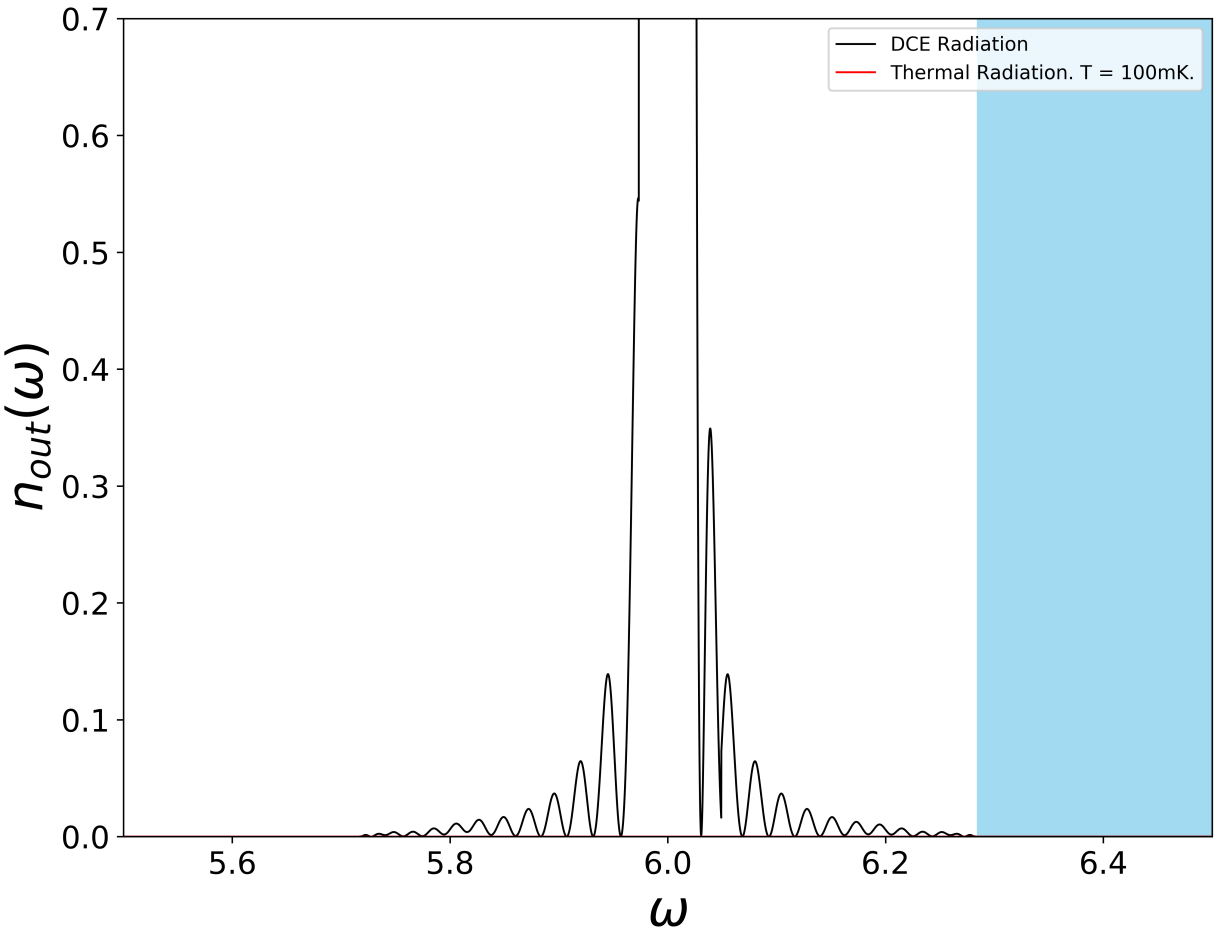

Figure 3.9: Output radiation for lattice of 100 driven SQUIDs. Here, we show the details of the radiation around half the oscillation frequency.

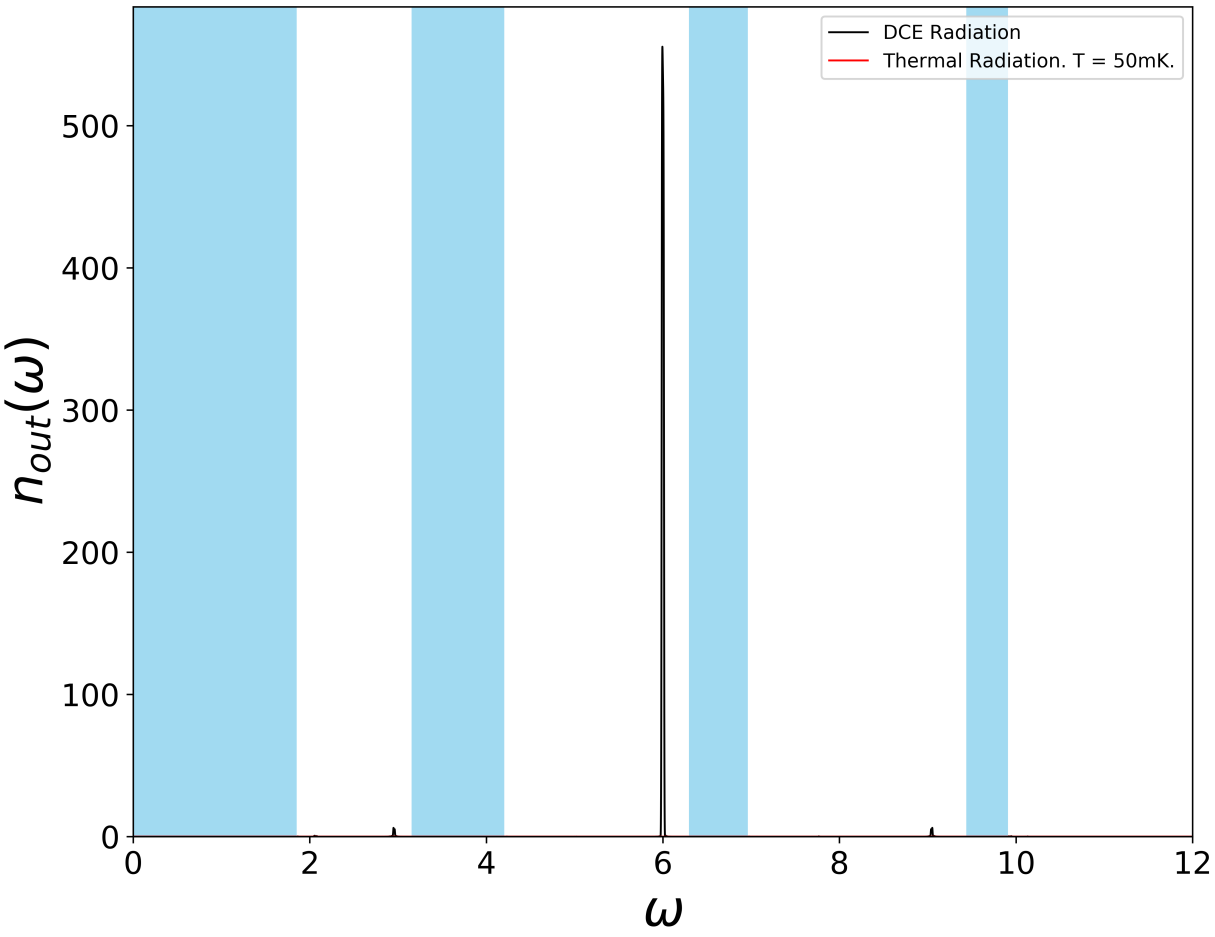

Figure 3.10: Output radiation for lattice of 150 driven SQUIDs. The magnitude of the photon-flux density changes in a non-trivial matter as we increase number of SQUIDs.

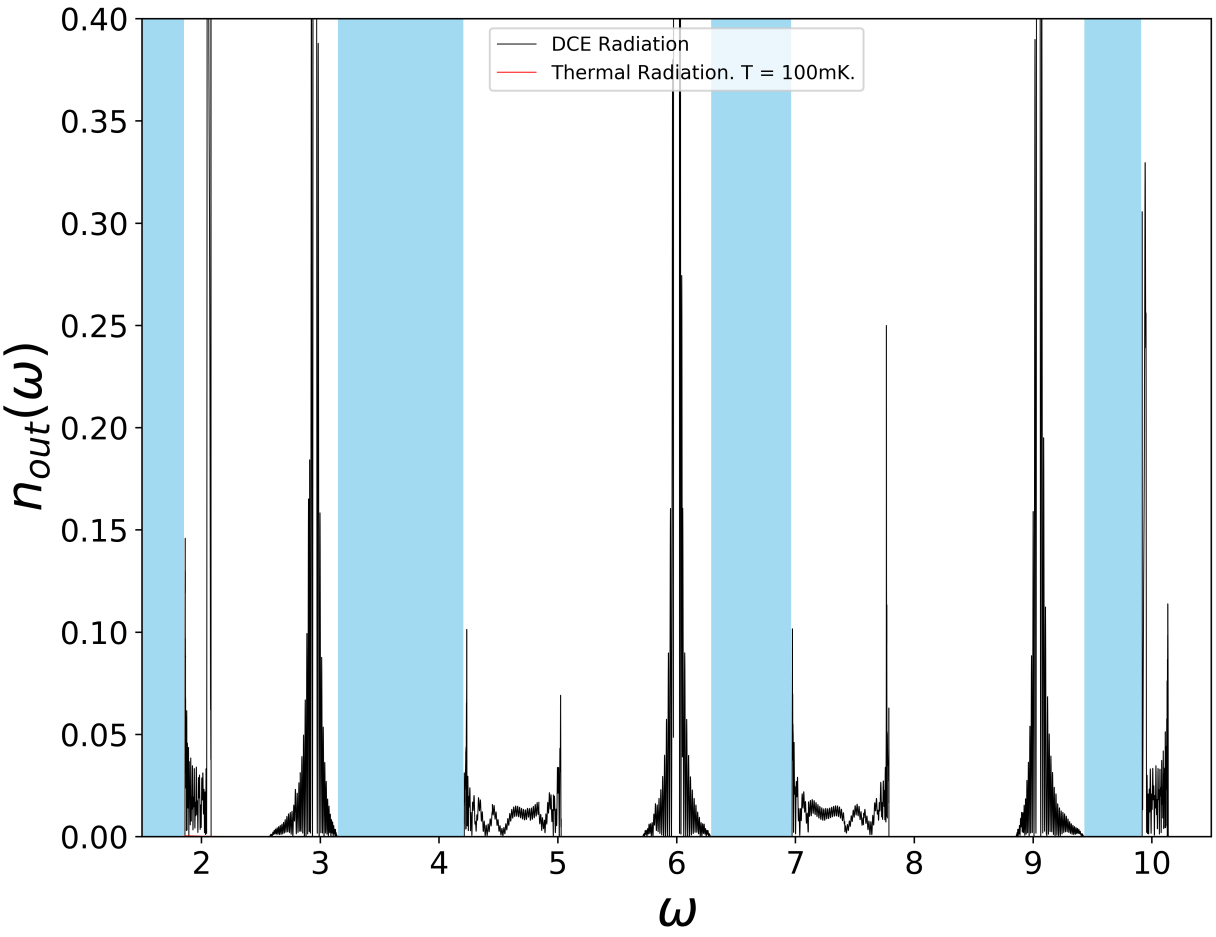

Figure 3.11: Output radiation for lattice of 150 driven SQUIDs. We show the detail in the behavior of photon production.

3.4 Spatial symmetry breaking

For all of the previous results, the lattice had spatial symmetry, i.e., there was nothing distinguishing the left and right side. Thus, the radiation emitted from each side was equal. We now turn our attention to a lattice of driven SQUIDs with a site dependent phase φ_n. By implementing this phase factor, we break the spatial symmetry and obtain different radiation spectra emitted from different sides of the lattice.

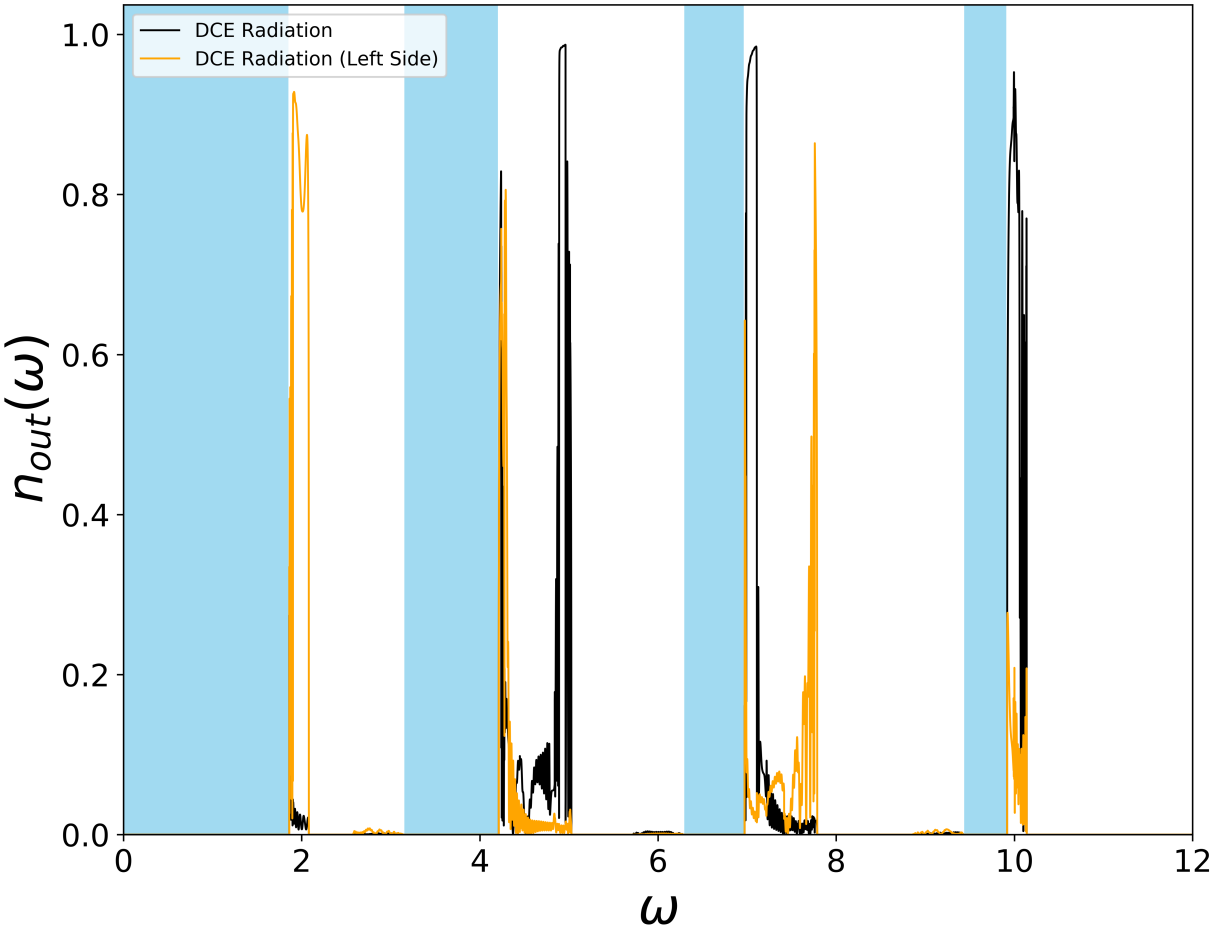

Figure 3.12: Output radiation for lattice of 100 SQUIDs driven out of phase. Introducing a phase shift factor breaks the spatial symmetry of the lattice. Here, each SQUID is driven at a phase difference of $\frac{2\pi}{3}$ with respect to the previous SQUID, effectively creating a new 3-SQUID unit cell.

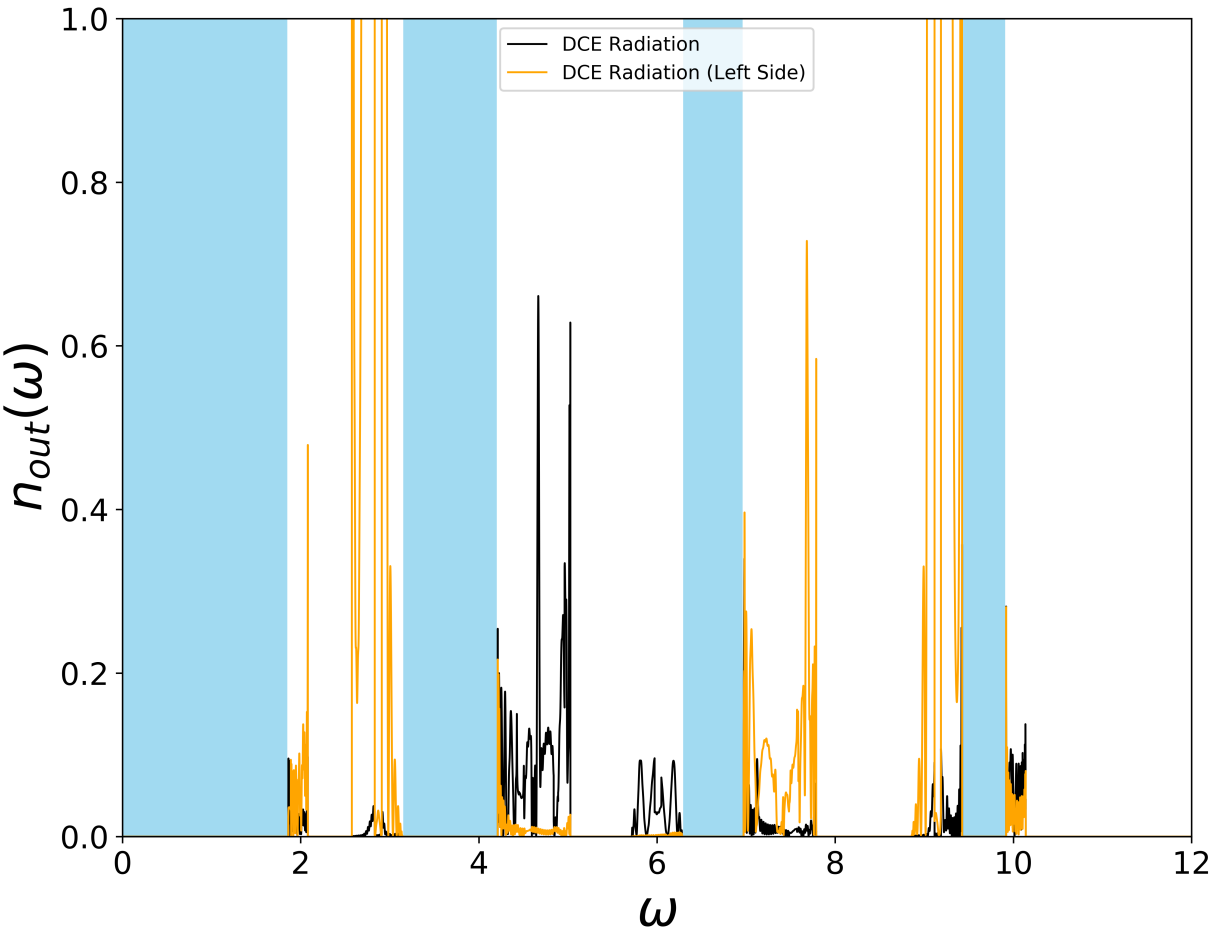

Figure 3.13: Output radiation for lattice of 100 SQUIDs driven out of phase. Phase factor = $\frac{2\pi}{5}$, 5-SQUID unit cell. Our system is highly susceptible to changes in phase.

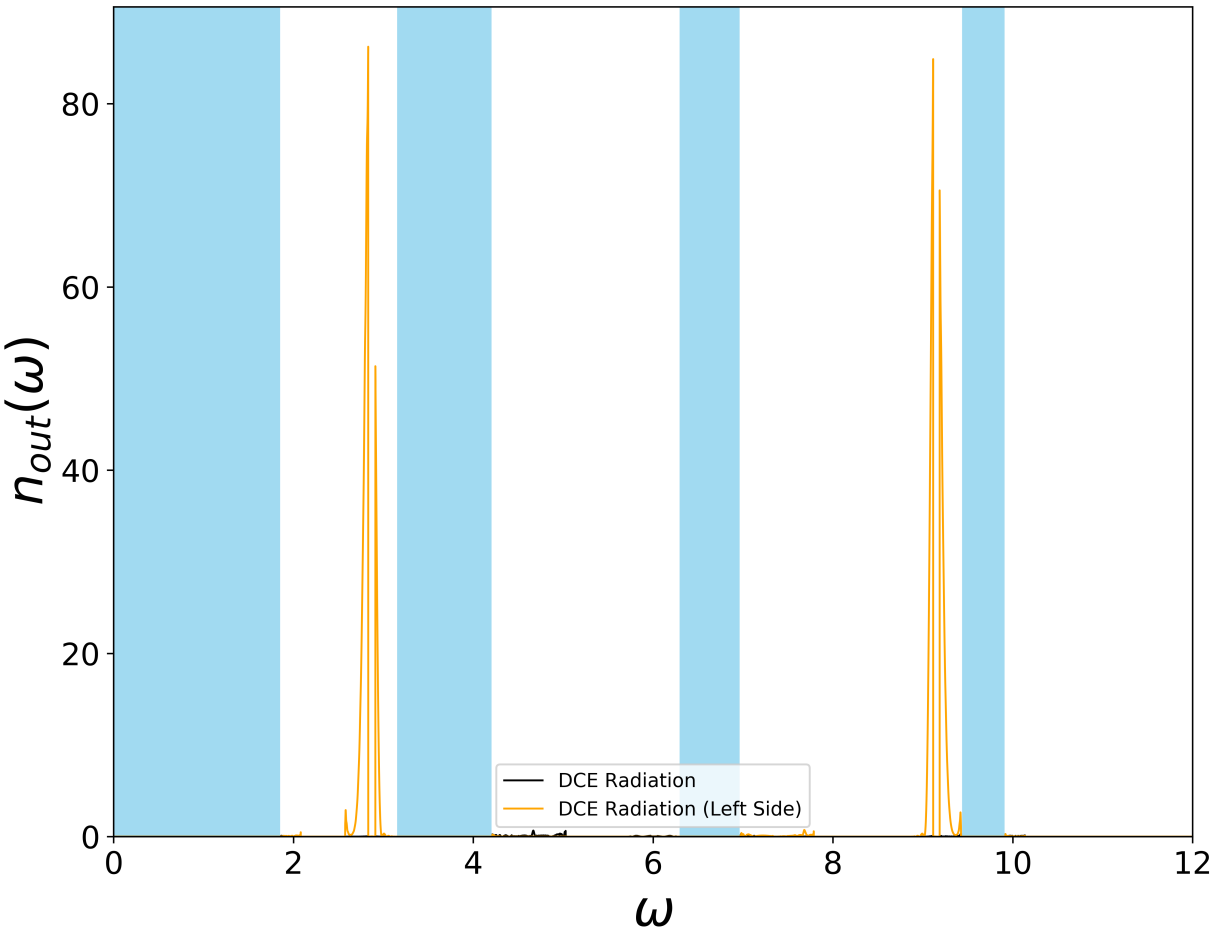

Figure 3.14: Output radiation for lattice of 100 SQUIDs driven out of phase. Phase factor = $\frac{2\pi}{5}$, 5-SQUID unit cell. Drastic difference in the left/right output radiation (quasi-unidirectionality) is achieved.

3.5 Final Remarks

We have proposed a new system in which to study the dynamical Casimir effect, as well developed a theoretical and computational model its behaviour. The resulting model exhibits non-trivial features like the presence of a band structure, and the particular way in which the DCE scattering process occur in this band structure. Moreover, the system is quite versatile. The band structure can be tuned by changing the spatial distance ℓ between SQUIDs, as well as their Josephson energy E_J^0 (which corresponds to changing the strength of the potential at each site). The harmonic drive of the SQUIDs generating the DCE radiation can be tuned in terms of the drive frequency Ω, amplitude $\delta E_{J,n}$, and phase φ_n, where the latter two parameters can be modulated for each SQUID n in the periodic array individually. This allows us to control spectral and spatial properties of the dynamical Casimir light emitted. We find a rich interplay between the band structure of the lattice, the harmonic drive of the SQUIDs, and the DCE photon-flux density, which thus allows us to control, guide, and manipulate DCE radiation.

BIBLIOGRAPHY

[1] A. AGUSTÍ, E. SOLANO, AND C. SABÍN, *Entanglement through qubit motion and the dynamical casimir effect*, Physical Review A, 99 (2019).

[2] N. ASHCROFT AND N. MERMIN, *Solid state physics*, Saunders College Publishing, 1976.

[3] H. B. G. CASIMIR, *On the attraction between two perfectly conducting plates*, Indag. Math., 10 (1948), pp. 261–263.

[4] A. CUELLAR VEGA, *Github repository*. `https://github.com/Andrescuellarvega/MS_Thesis`.

[5] V. DODONOV, *Fifty years of the dynamical casimir effect*, Physics, 2 (2020), pp. 67–104.

[6] V. V. DODONOV, A. B. KLIMOV, AND V. I. MAN'KO, *Generation of squeezed states in a resonator with a moving wall*, Physics Letters A, 149 (1990), pp. 225–228.

[7] S. FELICETTI, M. SANZ, L. LAMATA, G. ROMERO, G. JOHANSSON, P. DELSING, AND E. SOLANO, *Dynamical casimir effect entangles artificial atoms*, Physical Review Letters, 113 (2014), p. 093602.

[8] S. FULLING AND P. DAVIES, *Radiation from a moving mirror in two dimensional space-time: conformal anomaly*, Proceedings of the Royal Society of London. A. Mathematical and Physical Sciences, 348 (1976), pp. 393–414.

[9] R. GAINUTDINOV, A. GARIFULLIN, M. KHAMADEEV, AND M. SALAKHOV, *Quantum electrodynamics in photonic crystals and controllability of ionization energy of atoms*, Physics Letters A, 404 (2021), p. 127407.

[10] R. GAINUTDINOV, M. KHAMADEEV, A. AKHMADEEV, AND M. SALAKHOV, *Modification of the electromagnetic field in the photonic crystal medium and new ways of applying the photonic band gap materials*, InTech Rijeka, 2018.

[11] X. GU, A. F. KOCKUM, A. MIRANOWICZ, Y. XI LIU, AND F. NORI, *Microwave photonics with superconducting quantum circuits*, Physics Reports, 718-719 (2017), pp. 1–102.

[12] J. D. JOANNOPOULOS, S. G. JOHNSON, J. N. WINN, AND R. D. MEADE, *Photonic Crystals: Molding the Flow of Light, 2nd Edition*, Princeton University Press, 2008.

[13] J. R. JOHANSSON, G. JOHANSSON, C. M. WILSON, P. DELSING, AND F. NORI, *Nonclassical microwave radiation from the dynamical casimir effect*, Physical Review A, 87 (2013), p. 043804.

[14] J. R. JOHANSSON, G. JOHANSSON, C. M. WILSON, AND F. NORI, *Dynamical casimir effect in a superconducting coplanar waveguide*, Physical Review Letters, 103 (2009).

[15] ——, *Dynamical casimir effect in superconducting microwave circuits*, Physical Review A - Atomic, Molecular, and Optical Physics, 82 (2010).

[16] C. KITTEL, *Introduction to solid state physics*, vol. 8, Wiley New York, 1996.

[17] P. KRANTZ, M. KJAERGAARD, F. YAN, T. P. ORLANDO, S. GUSTAVSSON, AND W. D. OLIVER, *A quantum engineer's guide to superconducting qubits*, Applied Physics Reviews, 6 (2019), p. 021318.

[18] W. E. LAMB AND R. C. RETHERFORD, *Fine structure of the hydrogen atom by a microwave method*, Physical Review, 72 (1947).

[19] A. LAMBRECHT, M.-T. JAEKEL, AND S. REYNAUD, *Motion induced radiation from a vibrating cavity*, Physical Review Letters, 77 (1996).

[20] P. LÄHTEENMÄKI, G. S. PARAOANU, J. HASSEL, AND P. J. HAKONEN, *Dynamical casimir effect in a josephson metamaterial*, Proceedings of the National Academy of Sciences, 110 (2013), pp. 4234–4238.

[21] G. T. MOORE, *Quantum theory of the electromagnetic field in a variable-length one-dimensional cavity*, Journal of Mathematical Physics, 11 (1970), pp. 2679–2691.

[22] P. D. NATION, J. R. JOHANSSON, M. P. BLENCOWE, AND F. NORI, *Stimulating uncertainty: Amplifying the quantum vacuum with superconducting circuits*, Rev. Mod. Phys., (2011).

[23] B. PEROPADRE, J. HUH, AND C. SABÍN, *Dynamical casimir effect for gaussian boson sampling*, Scientific Reports, 8 (2018), p. 3751.

[24] U. VOOL AND M. DEVORET, *Introduction to quantum electromagnetic circuits*, International Journal of Circuit Theory and Applications, 45 (2017), pp. 897–934.

[25] C. M. WILSON, G. JOHANSSON, A. POURKABIRIAN, M. SIMOEN, J. R. JOHANSSON, T. DUTY, F. NORI, AND P. DELSING, *Observation of the dynamical casimir effect in a superconducting circuit*, Nature, 479 (2011), pp. 376–379.

[26] B. YURKE AND J. S. DENKER, *Quantum network theory*, Physical Review A, 29 (1984), pp. 1419–1437.

[27] S. ZHAO, Y. LONG, M. ZHANG, T. ZHENG, AND X. ZHANG, *Genuine tripartite entanglement in the dynamical casimir coupled waveguides*, Quantum Information Processing, 20 (2021), p. 308.

APPENDIX

APPENDIX

MATHEMATICA NOTEBOOK: BAND STRUCTURE OF THE KRONIG-PENNEY MODEL

The Mathematica notebook in this Appendix calculates the band structure $\omega_\nu(k)$ and Bloch functions $\psi_{\nu,k}(x) = e^{ikx}u_{\nu,k}(x)$ for the Kronig-Penney type model discussed in Section 2.2.3 using a transfer matrix approach.

```
(* Kronig-Penney model using transfer matrix *)

Clear[ell, q, p, epsilon, m]
```

In[1]:=
```
ell := {{1, 1}, {I q, -I q}}   (* matrix L *)
```

In[2]:=
```
MatrixForm[ell]
```

Out[2]//MatrixForm=

$$\begin{pmatrix} 1 & 1 \\ i\,q & -i\,q \end{pmatrix}$$

In[3]:=
```
v := {{1, 0}, {epsilon, 1}}  (* matrix V, epsilon as defined in Section 2.2 *)
```

In[4]:=
```
MatrixForm[v]
```

Out[4]//MatrixForm=

$$\begin{pmatrix} 1 & 0 \\ \text{epsilon} & 1 \end{pmatrix}$$

```
p := {{Exp[I q], 0}, {0, Exp[-I q]}}  (* matrix P *)
```

In[6]:=
```
MatrixForm[p]
```

Out[6]//MatrixForm=

$$\begin{pmatrix} e^{i\,q} & 0 \\ 0 & e^{-i\,q} \end{pmatrix}$$

In[7]:=
```
t := p.Inverse[ell, Method -> "CofactorExpansion"].v.ell  (* transfer matrix T *)

MatrixForm[t]
```

$$\begin{pmatrix} e^{i\,q} - \frac{i\,e^{i\,q}\,\text{epsilon}}{2\,q} & -\frac{i\,e^{i\,q}\,\text{epsilon}}{2\,q} \\ \frac{i\,e^{-i\,q}\,\text{epsilon}}{2\,q} & e^{-i\,q} + \frac{i\,e^{-i\,q}\,\text{epsilon}}{2\,q} \end{pmatrix}$$

```
Det[t]
```

```
1
```

```
(* Eigenvectors of transfer matrix t *)

Eigenvectors[t]
```

$$\left\{\left\{-\frac{1}{2\,\text{epsilon}}\left(\text{epsilon} + e^{2\,i\,q}\,\text{epsilon} - 2\,i\,q + 2\,i\,e^{2\,i\,q}\,q - i\,\sqrt{\left(-16\,e^{2\,i\,q}\,q^2 + \left(-i\,\text{epsilon} + i\,e^{2\,i\,q}\,\text{epsilon} - 2\,q - 2\,e^{2\,i\,q}\,q\right)^2\right)}\right), 1\right\},\right.$$
$$\left.\left\{-\frac{1}{2\,\text{epsilon}}\left(\text{epsilon} + e^{2\,i\,q}\,\text{epsilon} - 2\,i\,q + 2\,i\,e^{2\,i\,q}\,q + i\,\sqrt{\left(-16\,e^{2\,i\,q}\,q^2 + \left(-i\,\text{epsilon} + i\,e^{2\,i\,q}\,\text{epsilon} - 2\,q - 2\,e^{2\,i\,q}\,q\right)^2\right)}\right), 1\right\}\right\}$$

```
(* pasted from above *)
```

In[8]:=
```
va1[q_, epsilon_] := {-((epsilon + e^(2 i q) epsilon - 2 i q + 2 i e^(2 i q) q -
      i Sqrt[(-16 e^(2 i q) q^2 + (-i epsilon + i e^(2 i q) epsilon - 2 q - 2 e^(2 i q) q)^2)]) / (2 epsilon)), 1}
```

In[9]:=
```
v1[q_, epsilon_] := va1[q, epsilon] / Norm[va1[q, epsilon]]   (* normalized *)
```

In[10]:=
```
va2[q_, epsilon_] := {-((epsilon + e^(2 i q) epsilon - 2 i q + 2 i e^(2 i q) q +
        i Sqrt[-16 e^(2 i q) q^2 + (-i epsilon + i e^(2 i q) epsilon - 2 q - 2 e^(2 i q) q)^2])) / (2 epsilon)), 1}
```

In[11]:=
```
v2[q_, epsilon_] := va2[q, epsilon] / Norm[va2[q, epsilon]]
```

```
(* Simplified form of eigenvectors *)
(* Note: this notebook generally assumes that q = omega > 0 *)
```

In[12]:=
```
qq[q_, epsilon_] :=
 Cos[q] + (epsilon / (2 q)) Sin[q]   (* qq(q,epsilon) = cos(k) with k = wave vector *)
```

In[13]:=
```
ww[q_, epsilon_] := -Cos[q] + (2 q / epsilon) Sin[q]
```

In[14]:=
```
vv1[q_, epsilon_] :=
 {Exp[I q] (ww[q, epsilon] + (2 q / epsilon) Sqrt[1 - qq[q, epsilon]^2]), 1}
```

In[15]:=
```
vv2[q_, epsilon_] :=
 {Exp[I q] (ww[q, epsilon] - (2 q / epsilon) Sqrt[1 - qq[q, epsilon]^2]), 1}
```

```
(* Check that vv1 = va1, vv2 = va2 *)
```

```
va1[0.7, 0.1]
```

```
{12.5798 + 10.5958 i, 1}
```

```
vv1[0.7, 0.1]
```

```
{12.5798 + 10.5958 i, 1}
```

```
va2[0.7, 0.1]
```

```
{0.0465017 + 0.0391679 i, 1}
```

```
vv2[0.7, 0.1]
```

```
{0.0465017 + 0.0391679 i, 1}
```

```
(* End check *)
```

```
(* Modified, normalized eigenvectors to be used in the following *)
```

In[16]:=
```
v1norm[q_, epsilon_] := vv1[q, epsilon] / Norm[vv1[q, epsilon]]
```

In[17]:=
```
v2norm[q_, epsilon_] :=
 Exp[-I q] vv2[q, epsilon] / Norm[vv2[q, epsilon]]  (* note factor Exp[-I q] *)
```

```
(* v1norm[[1]]+v1norm[[2]] and v2norm[[1]]+v2norm[[2]] are complex conjugate,
   but only with factor Exp[-I q] in v2norm included. This is the modification. *)
```

```
v1norm[0.7, 0.1][[1]] + v1norm[0.7, 0.1][[2]]
```

```
0.82412 + 0.64303 i
```

```
v2norm[0.7, 0.1][[1]] + v2norm[0.7, 0.1][[2]]
```

```
0.82412 - 0.64303 i
```

```
(* alternative form of v2norm, further simplified *)
```

In[18]:=
```
vv2alt[q_, epsilon_] :=
 {ww[q, epsilon] - (2 q / epsilon) Sqrt[1 - qq[q, epsilon]^2], Exp[-I q]}
```

In[19]:=
```
v2normalt[q_, epsilon_] := vv2alt[q, epsilon] / Norm[vv2alt[q, epsilon]]
```

In[20]:=
```
v2normalt[0.7, 0.1][[1]] + v2normalt[0.7, 0.1][[2]]
```

Out[20]=
```
0.82412 - 0.64303 i
```

```
(* Eigenvalues mu of transfer matrix t *)
```

In[21]:=
```
Eigenvalues[t]
```

Out[21]=
$$\left\{\frac{1}{4\,q}e^{-i\,q}\left(i\,\text{epsilon}-i\,e^{2\,i\,q}\,\text{epsilon}+2\,q+2\,e^{2\,i\,q}\,q-\sqrt{\left(-16\,e^{2\,i\,q}\,q^2+\left(-i\,\text{epsilon}+i\,e^{2\,i\,q}\,\text{epsilon}-2\,q-2\,e^{2\,i\,q}\,q\right)^2\right)}\right),\ \frac{1}{4\,q}e^{-i\,q}\left(i\,\text{epsilon}-i\,e^{2\,i\,q}\,\text{epsilon}+2\,q+2\,e^{2\,i\,q}\,q+\sqrt{\left(-16\,e^{2\,i\,q}\,q^2+\left(-i\,\text{epsilon}+i\,e^{2\,i\,q}\,\text{epsilon}-2\,q-2\,e^{2\,i\,q}\,q\right)^2\right)}\right)\right\}$$

```
(* => mu = exp(+/- i k), cos(k) = cos(q) + epsilon/(2q) sin(q) =: qq(q,epsilon) *)
```

In[22]:=
```
Plot[ArcCos[x], {x, -1, 1}]
```

Out[22]=

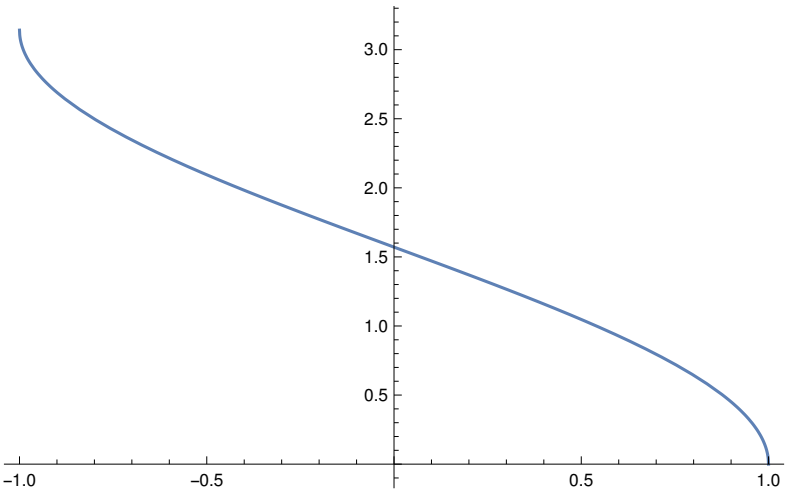

In[23]:=
```
kk[q_, epsilon_] := ArcCos[qq[q, epsilon]]
 (* k(q) wave vector, reduced range 0 < k < Pi *)
```

In[24]:=
```
epsilon := 5
```

```
(* Plot band structure q(k) = omega(k) for epsilon = 5 *)
```

```
(* A) Reduced zone scheme with -Pi<k<Pi *)
```

In[86]:=
```
komega = Plot[kk[q, epsilon], {q, 0, 14}, PlotRange → {{-0.1, 14.1}, {-0.1, 3.2}},
  PlotStyle → {Black, Thickness[0.005]}, AxesStyle → Directive[22]]
```

Out[86]=

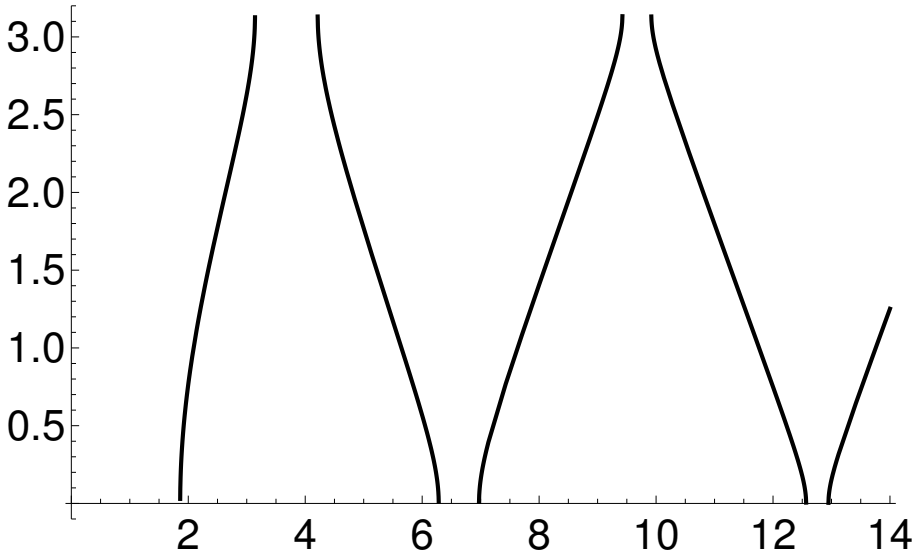

In[87]:=
```
Export["komega.png", komega, ImageResolution → 300]
```

Out[87]= komega.png

In[26]:=
```
kkmod[q_, epsilon_] := If[Abs[qq[q, epsilon]] < 1, kk[q, epsilon], 100]
 (* k(q), allow only |qq|<1 *)
```

```
(* This is the form of k(q) = k(omega) > 0 used in program *)
(* corresponding to the reduced zone scheme. *)


(* Use parametric plot to plot inverse function q(k) = omega(k) *)
```

In[27]:=
```
pos = ParametricPlot[{kkmod[q, epsilon], q},
  {q, 0, 14}, PlotRange → {{-Pi - 0.1, Pi + 0.1}, {0, 14}},
  PlotStyle → {{Black, Thickness[0.007]}}, AxesStyle → Directive[20],
  Ticks → {{-4 Pi, -3 Pi, -2 Pi, -Pi, 0, Pi, 2 Pi, 3 Pi, 4 Pi}, {1, 3, 4, 5, 8, 9, 10, 11}}]
```

Out[27]=

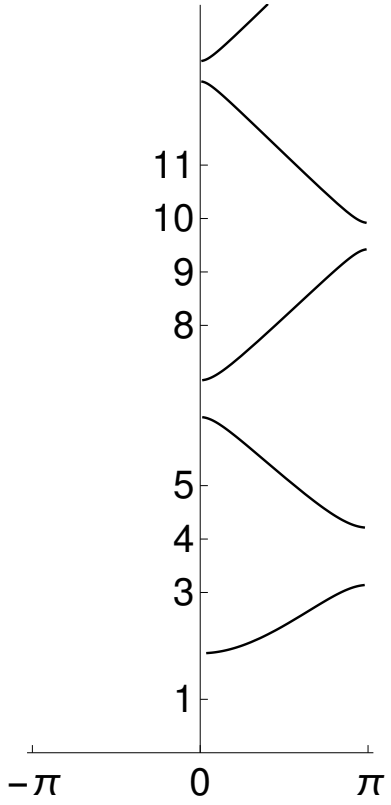

In[28]:=
```
neg = ParametricPlot[{-kkmod[q, epsilon], q},
  {q, 0, 14}, PlotRange → {{-Pi - 0.1, Pi + 0.1}, {0, 14}},
  PlotStyle → {{Black, Thickness[0.007]}}, AxesStyle → Directive[20],
  Ticks → {{-4 Pi, -3 Pi, -2 Pi, -Pi, 0, Pi, 2 Pi, 3 Pi, 4 Pi}, {1, 3, 4, 5, 8, 9, 10, 11}}]
```

Out[28]=

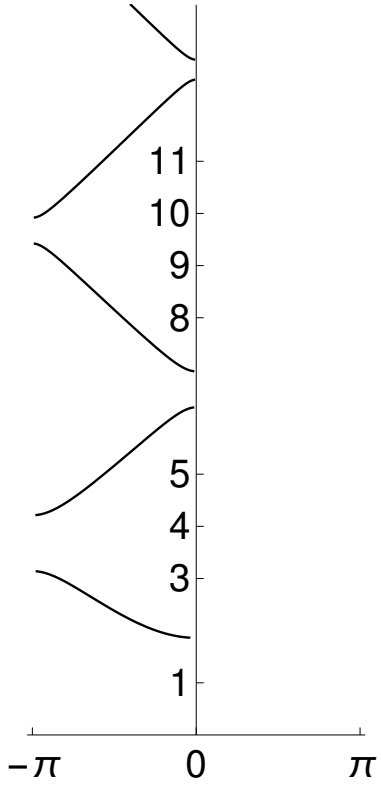

In[29]:=
```
pipos = ParametricPlot[{Pi, q}, {q, 0, 14}, PlotRange → {{-Pi - 0.1, Pi + 0.1}, {0, 14}},
  PlotStyle → {{Black, Thickness[0.0015]}}, AxesStyle → Directive[20],
  Ticks → {{-4 Pi, -3 Pi, -2 Pi, -Pi, 0, Pi, 2 Pi, 3 Pi, 4 Pi}, {1, 3, 4, 5, 8, 9, 10, 11}}]
```

Out[29]=

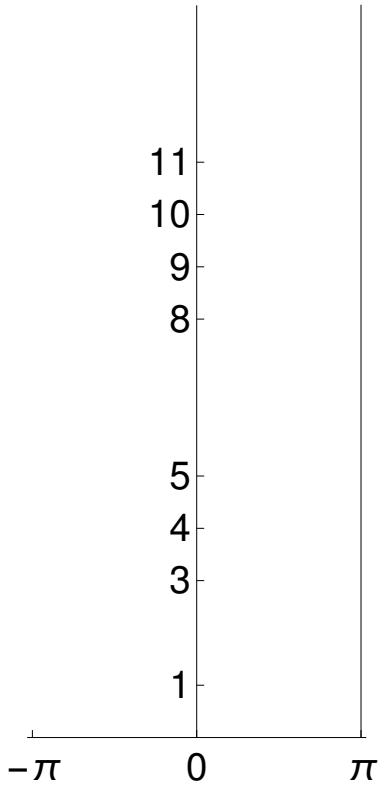

In[30]:=
```
pineg = ParametricPlot[{-Pi, q}, {q, 0, 14}, PlotRange → {{-Pi - 0.1, Pi + 0.1}, {0, 14}},
  PlotStyle → {{Black, Thickness[0.0015]}}, AxesStyle → Directive[20],
  Ticks → {{-4 Pi, -3 Pi, -2 Pi, -Pi, 0, Pi, 2 Pi, 3 Pi, 4 Pi}, {1, 3, 4, 5, 8, 9, 10, 11}}]
```

Out[30]=

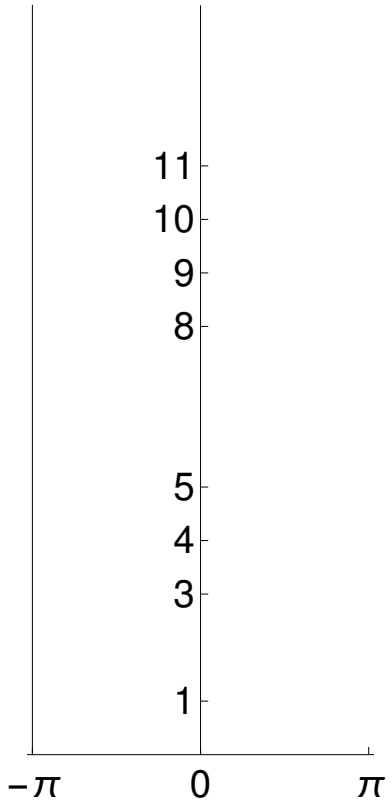

```
bandreduced = Show[neg, pos, pipos, pineg]   (* dispersion relation q(k) = omega(k) *)
```

Out[31]=

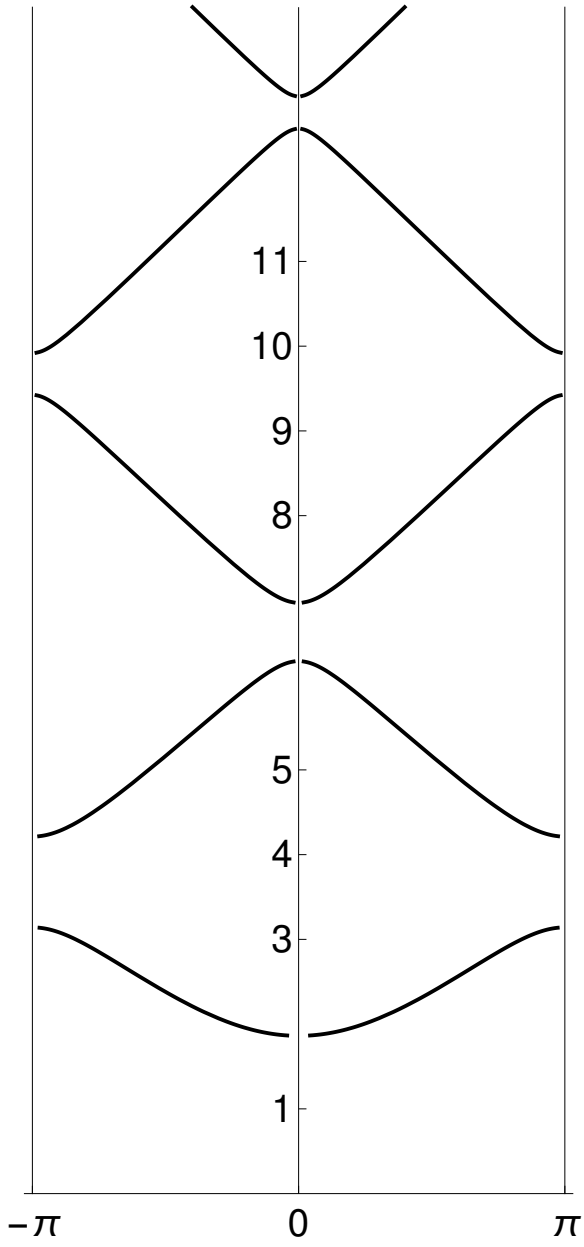


```
Export["bs_reduced.png", bandreduced, ImageResolution → 300]
```

bs_reduced.png

```
(* This is the dispersion relation q(k) = omega(k) used in the program *)
(* corresponding to reduced zone scheme. *)


(* Find gaps to 7 digits (for epsilon = 5) *)
```

```
Plot[kk[q, epsilon], {q, 0, 14}]    (* k(q) wave vector, reduced range 0 < k < Pi *)
```

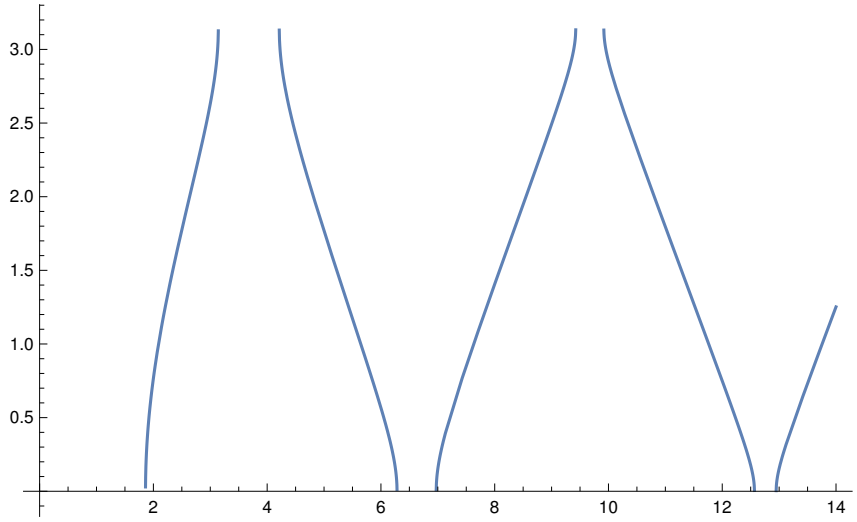


```
kk[1.861514, epsilon]    (* first allowed in 1. band *)
```

```
0.00149712
```

In[32]:=
```
first1 := 1.861514        (* first allowed q=omega in 1. band *)
```

```
kk[Pi, epsilon]           (* last allowed in 1. band = Pi *)
```

π

In[33]:=
```
last1 = Pi - 0.000001
```

Out[33]=
```
3.14159
```

```
kk[4.2127514, epsilon]    (* first allowed in 2. band *)
```

```
3.14132
```

In[34]:=
```
first2 := 4.2127514
```

```
kk[2 Pi, epsilon]         (* last allowed in 2. band = 2 Pi *)
```

```
0
```

In[35]:=
```
last2 = 2 Pi - 0.000001
```

Out[35]=
```
6.28318
```

```
kk[6.971795, epsilon]     (* first allowed in 3. band *)
```

```
0.000349891
```

In[36]:=
```
first3 := 6.971795
```

```
kk[3 * Pi, epsilon]        (* last allowed in 3. band = 3 Pi *)
```

π

In[37]:=
```
last3 = 3 Pi - 0.000001
```

Out[37]= 9.42478

```
kk[9.918596, epsilon]     (* first allowed in 4. band *)
```

3.14116

In[38]:=
```
first4 := 9.918596
```

```
kk[4 Pi, epsilon]         (* last allowed in 4. band = 4 Pi *)
```

0

In[39]:=
```
last4 = 4 Pi - 0.000001
```

Out[39]= 12.5664

```
kk[12.947842, epsilon]    (* first allowed in 5. band *)
```

0.000598452

In[40]:=
```
first5 := 12.947842
```

In[41]:=
```
last5 := 14
```

```
(* B) Extended zone scheme *)
(* Only for illustration,not used in program *)
```

```
pos1 = ParametricPlot[{kkmod[q, epsilon], q},
  {q, first1, last1}, PlotRange → {{-4.5 Pi - 0.1, 4.5 Pi + 0.1}, {0, 14}},
  PlotStyle → {{Black, Thickness[0.003]}}, AxesStyle → Directive[10],
  Ticks → {{-4 Pi, -3 Pi, -2 Pi, -Pi, 0, Pi, 2 Pi, 3 Pi, 4 Pi}, {4, 6, 8, 10, 12, 14}}]
```

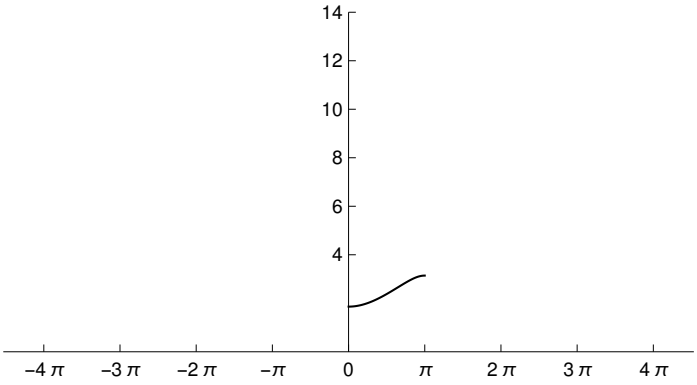


```
neg1 = ParametricPlot[{-kkmod[q, epsilon], q},
  {q, first1, last1}, PlotRange → {{-4.5 Pi - 0.1, 4.5 Pi + 0.1}, {0, 14}},
  PlotStyle → {{Black, Thickness[0.003]}}, AxesStyle → Directive[10],
  Ticks → {{-4 Pi, -3 Pi, -2 Pi, -Pi, 0, Pi, 2 Pi, 3 Pi, 4 Pi}, {4, 6, 8, 10, 12, 14}}]
```

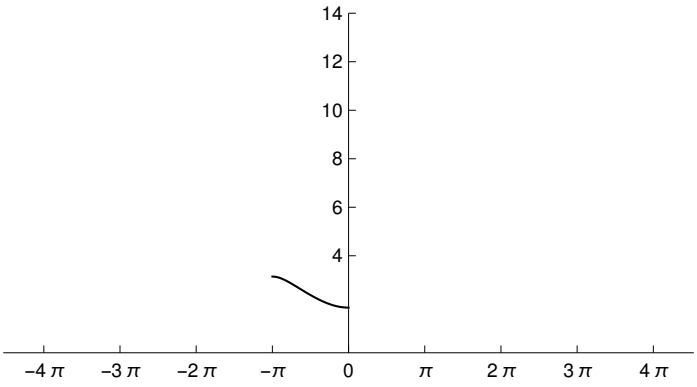

```
pos2 = ParametricPlot[{-kkmod[q, epsilon] + 2 Pi, q},
  {q, first2, last2}, PlotRange → {{-4.5 Pi - 0.1, 4.5 Pi + 0.1}, {0, 14}},
  PlotStyle → {{Black, Thickness[0.003]}}, AxesStyle → Directive[10],
  Ticks → {{-4 Pi, -3 Pi, -2 Pi, -Pi, 0, Pi, 2 Pi, 3 Pi, 4 Pi}, {4, 6, 8, 10, 12, 14}}]
```

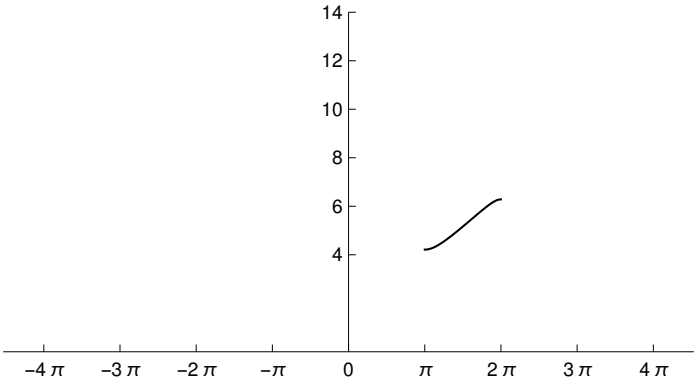


```
neg2 = ParametricPlot[{kkmod[q, epsilon] - 2 Pi, q},
  {q, first2, last2}, PlotRange → {{-4.5 Pi - 0.1, 4.5 Pi + 0.1}, {0, 14}},
  PlotStyle → {{Black, Thickness[0.003]}}, AxesStyle → Directive[10],
  Ticks → {{-4 Pi, -3 Pi, -2 Pi, -Pi, 0, Pi, 2 Pi, 3 Pi, 4 Pi}, {4, 6, 8, 10, 12, 14}}]
```

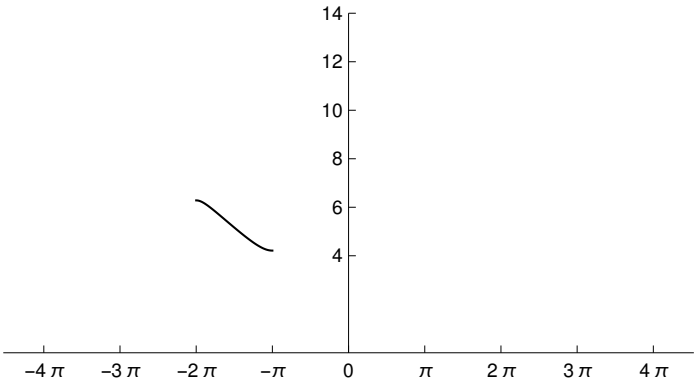

```
pos3 = ParametricPlot[{kkmod[q, epsilon] + 2 Pi, q},
  {q, first3, last3}, PlotRange → {{-4.5 Pi - 0.1, 4.5 Pi + 0.1}, {0, 14}},
  PlotStyle → {{Black, Thickness[0.003]}}, AxesStyle → Directive[10],
  Ticks → {{-4 Pi, -3 Pi, -2 Pi, -Pi, 0, Pi, 2 Pi, 3 Pi, 4 Pi}, {4, 6, 8, 10, 12, 14}}]
```

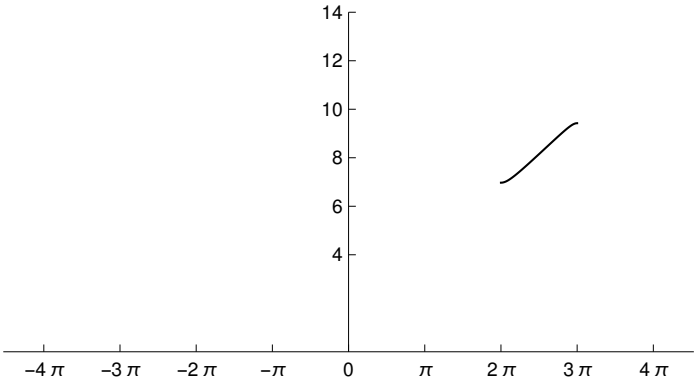


```
neg3 = ParametricPlot[{-kkmod[q, epsilon] - 2 Pi, q},
  {q, first3, last3}, PlotRange → {{-4.5 Pi - 0.1, 4.5 Pi + 0.1}, {0, 14}},
  PlotStyle → {{Black, Thickness[0.003]}}, AxesStyle → Directive[10],
  Ticks → {{-4 Pi, -3 Pi, -2 Pi, -Pi, 0, Pi, 2 Pi, 3 Pi, 4 Pi}, {4, 6, 8, 10, 12, 14}}]
```

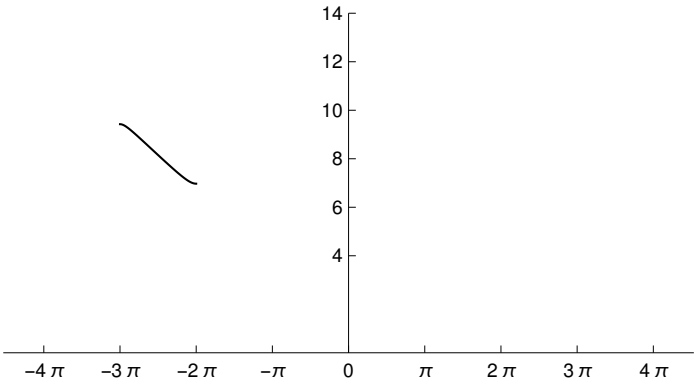

```
pos4 = ParametricPlot[{-kkmod[q, epsilon] + 4 Pi, q},
  {q, first4, last4}, PlotRange → {{-4.5 Pi - 0.1, 4.5 Pi + 0.1}, {0, 14}},
  PlotStyle → {{Black, Thickness[0.003]}}, AxesStyle → Directive[10],
  Ticks → {{-4 Pi, -3 Pi, -2 Pi, -Pi, 0, Pi, 2 Pi, 3 Pi, 4 Pi}, {4, 6, 8, 10, 12, 14}}]
```

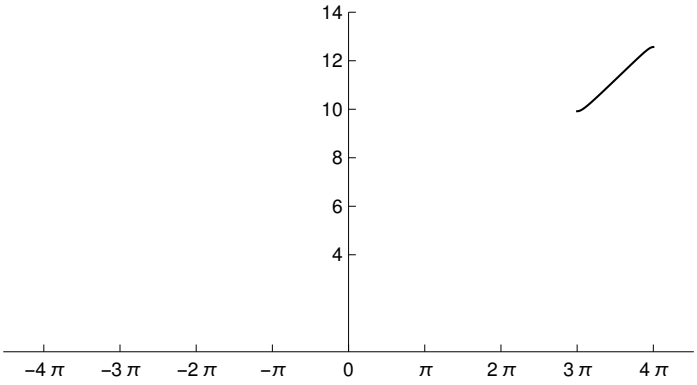


```
neg4 = ParametricPlot[{kkmod[q, epsilon] - 4 Pi, q},
  {q, first4, last4}, PlotRange → {{-4.5 Pi - 0.1, 4.5 Pi + 0.1}, {0, 14}},
  PlotStyle → {{Black, Thickness[0.003]}}, AxesStyle → Directive[10],
  Ticks → {{-4 Pi, -3 Pi, -2 Pi, -Pi, 0, Pi, 2 Pi, 3 Pi, 4 Pi}, {4, 6, 8, 10, 12, 14}}]
```

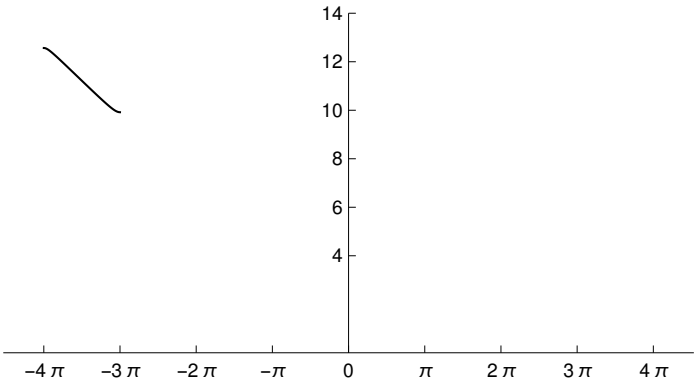

```
pos5 = ParametricPlot[{kkmod[q, epsilon] + 4 Pi, q},
  {q, first5, last5}, PlotRange → {{-4.5 Pi - 0.1, 4.5 Pi + 0.1}, {0, 14}},
  PlotStyle → {{Black, Thickness[0.003]}}, AxesStyle → Directive[10],
  Ticks → {{-4 Pi, -3 Pi, -2 Pi, -Pi, 0, Pi, 2 Pi, 3 Pi, 4 Pi}, {4, 6, 8, 10, 12, 14}}]
```

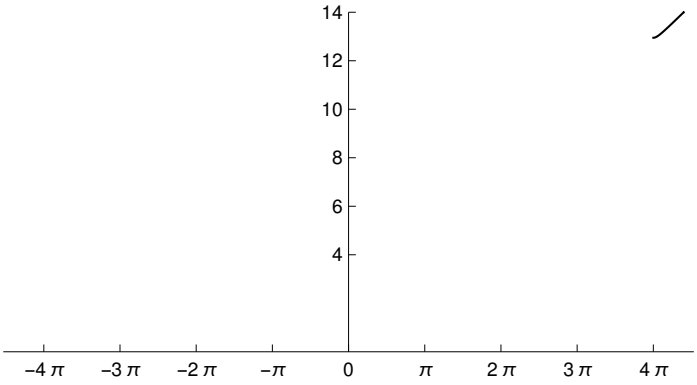


```
neg5 = ParametricPlot[{-kkmod[q, epsilon] - 4 Pi, q},
  {q, first5, last5}, PlotRange → {{-4.5 Pi - 0.1, 4.5 Pi + 0.1}, {0, 14}},
  PlotStyle → {{Black, Thickness[0.003]}}, AxesStyle → Directive[10],
  Ticks → {{-4 Pi, -3 Pi, -2 Pi, -Pi, 0, Pi, 2 Pi, 3 Pi, 4 Pi}, {4, 6, 8, 10, 12, 14}}]
```

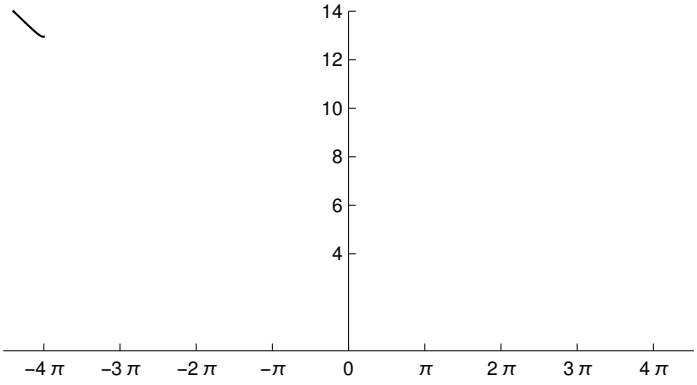

```
bandextended = Show[pos1, neg1, pos2, neg2, pos3, neg3, pos4, neg4, pos5, neg5]
```

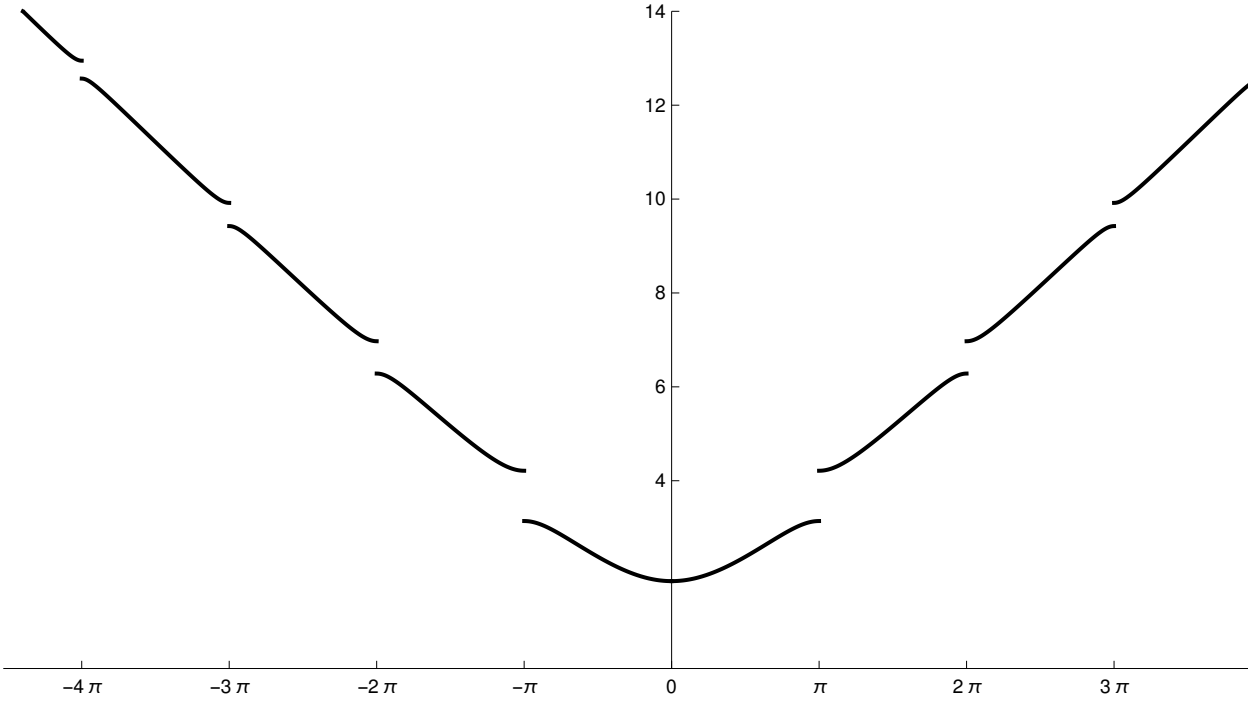


```
(* Only for illustration, not used in program *)
Export["bs_extended.png", bandextended, ImageResolution → 300]
bs_extended.png
(* End Illustration *)
{first1, last1, first2, last2, first3, last3, first4, last4, first5, last5}
{1.86151, 3.14159, 4.21275, 6.28318, 6.9718, 9.42478, 9.9186, 12.5664, 12.9478, 14}
```

```
(* Now define function k(q) explicitly in extended zone scheme *)
(* Only for illustration, not used in program *)
test[x_] := Piecewise[{{x^2, x > 0 && x < 3}, {1 / x, x > 3}}, 0]
```

```
Plot[test[x], {x, -2, 10}, PlotRange → {0, 10}]
```

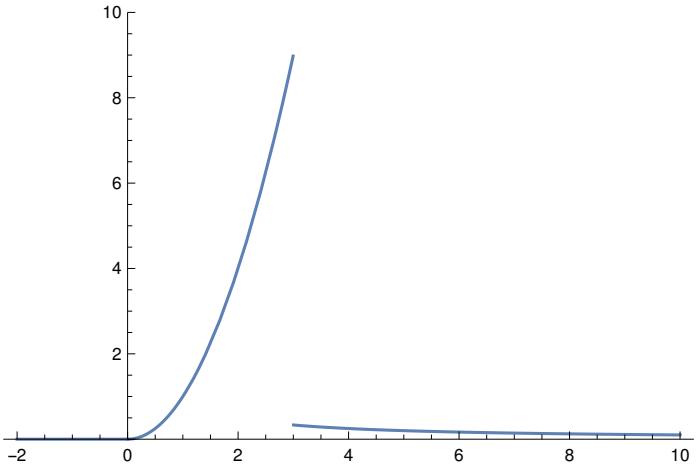


```
(* kkext[q] returns positive k[q]>0 for allowed q=
 omega and 0 for not allowed q=omega *)

kkext[q_, epsilon_] := Piecewise[{{kk[q, epsilon], Abs[q] > first1 && Abs[q] < last1},
   {-kk[q, epsilon] + 2 Pi, Abs[q] > first2 && Abs[q] < last2},
   {kk[q, epsilon] + 2 Pi, Abs[q] > first3 && Abs[q] < last3},
   {-kk[q, epsilon] + 4 Pi, Abs[q] > first4 && Abs[q] < last4},
   {kk[q, epsilon] + 4 Pi, Abs[q] > first5 && Abs[q] < last5}}, 0]


epsilon := 5

Plot[kkext[q, epsilon], {q, -15, 15},
 PlotRange -> {{-14, 14}, {-0.1, 15}}, PlotStyle → {Blue, Thickness[0.003]}]
```

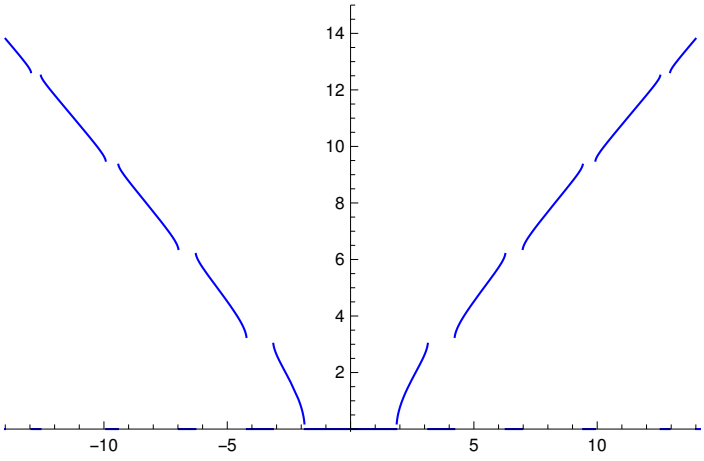

```
In[42]:= qq[q, eps]    (* qq(q,epsilon) = cos(k) with k = wave vector *)
Out[42]= Cos[q] + (eps Sin[q])/(2 q)

         (* Derivative dk/dq *)

In[43]:= kkprime[q_, epsilon_] := Derivative[1, 0][kkmod][q, epsilon]

         (* Analytical expression for Abs[dk/dq] *)

In[44]:= kkprimetest[q_, epsilon_] :=
          Abs[(1 + epsilon / (2 q^2)) Sin[q] - (epsilon / (2 q)) Cos[q]] / Sqrt[1 - qq[q, epsilon]^2]

In[45]:= epsilon := 5

In[46]:= kkprime[2.1, epsilon]     (* check in 1st band *)
Out[46]= 2.29166

In[47]:= kkprimetest[2.1, epsilon]
Out[47]= 2.29166

In[48]:= kkprime[4.7, epsilon]     (* check in 2nd band *)
Out[48]= -1.31896

In[49]:= kkprimetest[4.7, epsilon]
Out[49]= 1.31896

In[50]:= kkprime[7.5, epsilon]     (* check in 3rd band *)
Out[50]= 1.14931

In[51]:= kkprimetest[7.5, epsilon]
Out[51]= 1.14931

In[52]:= kkprime[11.2, epsilon]    (* check in 4th band *)
Out[52]= -1.04413

In[53]:= kkprimetest[11.2, epsilon]
Out[53]= 1.04413
```

In[54]:=
```
Plot[Abs[kkprime[q, epsilon]], {q, -15, 15},
 PlotRange -> {{-14, 14}, {-0.1, 15}}, PlotStyle → {Blue, Thickness[0.003]}]
```

Out[54]=

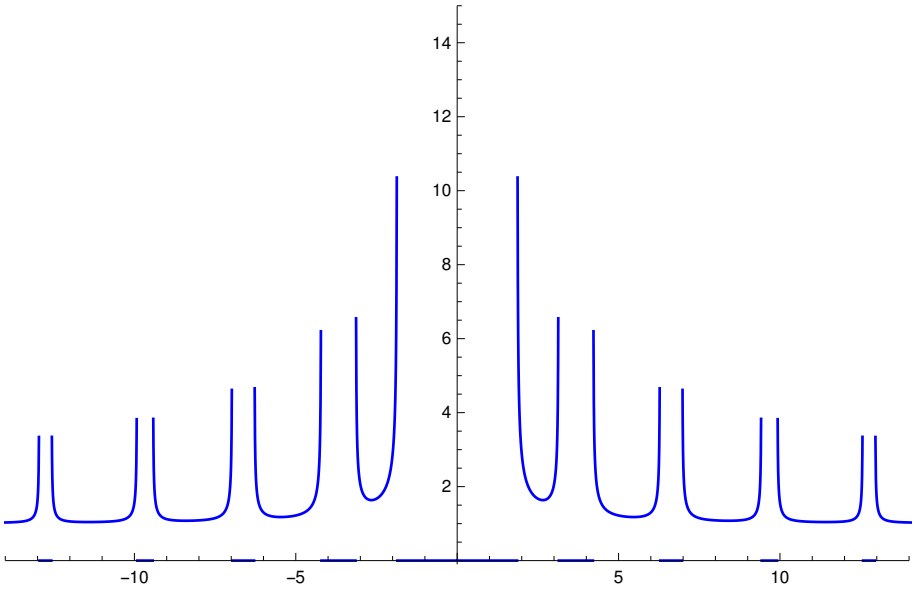


```
(* Only allowed q=omega should be used *)
```

In[55]:=
```
domega[q_, epsilon_] := Sqrt[Abs[kkprime[q, epsilon]]]   (* function domega(q) *)
```

In[56]:=
```
Plot[domega[q, epsilon], {q, -15, 15},
 PlotRange -> {{-14, 14}, {-0.1, 4}}, PlotStyle → {Blue, Thickness[0.003]}]
```

Out[56]=

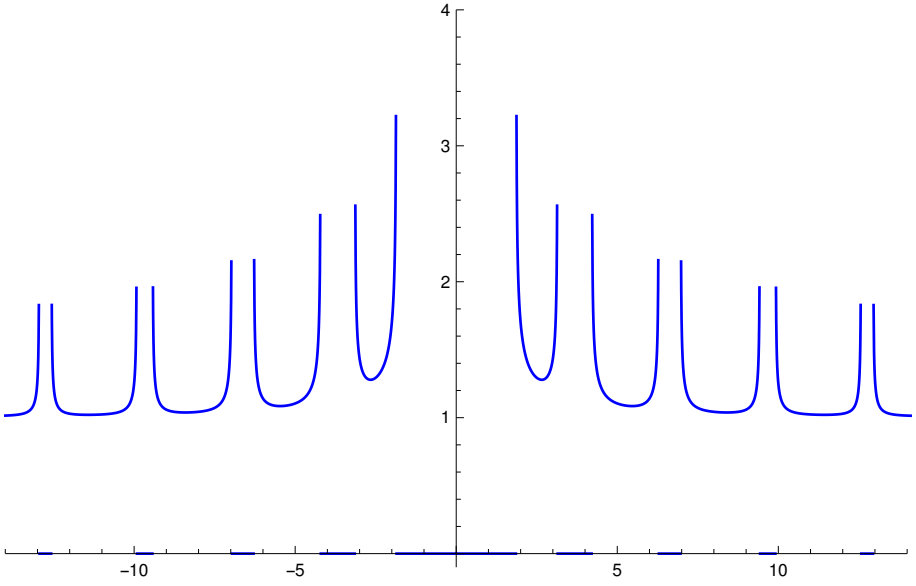


```
(* Bloch functions Phi(x) with additional normalization *)

(* allow only |qq|<1 where qq = Cos[q]+(epsilon/(2q))Sin[q] *)
```

```
(* in what follows: index 1 = +k, index 2 = -k *)

In[57]:= exp1[q_, epsilon_, n_] :=
 If[Abs[qq[q, epsilon]] < 1, Exp[I kk[q, epsilon] n], 0]   (* k1 > 0 *)

In[58]:= exp2[q_, epsilon_, n_] :=
 If[Abs[qq[q, epsilon]] < 1, Exp[-I kk[q, epsilon] n], 0]  (* k2 = -k1 < 0 *)

(* phi1raw, phi2raw not correctly normalized,
missing normalization factors norm1,  norm2 below *)

In[59]:= phi1raw[x_, n_, q_, epsilon_] := exp1[q, epsilon, n]
   (v1norm[q, epsilon][[1]] Exp[I q (x - n)] + v1norm[q, epsilon][[2]] Exp[-I q (x - n)]) /
    (v1norm[q, epsilon][[1]] + v1norm[q, epsilon][[2]])

In[60]:= phi2raw[x_, n_, q_, epsilon_] := exp2[q, epsilon, n]
   (v2norm[q, epsilon][[1]] Exp[I q (x - n)] + v2norm[q, epsilon][[2]] Exp[-I q (x - n)]) /
    (v2norm[q, epsilon][[1]] + v2norm[q, epsilon][[2]])



In[61]:= epsilon := 5

(* functions u(x) for 0<x<1, then periodically extended *)

In[62]:= u1raw[x_, q_, epsilon_] := (v1norm[q, epsilon][[1]] Exp[I (q - kk[q, epsilon]) (x - 1)] +
     v1norm[q, epsilon][[2]] Exp[-I (q + kk[q, epsilon]) (x - 1)]) /
   (v1norm[q, epsilon][[1]] + v1norm[q, epsilon][[2]])

In[63]:= norm1[q_, epsilon_] :=
 Sqrt[NIntegrate[u1raw[x, q, epsilon] Conjugate[u1raw[x, q, epsilon]], {x, 0, 1}]]

(* u1 correctly normalized used in program *)

In[64]:= u1[x_, q_, epsilon_] := u1raw[x, q, epsilon] / norm1[q, epsilon]

NIntegrate[u1[x, 2.1, epsilon] Conjugate[u1[x, 2.1, epsilon]], {x, 0, 1}]

Out[65]= 1.

In[66]:= u2raw[x_, q_, epsilon_] := (v2norm[q, epsilon][[1]] Exp[I (q + kk[q, epsilon]) (x - 1)] +
     v2norm[q, epsilon][[2]] Exp[-I (q - kk[q, epsilon]) (x - 1)]) /
   (v2norm[q, epsilon][[1]] + v2norm[q, epsilon][[2]])

In[67]:= norm2[q_, epsilon_] :=
 Sqrt[NIntegrate[u2raw[x, q, epsilon] Conjugate[u2raw[x, q, epsilon]], {x, 0, 1}]]

(* u2 correctly normalized used in program *)

In[68]:= u2[x_, q_, epsilon_] := u2raw[x, q, epsilon] / norm2[q, epsilon]
```

```
NIntegrate[u2[x, 4.7, epsilon] Conjugate[u2[x, 4.7, epsilon]], {x, 0, 1}]
```

Out[69]= 1.

```
(* Show u_{-k}(x) = u_k^*(x) for all x; u1 is for k, u2 is for -k  *)
u1[0.7, 2.1, epsilon]
```

1.07325 − 0.0663097 i

```
u2[0.7, 2.1, epsilon]
```

1.07325 + 0.0663097 i

```
u1[3.25, 4.71, epsilon]
```

− 0.72853 + 0.160454 i

```
u2[3.25, 4.71, epsilon]
```

− 0.72853 − 0.160454 i

In[70]:=
```
(* Show u(0) = u(1) real and equal for k, -k *)
```

In[71]:=
```
eps := 5
```

In[72]:=
```
q := 2.1
```

In[73]:=
```
u1[0, q, eps]
```

Out[73]= $0.664728 - 9.5709 \times 10^{-17}$ i

In[74]:=
```
u1[1, q, eps]
```

Out[74]= $0.664728 + 1.15312 \times 10^{-18}$ i

In[75]:=
```
u2[0, q, eps]
```

Out[75]= $0.664728 + 9.5709 \times 10^{-17}$ i

In[76]:=
```
u2[1, q, eps]
```

Out[76]= 0.664728 + 0. i

```
q := 4.71        (* 2nd branch *)
u1[0, q, eps]
```

$0.948549 - 3.1593 \times 10^{-16}$ i

```
u1[1, q, eps]
```

$0.948549 - 5.26551 \times 10^{-17}$ i

```
u2[0, q, eps]
```

$0.948549 + 3.1593 \times 10^{-16}$ i

```
u2[1, q, eps]
```

$0.948549 + 0.\,i$

```
(* Show u1=u2=1 for epsilon=0 and first branch *)
```

```
q = 2.1   (* 1st branch *)
```

2.1

```
u1[2.1, q, 0.0000000001]
```

$1. + 3.22605 \times 10^{-11}\,i$

```
u2[0.9, q, 0.0000000001]
```

$1. + 2.38087 \times 10^{-12}\,i$

```
q = 4.71   (* 2nd branch *)
```

4.71

```
u1[2.1, q, 0.0000000001]
```

$0.809017 - 0.587785\,i$

```
u2[0.9, q, 0.0000000001]
```

$0.809017 - 0.587785\,i$

```
(* functions c(q), d(q) *)
```

In[77]:=
```
u1prime[x_, q_, epsilon_] :=
 Derivative[1, 0, 0][u1raw][x, q, epsilon] / norm1[q, epsilon]  (* k>0 *)
```

In[78]:=
```
u2prime[x_, q_, epsilon_] :=
 Derivative[1, 0, 0][u2raw][x, q, epsilon] / norm2[q, epsilon]  (* k<0 *)
```

In[79]:=
```
(* Show epsilon = [u'(0) - u'(1)]/u(0)  for k, -k *)
```

In[80]:=
```
eps := 5
```

```
q := 2.1
```

```
(u1prime[0, q, eps] - u1prime[1, q, eps]) / u1[0, q, eps]
```

$5. + 5.1834 \times 10^{-17}\,i$

```
(u2prime[0, q, eps] - u2prime[1, q, eps]) / u1[0, q, eps]
```

$5. + 2.3901 \times 10^{-15}\,i$

```
q := 4.71
```

```
(u1prime[0, q, eps] - u1prime[1, q, eps]) / u1[0, q, eps]
```

$5. - 2.07375 \times 10^{-16}\,i$

```
(u2prime[0, q, eps] - u2prime[1, q, eps]) / u1[0, q, eps]
```

```
5. + 2.60169 × 10^-15 i
```

```
q := 7.1
```

```
(u1prime[0, q, eps] - u1prime[1, q, eps]) / u1[0, q, eps]
```

```
5. + 2.58146 × 10^-16 i
```

```
(u2prime[0, q, eps] - u2prime[1, q, eps]) / u1[0, q, eps]
```

```
5. + 1.76432 × 10^-15 i
```

```
(* end check *)
```

```
eps := 5
```

```
q := 2.1
```

```
u1prime[0, q, eps]
```

```
1.66182 + 0.700078 i
```

```
u1prime[1, q, eps]
```

```
- 1.66182 + 0.700078 i
```

```
u2prime[0, q, eps]
```

```
1.66182 - 0.700078 i
```

```
u2prime[1, q, eps]
```

```
- 1.66182 - 0.700078 i
```

```
q := 4.71
```

```
u1prime[0, q, eps]
```

```
2.37137 - 5.80308 i
```

```
u1prime[1, q, eps]
```

```
- 2.37137 - 5.80308 i
```

```
u2prime[0, q, eps]
```

```
2.37137 + 5.80308 i
```

```
u2prime[1, q, eps]
```

```
- 2.37137 + 5.80308 i
```

In[81]:=
```
c[q_, epsilon_] := u1[0, q, epsilon]  (* cal C *)

(* c real and equal for (1), (2) *)

eps := 5

q := 2.1

c[q, eps]
```

$0.664728 - 9.5709 \times 10^{-17}\, i$

```
u2[0, q, eps]
```

$0.664728 + 9.5709 \times 10^{-17}\, i$

```
u1[1, q, epsilon]
```

$0.664728 + 1.15312 \times 10^{-18}\, i$

```
u2[1, q, epsilon]
```

$0.664728 + 0.\, i$

```
c[2, 3]
```

$0.762883 + 3.46945 \times 10^{-17}\, i$

```
u2[0, 2, 3]
```

$0.762883 - 4.16334 \times 10^{-17}\, i$

```
d[q_, epsilon_] := u1prime[0, q, epsilon]   (* cal D *)

(* d complex and conjugate for (1), (2) *)

eps := 5

q := 2.1

d[q, eps]
```

$1.66182 + 0.700078\, i$

```
u2prime[0, q, eps]
```

$1.66182 - 0.700078\, i$

```
d[4.71, eps]
```

$2.37137 - 5.80308\, i$

```
u2prime[0, 4.71, eps]
```

$2.37137 + 5.80308\, i$

```
Abs[qq[1.1, 1.348]]  (* epsilon=1.348 is critical value for q=1.1 *)
```

```
0.999663
```

```
Plot[{Re[u1[0.4, 1.1, eps]], Re[u2[0.4, 1.1, eps]]}, {eps, 0, 2}, PlotStyle → Black]
```

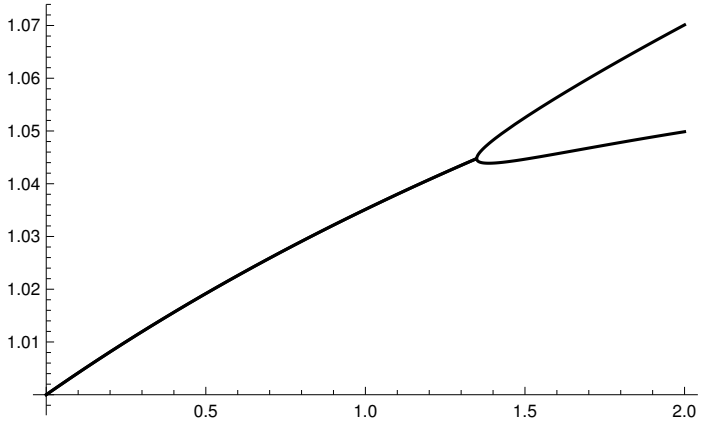


```
Plot[{Im[u1[0.4, 1.1, eps]], Im[u2[0.4, 1.1, eps]]}, {eps, 0, 2}, PlotStyle → Black]
```

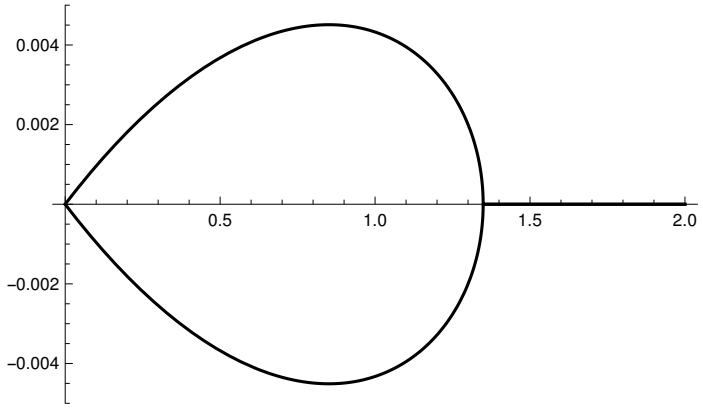


```
(* Plot real part of u(x) for epsilon=5, q=omega=2 *)
```

```
eps := 5
```

```
q := 2
```

```
pu1 = Plot[Re[u1[x, q, eps]], {x, 0, 1}, PlotStyle → Black]
```

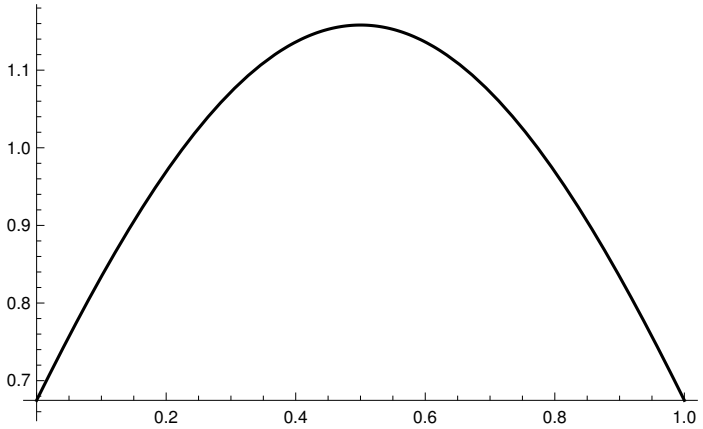


```
Export["u_real_eps5_omega2.png", pu1, ImageResolution → 300]
```

```
u_real_eps5_omega2.png
```

```
pu2 = Plot[Re[u2[x, q, eps]], {x, 0, 1}, PlotStyle → {Blue, Dashed}]
```

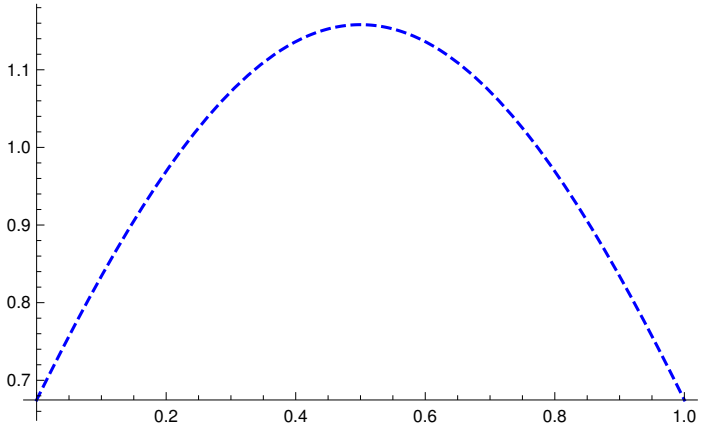


```
Show[pu1, pu2]
```

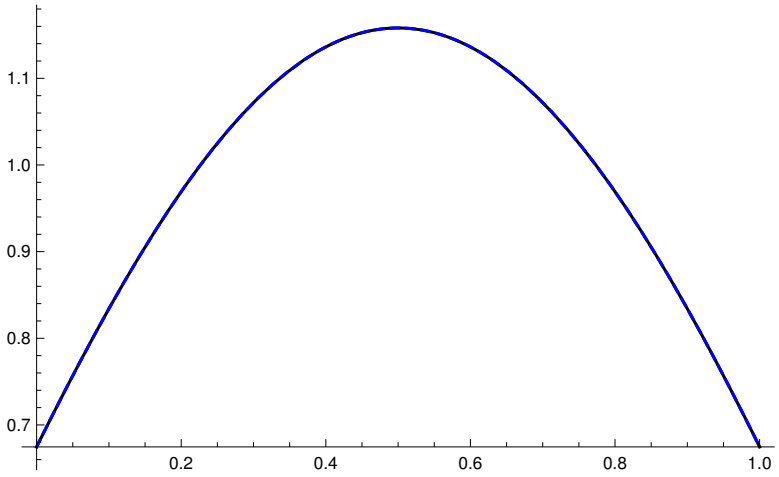

```
(* plot imaginary part of u(x) *)
pu3 = Plot[Im[u1[x, q, eps]], {x, 0, 1}, PlotStyle → Black]
```

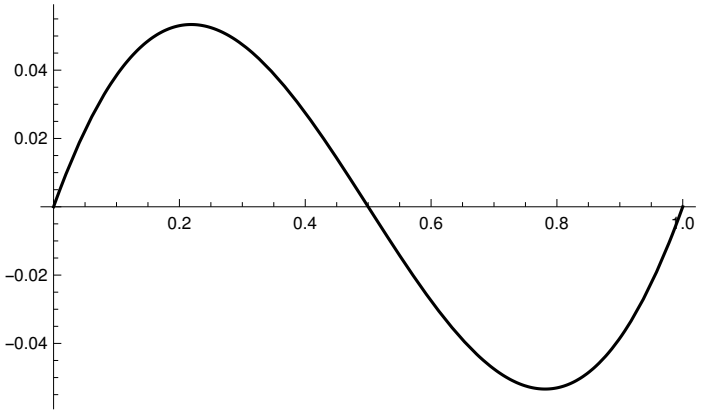


```
pu4 = Plot[Im[u2[x, q, eps]], {x, 0, 1}, PlotStyle → {Blue}]
```

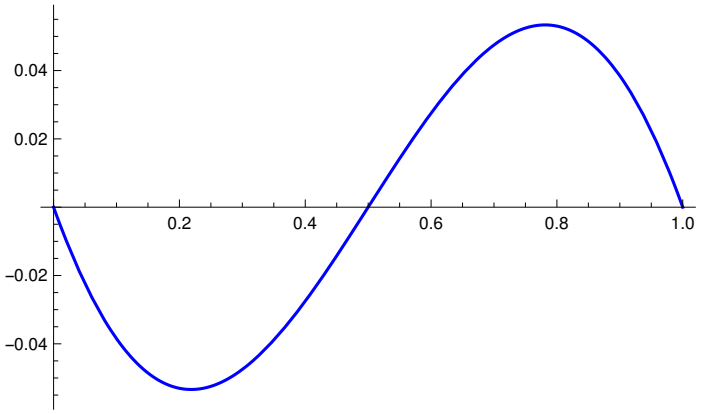


```
uim = Show[pu3, pu4]
```

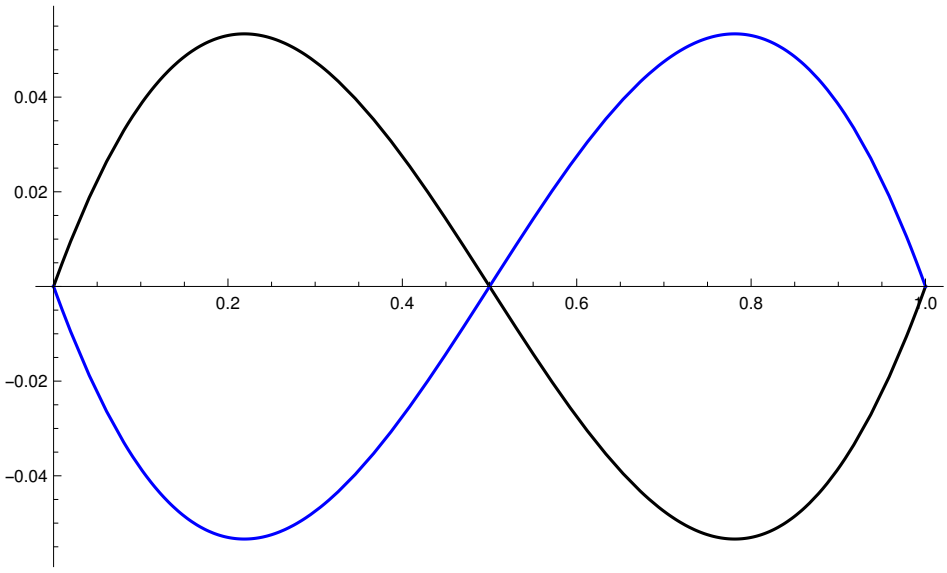

```
Export["u_imaginary_eps5_omega2.png", uim, ImageResolution → 300]
```

u_imaginary_eps5_omega2.png

```
(* Plot real and imaginary parts of Bloch functions Phi(x) *)
(* Show Phi_2 = complex conjugate Phi_1 *)
eps := 5
q := 2
p1 = Plot[Re[phi1raw[x, Ceiling[x], q, eps]] / norm1[q, epsilon] ,
  {x, 0, 20}, PlotStyle → Black]
```

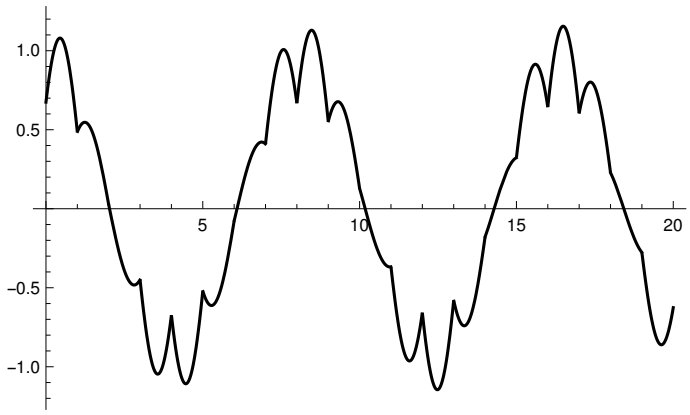


```
Export["Bloch_real_eps5_omega2.png", p1, ImageResolution → 300]
```

Bloch_real_eps5_omega2.png

```
p2 = Plot[Re[phi2raw[x, Ceiling[x], q, eps]] / norm2[q, epsilon],
  {x, 0, 20}, PlotStyle → Blue]    (* same as Re(phi1) *)
```

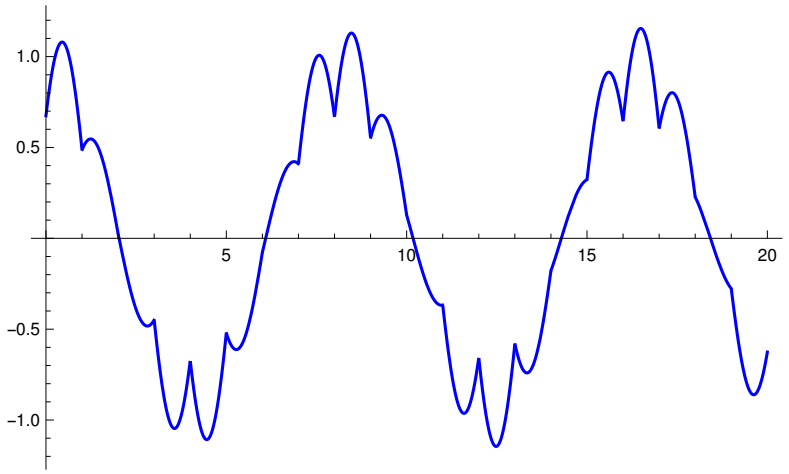

```
Show[p1, p2]
```

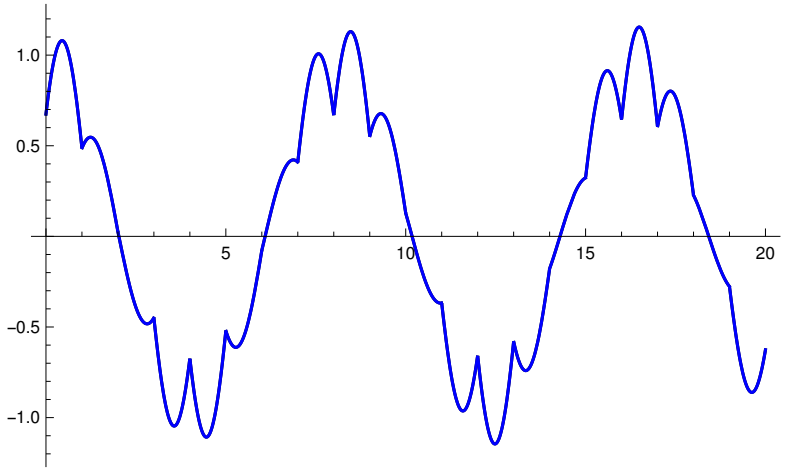


```
p3 = Plot[Im[phi1raw[x, Ceiling[x], q, eps]] / norm1[q, epsilon],
  {x, 0, 20}, PlotStyle → Black]
```

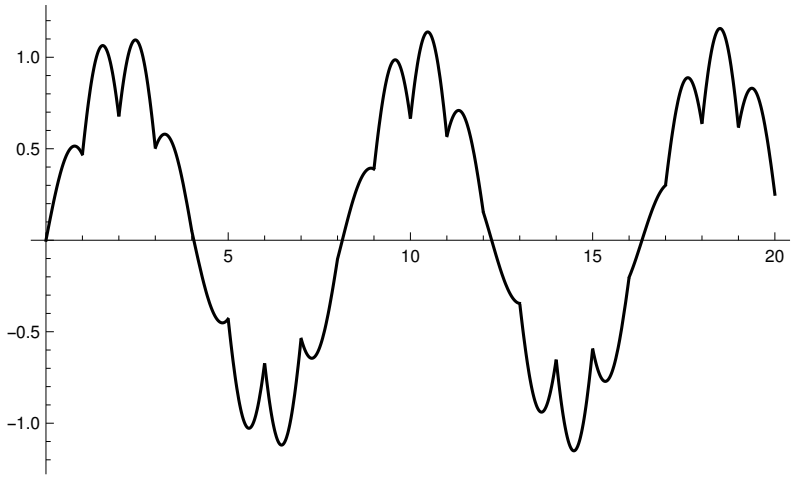

```
p4 = Plot[Im[phi2raw[x, Ceiling[x], q, eps]] / norm2[q, epsilon],
   {x, 0, 20}, PlotStyle → Blue]   (* -Im(phi1raw) *)
```

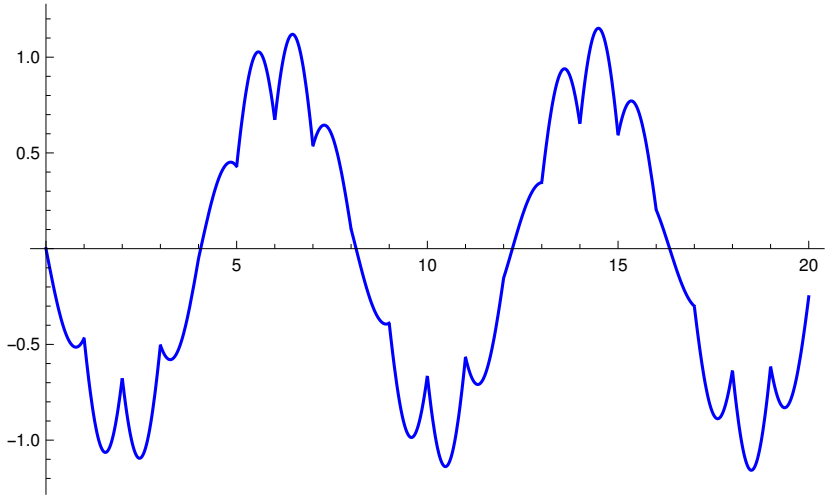


```
blochim = Show[p3, p4]
```

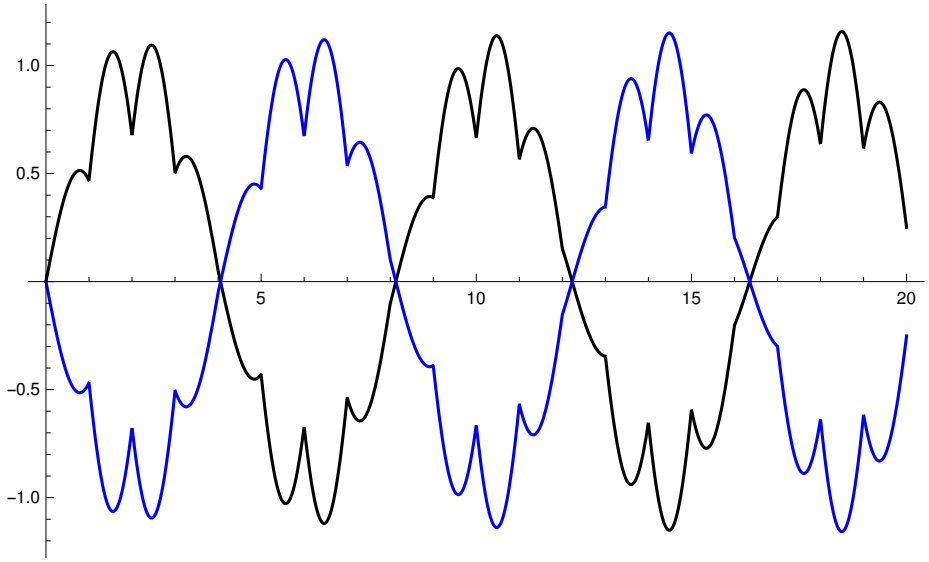


```
Export["Bloch_imaginary_eps5_omega2.png", blochim, ImageResolution → 300]
```

```
Bloch_imaginary_eps5_omega2.png
```

```
(* Show that phi1raw(x=n,n,q,epsilon) = Exp(i k n) *)

eps := 5

q := 2

phi1raw[7, 7, q, eps] // N
```

```
0.6066 - 0.795007 i
```

```
Exp[I kk[q, eps] 7] // N
```

```
0.6066 - 0.795007 i
```

```
phi1raw[8, 8, q, eps] // N
```

```
0.988362 - 0.152117 i
```

```
Exp[I kk[q, eps] 8] // N
```

```
0.988362 - 0.152117 i
```

```
(* Show that phi2raw(x=n,n,q,epsilon) = Exp(-i k n) *)
```

```
eps := 5
```

```
q := 2
```

```
phi2raw[7, 7, q, eps] // N
```

```
0.6066 + 0.795007 i
```

```
Exp[-I kk[q, eps] 7] // N
```

```
0.6066 + 0.795007 i
```

```
phi2raw[8, 8, q, eps] // N
```

```
0.988362 + 0.152117 i
```

```
Exp[-I kk[q, eps] 8] // N
```

```
0.988362 + 0.152117 i
```

```
(* Illustration: Function cos(k) *)
```

```
Clear[q, epsilon]
```

```
f[q_] := Cos[q] + epsilon / (2 q) Sin[q]     (* q = omega *)
```

```
f[q]
```

$$\text{Cos}[q] + \frac{\text{epsilon Sin}[q]}{2\,q}$$

```
epsilon := 5
```

```
plus[k_] := 1
```

```
minus[k_] := -1
```

```
pones = Plot[{plus[k], minus[k]}, {k, 0, 19},
  PlotRange → {{0, 14}, {-2, 2}}, PlotStyle → Blue, AxesStyle → Directive[20]]
```

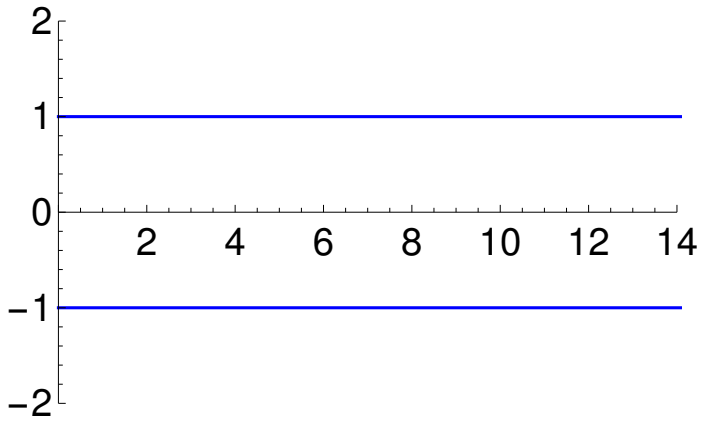


```
pf = Plot[f[k], {k, 0, 19}, PlotRange → {{0, 14}, {-2, 2}},
  PlotStyle → Black, AxesStyle → Directive[20]]
```

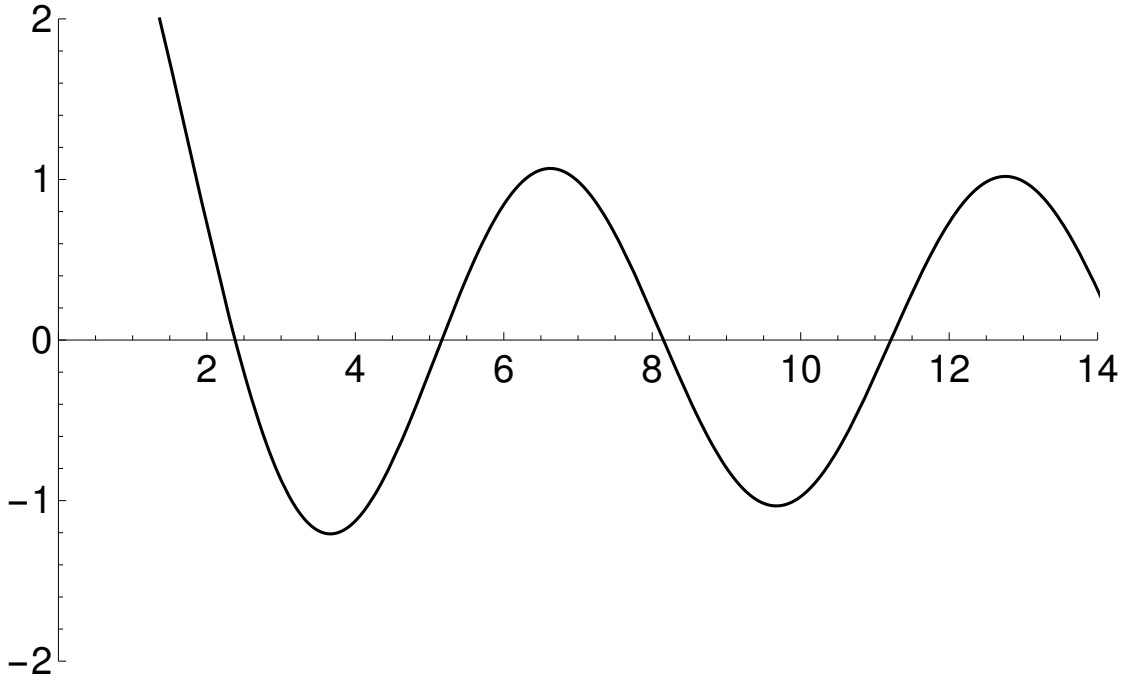

```
cosk = Show[pones, pf]
```

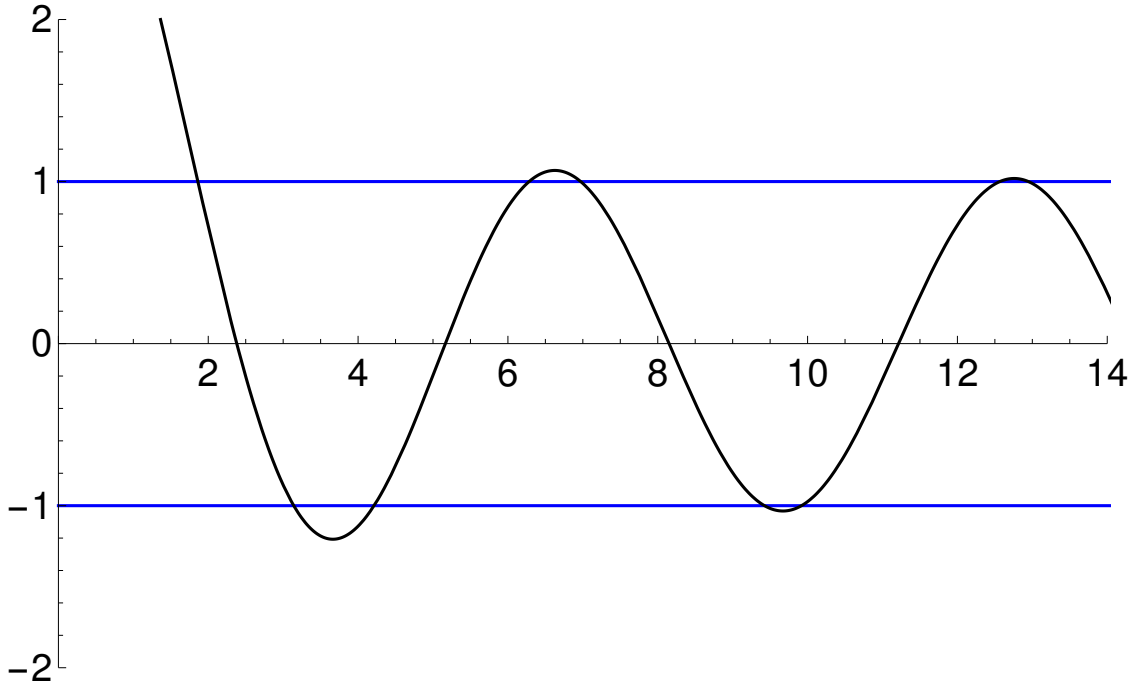


```
Export["cosk.png", cosk, ImageResolution → 300]
```

```
cosk.png
```

BIOGRAPHICAL SKETCH

Andrés Cuéllar Vega was born in Matamoros, Tamaulipas , México. Received a Bachelor of Science in Physics from UTRGV in 2019. Worked as an undergraduate research assistant as part of the Arecibo Remote Command Center, in the Center for Advanced Radio Astronomy at UTRGV, 2012-2016. Performed dozens of remote observations using the Arecibo Remote Command Center and worked in various projects. Worked as a summer research intern at the Max Planck Institute for Gravitational Physics in Hannover, Germany in 2014. Visiting student at Universidad Nacional Autonoma de México in 2017. Joined the graduate program at UTRGV in 2019 and received a Master of Science in Physics from UTRGV in 2021.

Full Curriculum Vitae, including publication list available at: https://github.com/Andrescuellarvega.

Email: andrescv.phys@gmail.com